Intensive Recrystallization-Controlled Rolling of High-Temperature-Processing Linepipe Steel with Low Niobium Content

by

Gregorio Solis Bravo

Mechanical and Electrical Engineer, Universidad Veracruzana, 2008

Master of Science in Materials Science and Engineering, University of Pittsburgh, 2010

Submitted to the Graduate Faculty of

Swanson School of Engineering in partial fulfillment

of the requirements for the degree of

Doctor of Philosophy

University of Pittsburgh

2020

UNIVERSITY OF PITTSBURGH

SWANSON SCHOOL OF ENGINEERING

This dissertation was presented

by

Gregorio Solis Bravo

It was defended on

January 10, 2020

and approved by

Ian Nettleship, Ph.D., Associate Professor, Department of Mechanical Engineering and Materials Science

Guofeng Wang, Ph.D., Associate Professor, Department of Mechanical Engineering and Materials Science

Susheng Tan, Ph.D., Associate Professor, Department of Electrical and Computer Engineering

Matthew Merwin, Ph.D., Senior Researcher, United States Steel Corporation

Dissertation Director: C. Isaac Garcia, Ph.D., Professor, Department of Mechanical Engineering and Materials Science

Intensive Recrystallization-Controlled Rolling of High-Temperature-Processing Steel with Low Niobium Content

Gregorio Solis Bravo, PhD

University of Pittsburgh, 2020

The goal of this research was to gain a systematic understanding of the major factors that control the mechanical behavior and the final microstructure of a linepipe steel after High Temperature Processing and Controlled Cooling processing. Based on this in-depth knowledge, an innovative hot deformation process for optimized microstructure, strength and impact toughness using less alloying content was developed.

The novel deformation approach Intensive Recrystallization-Controlled Rolling (IRCR) was compared to the Conventional Controlled Rolling (CCR). CCR comprised thickness reductions of 75% above the temperature of no-recrystallization (Tnr) and 67% below the Tnr, whereas IRCR utilized 85% reduction above Tnr and 46% below Tnr. These deformation approaches were applied to two alloys with contrasting Nb contents. The low finishing deformation of IRCR allowed for the reduction of deformation passes, reducing the number of deformation-stands and processing time. To achieve a fine microstructure with IRCR, recovery was limited by finishing in two passes at lower temperature and accelerated cooling was applied immediately after.

Low-Nb steel showed unexpected resistance to grain coarsening. Complex epitaxial precipitate morphology and composition accompanied retarded precipitate dissolution. Transition from recrystallization to no-recrystallization was controlled by strained induced precipitation. IRCR, preserved more deformation after finishing deformation, despite the lower thickness reduction used. The final precipitation was affected by every step of the process.

Results prompted for adjusting models of precipitation and dissolution of complex precipitates; mean-flow stress; and temperature of no-recrystallization. Optimization of grain size control from a new precipitate-dissolution perspective was enabled. The developed Low-Nb alloy kept good austenitic grain size control during austenitization to 1200°C. Combined with the novel deformation process, the studied alloy reduced microstructural and property variability, while improving productivity in thick products (19mm thick). This process reduced alloying additions and required less time for product processing. The science and engineering involved are presented and discussed in this document.

Table of Contents

List of Tables

List of Figures

Preface

Steel has been called *the backbone of our civilization*. Our most elemental infrastructure is either made of steel or made with steel tools. The human-steel technological relationship is linked to iron's abundance on earth's crust, but even more to its many functional properties. Human ingenuity produces ever-growing technological applications that demand for new, improved properties of steel. Scientists and metallurgic engineers keep working to deliver steel suitable for a wide range of technological demands.

High Strength Low Alloy (HSLA) steel is a very important family of modern steels. HSLA steel range of strength, elongation, impact energy and weldability combined with massive production and low costs have revolutionized all areas of industry. HSLA steel was born from technological changes and a new understanding of metallurgy pushed by advances like electron microscopy. The introduction of electron microscopy in the 1930's, and its development in the 1950's boosted up a defect-based race for mechanical properties, especially in metallic alloys. No longer the alloy properties would depend on their chemical composition and phases only. The development of the dislocation theory provided a better understanding of the link between defects and alloy behavior such as deformation strengthening, recovery, induced precipitation and even explain the exceptional hardness of phases like martensite. HSLA steels are a product of this physical metallurgical revolution driven by society's most demanding needs, and made possible by technologies like electron microscopy, electric arc furnaces and controlled thermo-mechanical processing.

The increasing demand for strength and toughness of HSLA steels has become a challenge for some plants. These plants have valuable remaining functional life but achieving the new product challenges and bearing the new mechanical loads requires excellent process design and ingenuous physical metallurgy. Fabrication of thick products have special difficulties through conventional HTP. Thick products imply little deformation at the final stages, this compromises the homogeneity of properties through thickness. Another drawback of conventional HTP is the loss of productivity due to dead time at the transfer bar. New thermo-mechanical approaches are required, that allow for enhanced mechanical properties and increased productivity.

Acknowledgements

First, I want to thank the advice and remarkable example of my advisor Dr. C. Isaac Garcia. I am greatly thankful for those enriching discussions and wise guidance. I feel honored to have worked with you. Similarly, my deep gratitude to my external advisor Dr. Matthew Merwin, for meticulously revising my progress, suggesting brilliant ideas and for those experiments we did side to side. I owe you respect and admiration.

I want to thank my committee members for their keen analysis of this work: Prof. Guofeng Wang, Prof. Susheng Tan and Prof. Ian Nettleship. Thank you for the enlightening suggestions and for pushing me to think beyond the scope of this work. Trying to meet your high expectations made me give my best in this work.

I wish to express my gratitude to my qualifying committee for mapping my strengths and weaknesses; and to all my professors at Pitt, for their diligent labor. My gratitude goes also to the Swanson School of Engineering staff, especially those who helped me uncountable times: Carolyn Chuha, Kelly Wodnicky, Heather Manns, Jeffrey Wade, Andrew Holmes, Charles Hager and Mike McConegly.

This work would not have been possible without the contributions of my sponsors. First, I want to acknowledge the Mexican people for providing the main funding for this project through

SEP-PRODEP and Universidad Veracruzana. My special gratitude to the Roberto Rocca Education Program (RREP) and all people behind it, your fellowship was vital support for me and my family during this project.

I want to thank to all my friends and peers for believing in me and giving me moral support. Special thanks to all members of the Ferrous Physical Metallurgy Research Group, for your unconditional support and help with experiments. For sharing the riches of your cultures, your cookies and your time with me. But especially, thank you for your kind friendship. In alphabetical order: Adam Argentine, Victor Blancas, Javier Carreno, Pedro Ciacco, Yasmin Daukoru, Christine Determan, Robert Giles, Tiffany Juan, Anastasia July, Louis Kish, Rafael Landa, Madison Milligan, Pablo Rodriguez, Luis Simoes, Yuankang Wang, Marissa Wolfe, Zhanfang Wu, Yu Zhou and all senior design students who collaborated with us.

I want to acknowledge the U.S. Steel Research Center personnel who contributed to this work: Justin Bryan, Debra Giansante, Chris Snyder, Ralph, Joe Bosko, Dan Lisjack, Rick Martin and Bill Gaber. Thank you for your contributions during experiments.

I want to thank those who I love the most. To my wife Mariana, whose support was indispensable for the completion of this work. For those long days when you had to be mother and father, I admire your strength and thank your invaluable efforts, this is the fruit of your work. To my parents and siblings, whose love nurtured my strength and confidence, to you I owe my resilient spirit. Thank you for believing in me. Finally, I want to give special thanks to the sweetest love of my life, my two daughters. Dafne and Lis, you are the light of my life, words are not enough to describe all that you mean to me. Through your love I gained the stamina to complete this project. It is all because of you, I dedicate this and all my life endeavors to you.

1.0 Introduction

The goal of this research was to gain a fundamental understanding of the major factors that control the mechanical behavior and the final microstructure of a linepipe steel after High Temperature Processing and Controlled Cooling. Based on this in-depth knowledge, an innovative hot deformation process for optimized microstructure, strength and impact toughness using less alloying content was developed.

The approach includes thorough studies of austenite grain coarsening, dissolution of precipitates during reheating, recrystallization, precipitation, deformation and transformation that occur during HTP. Experiments included reheating, hot compression and hot torsion with different deformation schedules and controlled cooling. The studies compared three alloys with different Nb content. Nb contents around 0.1wt% have traditionally been considered crucial for the HTP process. The present work hypothesizes that similar mechanical properties and microstructural control can be achieved with half as much Nb, without the need to adjust other alloying elements. The hypothesis includes the test of an innovative deformation approach for producing a high strength-high toughness microstructure from a low Nb linepipe steel.

Objectives:

1. Optimize precipitate formation and microstructure for strength and toughness higher than similar commercial alloys with special focus on thick products (19mm).

2. Develop a new, effective and robust high temperature process for thick linepipe steel through Intensive Recrystallization-controlled Rolling.

3. Reduce alloy content costs while effectively achieving microstructural optimization.

2.0 Background

HSLA steel is result of a multidisciplinary technological advancement. Steel has evolved dramatically and developed into many families. One of the most important modern families of steel is the HSLA steel. The work that was undertaken in this study required an in-depth understanding of alloy design-processing-mechanical properties relationship. The fundamental understanding of grain size control, thermomechanical processing, precipitation reactions, transformation products, strengthening mechanisms, and the structural factors that control toughness was not only important, it was indispensable to achieve the goals of this thesis.

2.1 Strengthening Mechanisms

The dislocation theory was proposed in the early 1930's independently[1] by E. Orowan[2], G.I. Taylor[3] and M. Polanyi[4]. The idea was born as a proposed explanation to the differences between measured and calculated (shear-caused slip deformation) strengths. At the beginning the idea was controversial, but after transmission electron microscopy (TEM) observations of dislocations, the theory became irrefutably accepted. Different strengthening mechanisms were later explained making use of dislocation theory.

Following dislocation theory, all strengthening mechanisms in metals can be explained due to their ability to stop or prevent dislocation motion. Dislocation motion through climb or glide, is well recognized as the phenomena that allows plastic deformation. Hence, any means that difficult or inhibit dislocation motion retard the onset of plastic deformation or yielding, in other words, strengthen the alloy.

The first natural force that prevents dislocation motion was first described by Peierls, and its equation was corrected by Nabarro[5, 6]. The Peierls-Nabarro stress, σ_{PN}, is the necessary stress to move a dislocation[7].

$$\sigma_{PN} = \frac{2\mu}{1-\nu} exp\left(1 - \frac{4\pi h}{2b(1-\nu)}\right) \tag{2-1}$$

Where μ is the material's shear modulus, ν is Poisson's ratio, b is the unit slip distance, and h is the distance between glide planes. Once this stress has been surpassed, a dislocation can start motion. Any obstacles on the dislocation path strengthen the alloy. Such obstacles may be lattice distortions due to alloying elements in solid solution, type of grain boundaries, the type and size of precipitates and even other dislocations. The different types of obstacles provide the understanding of the different strengthening mechanisms, as were discussed in the next sections.

2.1.1 Solid Solution Strengthening

The presence of solutes in iron lattice produce distortions that can hinder dislocation motion. Solute atoms are never the same size as the matrix atoms, this size difference is directly proportional to the resulting distortion in the lattice due to their presence. The difference in size is also responsible for the solute atoms' locations in the solid solution lattice. A classic rule of thumb is that solute atoms which diameter is less than 0.85 times the diameter of the base element atom will take interstitial locations. Whereas solute atoms which diameter is at least 0.85 times the diameter of the base element atom will locate as substitutional. Either interstitial or substitutional, solute atoms produce local distortions.

Interstitial atoms are usually bigger than the interstitial space that they occupy, this translates on local compression of the lattice to make room for the interstitial atom. The local compression around an “oversized” interstitial atom comes associated to a stress as it would be expected from Hooke’s law. On the other hand, substitutional atoms are either smaller or bigger than the base element atomic size. To yield the extra space necessary for an oversized atom, or to make use of the extra space yield by a smaller substitutional atom, compression or tension fields are generated around them. In summary, every solute element present in solid solution produces stress fields near their location in the lattice.

It is well-known that dislocations find it difficult to migrate through a distorted lattice. Stress fields hurdle the path of a dislocation by interacting with the dislocations own stress field. Edge dislocation’s stress fields are both compressive and tensile, one on each side of the slip plane. Edge dislocations also have a very localized shear component at the slip plane. Similarly, screw dislocations have associated shear stresses due to their helicoidal nature. In steels, the distortions caused by substitutional atoms, produce hydrostatic distortions that interact with edge and mixed dislocations only. On the other hand, interstitial elements like C and N have shear and hydrostatic components, allowing them to interact with both screw and edge dislocations[8].

Interstitial elements interaction with dislocations is strong enough to make these atoms migrate towards dislocations creating atmospheres that may lock dislocations in place. The phenomenon was elegantly described by Cottrell and Bilby[9]. An equation was proposed by Cottrell and Bilby for the force necessary to unlock a dislocation from this type of atmosphere, σ_0.

$$\sigma_0 = \frac{3\sqrt{3}A}{4\lambda^2\rho^2} \tag{2-2}$$

Where A is a constant dependent on each base alloy, λ is the interplanar spacing and ρ is the distance from the dislocation line to the interstitial atoms line. When this force is surpassed, dislocations free from their atmospheres, dropping the yield stress value instantly. This explains the yield point phenomenon.

2.1.2 Precipitation or Secondary Phase Strengthening

Another way to hinder dislocation motion and strengthen an alloy is by interactions with secondary phase particles. Secondary phase particles, e.g. precipitates, represent low energy positions for a dislocation. Hence, when a moving dislocation finds disperse precipitates, voids, or inclusions, the strong interaction difficult their motion. To keep moving, a dislocation that has found dispersed particles must either cut through them or loop around them[1, 10]. When these particles are harder than the matrix, cutting through them is not possible, hence, looping around them or cross-slip are the only alternatives[1]. The looping phenomenon was well modelled by Orowan[10]. The dislocation line bends, as parts of it keep moving, while other parts are pinned by the particles. Once the particles are surpassed, the dislocation line re-builds and straightens. This phenomenon causes a yield stress increase. An equation for this yield stress increment due to particles was proposed by Orowan[10]:

$$\Delta\boldsymbol{\tau}_{\boldsymbol{y}} = \frac{\boldsymbol{Gb}}{\boldsymbol{L}} \tag{2-3}$$

Where $\boldsymbol{\Delta\tau_y}$ is the yield strength increase due to particles, G, is the shear modulus of the base metal, **b** is the Burgers vector associated to the dislocation and **L** the interparticle spacing. From Equation 2-3, it can be seen how important the interparticle spacing is for the strengthening through this mechanism. Later, Ashby would incorporate the effects of statistically distributed interparticle spacing and particle size, when written in terms of tensile stress gives the following equation[8, 10]:

$$\Delta\boldsymbol{\sigma}_{\boldsymbol{y}} = \left(\frac{\mathbf{0.538}\boldsymbol{Gbf}^{\mathbf{1/2}}}{\boldsymbol{X}}\right) \boldsymbol{ln}\left(\frac{\boldsymbol{X}}{\mathbf{2}\boldsymbol{b}}\right) \tag{2-4}$$

Where, $\Delta\sigma_y$, represents the increase in yield strength, f, the volume fraction of precipitates and, X, the average diameter of the particles. In summary, the strengthening is proportional to the square root of the volume fraction of precipitates and increases at smaller interparticle spacing.

Precipitates coherency to the matrix and shape are important factors affecting pinning. Cubic precipitates have been observed to be more effective at pinning grain boundaries, when compared to round ones[11]. Coherency of a precipitate affects both the exerted force on a boundary and the growth rate of the precipitate itself[12]. Coherent particles are more effective than incoherent particles at pinning grain boundaries[13].

2.1.3 Grain Boundary Strengthening

An inexpensive strengthening mechanism that does not require alloying, relies on the interaction of dislocations with grain boundaries. Grain boundaries (GB) are disarrayed regions that act as potential barriers almost impossible to pass for a moving dislocation. When dislocations reach a GB they pile up until the stress concentration reaches the yield level[14] when dislocations can move from one grain to the other[15]. Dislocations can also use grain boundaries as nucleation sites. Hence for grain boundary strengthening a high density of grain boundaries is better, which translates onto small grain size. The GB's effect of increasing yield stress must be then attributed to small grain size. This strengthening mechanism was well described in the equation by Hall[14] and Petch[16] which stands not only for steel, but for many non-ferrous alloys:

$$\boldsymbol{\sigma_y = \sigma_0 + k_y d^{-1/2}} \tag{2-5}$$

Where σ_y stands for yield strength, σ_0, is a constant of the base material, called friction stress, equivalent to the yield stress of a single crystal of the matrix metal; k_y, stands for the slope of the GB-strengthening effect and, d, is the average grain size. The well-accepted Hall-Petch equation clearly shows how finer grains increase strength.

A further look at the Hall-Petch equation help distinguish the temperature dependence of this phenomenon. σ_0, the theoretical strength of the alloy reduces as temperature increases. On the other hand, the slope k_y, despite not being constant, has been proven insensitive to temperature[17]. In general, the yield stress may be regarded as temperature sensitive, however the tendency to increase yield stress by finer structure remains true at all solid temperatures. The same strengthening mechanism may be associated with other interfaces like, sub-boundaries, laths or interlamellar interfaces. In other words, besides having small grains for strength, it also helps having a fine pearlitic interlamellar space, fine bainite laths and plenty of sub-boundaries.

The tendency to strengthening as the grain size decreases have its limits. It has been observed that at nanometric grain sizes (i.e. <10nm) smaller grains reduce strength. This is called reversed Hall-Petch effect and has been attributed to deformation through sliding and grain boundary rotation[18]. However, reaching this level of grain refinement is not a concern in the production of HSLA steels where the smaller grains are still in the order of microns, so the researcher can trust that grain refinement will always improve the mechanical properties.

The type of grain boundaries is also a very important factor to consider in grain boundary strengthening since not all boundaries interact the same with dislocations. It has been proposed that the dislocation-GB interactions depend on misorientation, free volume and energy of the boundaries[19, 20]. It is generally accepted that the energy of a GB increases with misorientation up to about 15°, after which the energy is virtually constant. Hence, a classic distinction of type of boundaries is based on this. Low-Angle Grain Boundaries (LAGB), typically below 15° of misorientation, and High-Angle Grain Boundaries (HAGB) with misorientation greater than 15°. Research have suggested a critical misorientation angle below which the LAGB resistance increases with misorientation, and above which the resistance of a LAGB equals that of a HAGB [15, 21]. Another interesting type of GB is Coincident Site Lattice (CSL) boundaries. CSL boundaries have in a degree a periodic order that derives in a dramatically lower interfacial energy. This order can in very special cases facilitate dislocation slip through the boundary[22].

2.1.4 Dislocation Strengthening

Strain hardening is a common approach to describe this hardening, however dislocation strengthening can also be due to any other transformation that introduces dislocations, such as martensitic transformation. Dislocation motion is necessary for plastic deformation to occur but having more dislocations do not facilitate yielding. At first sight, one could expect that massive dislocation motion would allow for easier plastic deformation. In reality, dislocations interact with each other dificulting slip and even stopping each other, these interactions are the cause for dislocation strengthening. Dislocations that encounter each other may combine, annihilate or entangle. Opposite dislocations attract each other while alike dislocations reject, due to their stress fields[3]. These attraction forces may bring two dislocations together. If two opposite dislocations travel in different slip planes, they will come as close as possible. Annihilation occurs when two opposite dislocations meet while traveling on the same slip plane. If two dislocations that are not opposite to each other meet, they will either combine into a mixed dislocation or entangle. If the dislocation density is high, entanglement is highly frequent and strengthening occurs. The well-known strain hardening phenomenon may be regarded as a way of dislocation strengthening. During deformation the dislocation density increases, this reduces the spacing between dislocations so the resistance to shear in the material increases[3].

Dislocation strengthening occurs whenever dislocation density is increased. Dislocation density can be heavily increased during cooling transformations. Transformations occurring at lower temperatures are generally associated with higher dislocation content. Using this type of transformations may enhance strength.

2.2 Toughness Control

The concept of toughness was developed after the second world war while studying brittle fracture at welded joints in the called “liberty ships”[23]. An understanding of fracture mechanics was developed based on mathematical modeling of crack nucleation and growth. Early research works highlighted the importance of factors like cleanliness, homogeneity, load conditions and temperature [5, 24-28]. Later works would relate factors like grain size, precipitation, phase balance, microstructure morphology, grain boundaries and even texture to a common property, toughness.

The ability of a material to absorb energy before fracture is toughness. The energy is usually absorbed by means of plastic deformation and the release of heat. Consequently, a material capable of plastic deformation will show a better toughness than a more rigid material. The former example of material is called ductile, while the latter is called brittle. One can also call *ductile fracture* to that fracture where plastic deformation has taken place, and *brittle fracture* to fractures with little or no plastic deformation. In other words, a ductile material has good toughness, while a brittle material has poor toughness. However, fracture may occur under a variety of circumstances, which makes toughness a property that may be expressed and measured in different ways.

Fracture toughness is a measurement of the energy required to produce a unit area of fracture under concentrated stress due to the presence of a crack at a steady or very slowly applied load. This can be plastic-elastic fracture toughness, conventionally denoted by J_{1C}, or plane strain fracture toughness K_{1C}. Fracture toughness is the critical stress intensity factor of a material. That is, the minimum stress intensity factor necessary to undergo fast fracture propagation. Fracture toughness definition implies the occurrence of fracture at very special conditions, that is, under a slowly growing load in the presence of a pre-existing crack. But this is not the only way materials fracture.

Toughness can be quantified through different mechanical tests and loading paths that lead to fracture under very different mechanical conditions. Toughness simplest observation comes from the tensile test. In a tensile test, the area underneath the stress-strain curve is a proportional quantification of the energy required for fracture. High toughness, for instance, would produce a large area under the stress-strain curve. This is a good observation of toughness under slow strain rate. However, fracture can occur under circumstances way different than a slow steady unidirectional overload. Impact, fatigue and thermal shock are other causes of fracture, impact being one of the most susceptible to cause unexpected fast fracture failures.

Impact toughness can be measured through a few different tests. Good examples are the Charpy V notch impact test, the Izod impact test and the Dropped-Weight Tear Test (DWTT). What these tests have in common is the proper conditions to take to the limit a materials ability to withstand impact.

It is well known that materials ductility is favored by slow deformation and high temperature. Slow loading rate gives time for the plastic deformation mechanisms to occur. High temperatures can activate slip systems that may facilitate plasticity. Furthermore, structural cleanliness and smooth homogeneous surface favor toughness. Microstructural and geometrical homogeneity provides a smooth distribution of stress, while also limits the potential crack nucleation sites. All these factors facilitate ductility, that is why, when testing impact toughness, they must be minimized so the property can be measured at the most critical conditions. This way, impact toughness is measured while concentrating stress at a notch root, under very fast load rates and usually at very cold temperatures.

Charpy V-notch (CVN) test is a standardized impact toughness test, performed at decreasing temperatures. Specimens (55mmX10mmX10mm) are sampled from many directions of the product, especially transverse to rolling direction. A “V” shaped notch is machined in the thickness direction for stress concentration. The specimen is hit by a pendulum right behind the notch and the energy absorbed is registered. From the fractured specimen, the percent of ductile fracture area is measured. Plotting absorbed energy against test temperature provides information about ductile to brittle transition temperature when present.

Another very common impact toughness test in HSLA steels is the Dropped-weight Tear Test (DWTT). A notch is fabricated at one edge of the specimen through thickness. Impact is done in a three-point bending fashion at decreasing temperatures. The most important measurement from this test is the percentage of shear fracture area at the different temperatures, which results in a ductile to brittle transition plot. A particularity of this test is that specimens have the entire thickness of the product. This ensures that the homogeneity of the product is tested, and the results are easily relatable to working conditions

2.2.1 Fracture Mechanics Overview

Fracture can occur in three conventional well-known modes: Mode I is crack opening. This fracture mode occurs when the applied stress is perpendicular to the crack direction. The applied stress obliges the crack to open in the stress filed direction, and to grow in the perpendicular direction to the stress. Mode II of fracture is slip. Slip fracture occurs when the applied stress is shearing in the same plane of the crack. This forces the crack to grow parallel to the stress field. Mode III of fracture is tearing. Tearing occurs as result of a shear stress applied in a direction normal to the plate where it is applied and at the same plane of a crack. Combined modes of fracture are common, due to the imperfect orientation of cracks and stresses.

Crack orientation with respect to stress field matters. It is important to notice that when a normal stress is applied, the most critical orientation for a crack is perpendicular to the stress. That is, in opening mode. If a normal stress is applied to a crack oriented parallel to the stress field, the crack is virtually insensitive to this stress. Conversely, when a shear stress is applied perpendicular to a pre-existing crack, this crack is virtually insensitive to this stress. These are very important observations, for they mean that one should be able to stop a crack if one can manage to divert their growth direction.

2.2.2 The Effective Grain Size and its Effect on Toughness

Small grain size favors toughness, this was shown by Cottrell and Petch in their well-known equation[29] and is widely accepted in the literature[30-34], however conventional grain size should not be directly linked to toughness that way. Not all types of boundaries are good at stopping cracks. Hence, it may be misleading to directly relate grain size to toughness, one must use the concept of effective grain size.

The effective grain size is a commonly used parameter that distinguishes a structure refinement, regarding its HAGB. The measured effective grain size can be directly related to toughness because it limits the straight propagation of cracks. As explained in previous section, there are critical plane orientations of the cracks that favor their propagation according to their load mode. Limiting the growth of the cracks within this critical plane is crucial for toughness control. This straight trajectory, also called Unit Crack Path (UCP) depends, naturally, on how close the crack-stopping features are in the microstructure. The UCP is equivalent to the Cleavage Facet Size (CFS) when transgranular cleavage fracture occurs[32]. The effective grain size can be determined from the interspacing of features that limit the size of the UCP or the CFS[32].

Grain boundaries are excellent crack stoppers, so having abundance of them is the right strategy when toughness is a concern. Having more boundaries in a given volume can only mean one thing, small grain size. Grain boundaries deviate a crack's direction of growth, very likely turning them onto a direction where stress is not critical for any fracture mode to occur. This means, by deviating crack growth, grain boundaries act as crack stoppers. However, not all boundaries are equally good at arresting crack propagation. According to Pickering[35], High-angle Grain Boundaries (HAGB) are the best crack stoppers among grain boundaries. Conversely, some boundaries are highways for cracks, especially some that have big incoherent particles, or segregation happening at them. Coherence, misorientation and energy of the boundaries also determines how they react to cracking.

The importance of a small effective grain size lies in that it limits the stress concentration at the tip of a crack. Concentration of stress at the tip of a crack is considered proportional to the length of that crack[7]. A small effective grain size combines two phenomenon that provide toughness: the limitation of stress concentration at the crack tips (i.e. due to shortening of the crack length), and the change of direction of crack propagation.

2.2.3 Acicular Ferrite, a Tough Microstructural Component

Acicular ferrite (AF) is a desirable microstructural component when toughness is a main concern. Its characteristic fine structure and randomly-oriented crystallites deflect cracks and difficult crack propagation[36-38]. AF toughness advantages are numerous, justifying it as our microstructure of choice in the present project.

Research has compared the same alloy with different microstructures, ferrite-pearlite (F-P), ferrite-bainite (F-B), and AF. It has been shown that AF is superior in strength and toughness[39]. In Figure 2.1 CVN results are plotted for steel 1 (F-P), steel 2 (F-B) and Steel 3 (AF) showing a higher absorbed energy for the AF microstructure. As can be appreciated in Figure 2.2, where the three microstructures are next to their correspondent fractography, there is a finer CFS for the AF microstructure. The finer CFS of AF denotes the higher toughness of the microstructure.

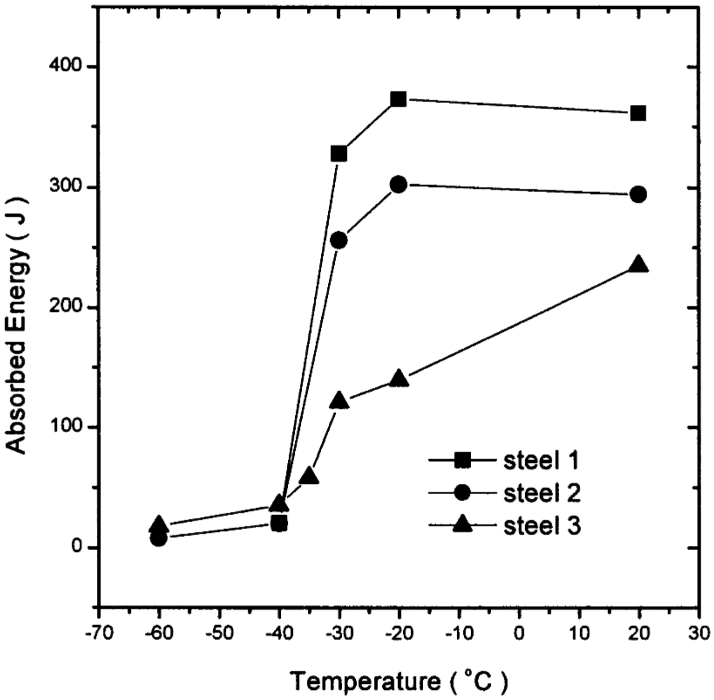

Figure 2.1 Comparison of CVN impact test of the three microstructures of the alloy by Byun et al[39].

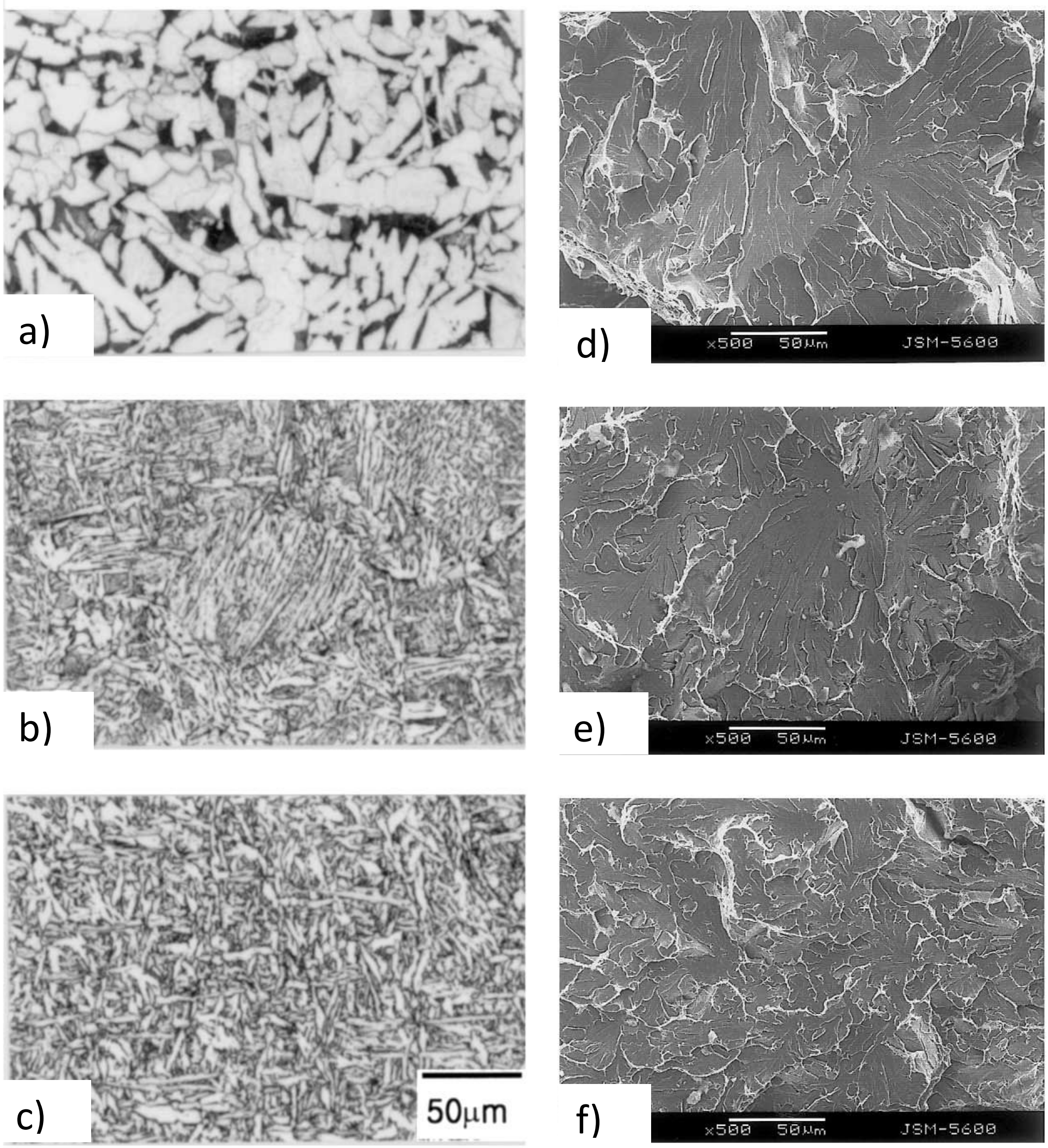

Figure 2.2 Same alloy showing different microstructures and their correspondent fractographies. a) F-P, b) F-B, c) AF. Cleavage facet size is evident for d) F-P, e) F-B and e) AF [39].

AF is characterized for having a small effective grain size and high strength[40-42]. The small effective grain size may come from the set of ferrite plates with misorientations below 15 degrees[43]. This refinement may be obtained by applying accelerated cooling on a deformed or particle-containing austenite with numerous nucleation sites. AF characteristically has numerous HAGB due to its randomly oriented crystallography. This characteristic is crucial for crack arrest, as it was explained in section 2.1.3. The size of AF has a high dislocation density, as compared to polygonal ferrite (PF) [44], this high dislocation density is responsible for the characteristic strength of this phase. Due to all the mentioned characteristics, acicular ferrite is the microstructural component to aim for when producing a HSLA steel with high strength and high toughness.

2.2.4 Other Microstructural Factors Affecting Toughness

Secondary phases with mechanical properties considerable different than the matrix can significantly affect toughness. If the particle/matrix interface is incoherent, it is easy for these particles to be crack initiators. Size of the second phase is a critical parameter for determining their effect on toughness. Hence, big incoherent carbides or inclusions are regarded as crack initiators.

Carbon-rich constituents, such as martensite-austenite (MA), are well known to be detrimental for toughness when their volume fraction and size are big. Research has shown that MA acts as crack nucleator at the MA/matrix interface. An aspect that makes MA particularly dangerous is that it forms at grain boundaries. During deformation, dislocation pile-ups occur at grain boundaries, concentrating stress at MA islands[45]. This makes slender MA islands are more effective crack nucleators than equiaxed MA[32]. Volume fraction of MA remains the most important parameter, especially affecting Ductile-to-Brittle Transition Temperature (DBTT) of impact tests [32].

Texture positive and negative effects on toughness have been reported. Texture can be responsible, for instance, of aligning cleavage planes with a crack plane, or promote preferential slip planes for deformation[46]. A study of X80 LP steel claims that the $\{112\}\langle 110\rangle$ component is responsible for ductile fracture anisotropy. Whereas $\{001\}\langle 110\rangle$ and $\{110\}\langle 001\rangle$ orientations are accounted for low temperature cleavage[47, 48]. In another study of a high strength steel, component $\{311\}\langle 011\rangle$ is accounted for poor impact toughness at 45° and component $\{332\}\langle 113\rangle$ is correlated to strength and toughness improvements[49].

2.3 High Strength-Low Alloy (HSLA) Steels

HSLA steels are a type of microalloyed steels produced by controlled rolling and designed for low cost, better mechanical properties and corrosion resistance than plain carbon steels[50]. Their design was a result of pursuing higher strength, toughness and ductility, while keeping good weldability. The C content in HSLA steel usually does not exceed 0.26wt%. Mn is always lower than 2wt% and S below 0.04wt%.

HSLA steels make use of all strengthening mechanisms to achieve strength. Solid solution strengthening by C, N, Mn, Si and other elements. Grain boundary strengthening by refining the microstructure homogeneously through the thickness. Dislocation strengthening through rapid cooling transformations after rolling. And precipitation hardening through carbides and nitrides such as VC, VCN, NbC, Nb(C,N), (Ti,Nb)(C,N), etc.

Because strength is the main concern, standardization organizations such as SAE (Society for Automotive Engineers) and API (American Petroleum Institute) have their own specifications and designations for HSLA steels. API classifies them by their strength in KSI (X-42, X-80, X-120, etc.). SAE uses a 9 followed by two digits indicating the minimum strength in KSI (942X, 945A, 950D), the letter following the number indicates the type of alloying elements used. For example X is used to indicate content of N, Nb, V and other[51]. The mechanical properties are achieved by carefully choosing the microalloying content, optimizing the thermo-mechanical process (TMP) and the final cooling, as well as the coiling temperature. HSLA steels are very good at structural applications, but especially good at the oil and gas industry. API standards has a whole range of specifications for linepipe products, giving to some HSLA steel the name of Linepipe Steel.

2.3.1 Line Pipe Steel

Line pipe steel (LP steel) is a type of HSLA steel specifically designed for strength, toughness and corrosion resistance required in the oil and gas industry. LP steel must have good weldability for pipelines are built by this joining method. The importance of LP steels in modern society comes from the fact that pipelines are the most efficient mode for fluid transportation over long distances. The development of steel processing technologies and the high requirements from oil industry promoted advancements in LP steel in the last decades.

In 1948 API published specifications for X42 line pipe steel, many things have changed in line pipe steel since then. The pipelines became bigger, the pressures higher along with the requirements for higher strength and lower cost. In the race for toughness sulfur content was reduced from 0.012wt% to 0.002wt%[52]. Strength requirements nearly tripled in the last twenty years from 42 to 120 KSI. Controlled rolling processes and the development of Accelerated Controlled Cooling (ACC) systems introduced the possibility of new microstructural combinations.

One LP steel production method common today is the patented Compact Strip Mill (CSP) introduced in 1989 by SMS. The novelty of this process was the continuous uninterrupted process from casting to coiling. The casting process is done in slabs from 50 to 90mm thick. Instead of cutting the slab after solidification, it is fed directly into a furnace for temperature homogenization. This is followed by rolling to final thickness and controlled cooling.

Another (most common) production process is the Conventional Controlled Rolling (CCR). Here, reheating is followed by two stages of deformation: "Roughing" rolling at high austenitic temperatures, in recrystallization conditions, and "Finishing" rolling, at low austenitic temperatures in non-recrystallization conditions. The roughing refines the austenite grain size by multi-pass deformation and recrystallization cycles to ~20 μm[53]. The finishing accumulates strain in austenite, "pancaking" the grains, and conditions the austenite with numerous nucleation sites. As steel grades kept increasing, loads at the mills kept growing and new deformation techniques had to be engineered.

A remarkable advancement was the development of High-Temperature Processing (HTP). HTP utilizes Nb to increase the non-recrystallization temperature, allowing for deformations at higher temperatures. This process improved dimensional tolerances, weldability and improved toughness through microstructural control. The classic ferrite-pearlite microstructure was replaced by acicular ferrite and bainite[54]. HTP production of line pipe steel is object of analysis of this research work. Opportunities for improvement in the HTP are assessed, based on scientific observations.

3.0 Linepipe Steel and the High Temperature Process

Thermomechanical processing (TMP) means to utilize the process of shaping the steel with a double purpose: to achieve both the geometric and the mechanical expectations without further heat treatment. The High Temperature Process (HTP) is an industrial TMP created for reducing mill loads and increase productivity by utilizing unusually high temperatures of deformation. High Nb contents of about 0.12wt% are considered crucial to HTP, given niobium's ability to promote non-recrystallization conditions at elevated temperatures. The process comprises four important operations: reheating of slabs; roughing deformation in recrystallization conditions; finishing deformation in non-recrystallization conditions; and controlled cooling transformation.

3.1 Reheating

The reheating operation is a necessary step for homogenizing the chemistry of the alloy, as well as to facilitate deformation. During reheating, dissolution of micro-alloying elements like V, Mo and Nb must be completed and austenite grain coarsening or abnormal growth avoided. During this step, thermal homogeneity and target discharge temperature must be met. The homogeneous grain size, chemistry and temperature are key factors that minimize variability in final properties.

3.1.1 Prior Austenite Grain Size (PAGS) Control During Reheating

Austenite grain growth can be arrested by precipitates which exert pinning forces on GB's. 1948 Zener's well-known model for limit grain size was idealized on spherical grains and spherical particles. Numerous modifications to Zener's model have been made[11, 55-59] that claim better fitting to experimental data on specific conditions. The common ground is that higher volume fraction of precipitates in finer sizes limit grain size.

3.1.2 Grain Growth and Grain Boundary Motion

Grain boundaries' intrinsic energy minimization is the driving force for grain growth. As grains increase in size, the overall GB interface area is reduced. The grain growth force, responsible for GB migration have been long studied, this force must outstand pinning and drag forces for a GB to move.

The grain coarsening force can be understood trough force-equilibrium. For simplicity, consider a bidimensional GB structure. Consider the most common case, where three boundaries meet at a point, four or more boundaries at a point is highly unlikely, but can also happen. If three boundaries meet at a point, each of them exerts a force on this node. If the three boundaries have the same surface energy, all three forces on the node are equal. This means that equilibrium at this node requires that these boundaries arrange in a 120° angled fashion, and if they are not like this, they will tend to move towards equilibrium. This has geometric implications that dictate the growth of the bigger grains at the expense of the smaller.

Big grains grow due to GB migration towards their center of curvature. The rate of atom jumps across a GB is higher from the convex side to the concave one, as compared to the opposite.

This is usually associated to a higher stability on the concave side of the boundary, due to more neighbor atoms. When a grain is bigger than its neighbors, its boundaries bend to comply the 120° requirement at triple points. This GB curvature makes big grains' boundaries concave and causes grain growth. This explanation is rather oversimplified, since the structure is three-dimensional and more complex. However, the analogy is very good. Abnormal grain growth of austenite during reheating is undesirable because it lowers the mechanical performance and homogeneity. To avoid grain coarsening, pinning and dragging forces on GB are necessary.

3.1.3 Arresting Grain Coarsening

The most common strategy to avoid grain coarsening of austenite is to produce fine precipitates that can pin the boundaries in place, limiting growth. Pinning forces that counteract grain growth force can result from several factors. Essentially, any interface in the path of a GB will interact exerting forces on it. Examples include pores, precipitates, non-metallic inclusions and even external surfaces. In HSLA steels, pores and non-metallic inclusions are undesirable and avoided, hence, precipitation is the tool for grain size control.

According to Zener, the grain size of an alloy can be limited by the presence of fine precipitates. Assuming spherical particles, Zener calculated that the maximum pinning force exerted by a volume fraction of precipitates, f, of radius, r, on a GB with surface energy, γ, is $3\gamma f/(2r)$ and the growth force is $2\gamma/r$. Hence, the grain growth arrest would occur when the two forces are equal, giving the limit grain size[57]:

$$D_{max} = \frac{8r}{3f} \tag{3-1}$$

However, Zener’s assumptions idealize the structure of an alloy. To accommodate for more real conditions several modifications have been proposed[11, 55-59].

Most models follow a similar logic. The limit in grain size is a consequence of the following three observations: First, every curved GB has a migrating force towards its center of curvature. Second, every particle exerts a drag force on the GB that is in contact with. Third, as grain growth force gets weaker due to growth, multiple particles are collected at GB’s and their drag forces add-up. At the point where pinning force equals grain growth force grain coarsening stops.

The models to predict grain size limit follow that logic, balancing out models of driving force (See Table 3.1) and models of pinning force (See Table 3.2). Some grain size prediction models available in the literature are shown in Table 3.3.

Table 3.1 Models of grain growth driving force.

Model Name	**Expression**	**Where:**
Zener[8, 57, 60]	$F_Z = \frac{2 * \gamma}{R}$	γ=Interfacial energy, R=Radius of curvature
Gladman[57, 61]	$F_G = \left(\frac{2}{Z} - \frac{3}{2}\right)\frac{\gamma}{R_0}$	R=Radius of grain, R_0=Radius of the average grain, γ=Interfacial energy Z=R/R_0
Hillert[8, 57]	$F_H = k\left(\frac{1}{R} - \frac{1}{R_C}\right)$	R=Radius of curvature, R_C=Critical grain radius, k= constant

Table 3.2 Models of pinning force.

Model Name	$Expression$	Where:
Gladman[8]	$F_{Pin} = \frac{3f\gamma}{2r}$	f= Volume fraction of particles. γ=Boundary Surface energy per unit area r = particle radius
Rigid Boundary[62]	$F_{Pin} = \frac{6f\gamma}{\pi r}$	
Flexible Boundary[62, 63]	$F_{Pin} = \frac{3\gamma f^{2/3}}{\pi r}$	

Table 3.3 Grain size prediction models.

Model	**Expression**	**Where:**
Zener[60]	$R = \frac{4r}{3f}$	R= radius of curvature of GB, r= radius of mean particle, f=volume fraction of precipitates
Hillert[64]	$D_{cr} = \frac{8r}{3f^{0.93}}$	D_{cr}=equilibrium grain size, r=particle mean radius, f=particle volume fraction
Nishizawa *et al.*[56]	$D_{cr} = \frac{8r}{3f^{2/3}}$	D_{cr}=equilibrium grain size, r=particle mean radius, f=particle volumen fraction
Rios[59]	$D_{cr} = \frac{r}{3f}$	D_{cr}=equilibrium grain size, r=particle mean radius, f=particle volumen fraction
Moon *et al.*[65]	$\frac{dD}{dt} = nK\left[\frac{1}{D} - \frac{f}{Zr}\right]^{(1/n)-1}$	D=mean grain diameter, n= time exponent, K=rate constant, Z=Zener coefficient, r=particle mean radius, f=particle volume fraction

Solute drag force, another type of force acting against grain growth is exerted by solute atoms on GBs. The solutes are naturally attracted to the lattice distortions at GBs, minimization of elastic energy due to misfit is the driving force. It is well known that an alloy atom present in austenite causes local elastic strain of the matrix. As GBs are regions of lattice misfit, the strain energy associated to a foreign atom and that of the GB can be reduced if the atom migrates to the neighborhood of a GB. This is the thermodynamic drive for the segregation phenomenon[60]. As segregation lowers a GB's interfacial energy, it also makes it loose mobility.

Segregation in the vicinity of GB creates solute rich atmospheres that can effectively hinder the motion of GB[60]. This effect, called solute drag, was experimentally verified by Weining and Machlin in 1957, after observing a fast decrease of the grain growth exponent, *n,* as the solute concentration increased [60, 66, 67]. This effect reached a saturation value, at which increasing alloying content no longer decreased the grain growth exponent. This exponent has the ideal value *n*=1/2 when no solute is added. The solute elements which distorted the matrix the most were found to have the largest effect. At higher temperatures, however, the effect is reduced, it is assumed that the solute atmospheres are broken by thermal vibration. Hence, precipitation remains the main tool for controlling growth.

3.1.4 Dissolution of Precipitates

During reheating, dissolution of alloying elements is important for homogenization purposes, so an optimal reheating treatment must be found between dissolution of precipitates and grain size control.

Precipitates' dissolution at reheating temperatures have the natural consequence of abnormal grain growth and grain coarsening. When precipitates dissolve, the only remaining force against GB motion, is solute drag. As explained before, solute drag force is not as strong as pinning force, especially at high temperatures (i.e. above ¾ of melting temperature). At these temperatures is well known that once precipitates dissolve grains will coarsen. Hence, precipitates' dissolution during reheating is a very relevant phenomenon to understand.

The phases present in an alloy at equilibrium, at a given temperature and pressure, can be determined by minimization of Gibbs free energy. Dissolution is governed by the chemical potential of elements in the existing phases. That is, the Gibbs free-energy change due to the addition of a unit mass of the component. Models that describe the alloy as regular solution sublattice and account for the total Gibbs free energy of the multicomponent system are commonly used. Additional energy from the mixing process is considered in these models, the entropy of mixing and the excess energy of mixing are important parameters to consider. The overall calculation is based on databases of Gibbs free energy of the possible phases in the alloy. These models are very accurate at predicting the amounts of each phase present in equilibrium conditions.

During reheating, however, it is uncertain whether equilibrium conditions are achieved. Factors such as geometry, atmosphere and soaking time largely vary, and influence the different dissolution processes. Hence, precipitates' volume fractions calculations based on Gibbs-free energy may not fit experimental data.

Another way to determine the volume fraction of precipitates is by utilizing the empirical solubility products of the precipitates. Numerous publications provide experimentally verified solubility product equations. Combining these with mass balance equations accurate calculations of the volume fractions present can be made. Especially if the solubility products were determined on similar alloys to that of interest. Based on precipitate volume fraction calculations, PAGS calculations can be made and a suitable reheating temperature chosen. Experimental verification of dissolution and grain size is necessary to avoid undesirable reheating results.

3.2 Hot Rolling

Hot rolling is the central stage of TMP. During hot rolling the final thickness is achieved, and the microstructure of austenite is conditioned for the final transformation. The hot rolling by CCR comprises two important operations: roughing rolling, under recrystallization conditions; and finishing rolling, under non-recrystallization conditions.

3.2.1 Austenite Deformation Under Recrystallization Conditions: Roughing

CCR roughing deformation has the purpose of providing bulk deformation while producing a refined austenitic microstructure. This is achieved by repeated cycles of deformation and recrystallization that iteratively produce finer grains in a similar fashion to Recrystallization Controlled Rolling (RCR). Well balanced microalloying is key in this strategy to prevent austenite grain coarsening while allowing Dynamic Recrystallization (DRX) or fast Static Recrystallization (SRX).

DRX is the nucleation and growth of strain free grains, that happens simultaneously with deformation. Deformation conditions control when DRX occurs. One way to summarize deformation conditions is through the Zener-Hollomon parameter, Z. Given by:

$$Z = \dot{\varepsilon} exp\left(\frac{402000}{RT}\right) \quad \text{(3-2)}$$

DRX occurs when the required steady state for DRX, σ_{ss}, is surpassed. According to Roucoules [68], this stress is defined by:

$$\sigma_{ss} = A\dot{\varepsilon} exp\left(\frac{Q_{def}}{RT}\right)^{q} \quad \text{(3-3)}$$

Where A is a constant for the material, A~7.2, Q_{def}=300kJ/mol for hot austenite, q=0.09[68], T, is the absolute temperature and R, is the universal constant of ideal gases. According to Siciliano, et al[68], DRX is very likely to occur in the first deformation passes given the high temperature.

SRX, the nucleation and growth of strain-free grains that occurs after a deformation, is driven by the introduced strain in the material. Hence, higher deformation passes are susceptible to produce recrystallization. Being a diffusional process, SRX is highly promoted by high temperature. Static recrystallization softens the material eliminating strain hardening, so an effective method for detecting SRX is by stress relaxation.

Stress relaxation can be detected when a second deformation is applied at the same temperature and after a determined interpass time. If the yield strength of the material is repeated, full recrystallization has happened. During CCR, roughing deformation is done under full recrystallization conditions.

CCR roughing deformation comprises most of the total rolling percent reduction of thickness, however, some deformation is reserved for the "finishing" stage. This is broadly accepted as a necessary measure to condition austenite. Common thickness reduction during roughing does not exceed 75% and finishing deformation is around 60%. It has been claimed that a 3:1 transfer bar to final thickness ratio must be used to produce adequate final properties. Nevertheless, having a thick transfer bar means suppression of grain coarsening at the center cannot depend on cooling only[69]. Once the recrystallization is completed, the structure is meta-stable and will attempt to coarsen to reduce surface area[70]. Precipitates that avoid coarsening must be present if a fine microstructure is to be produced during roughing deformation-recrystallization cycles.

3.2.2 Austenite Conditioning by Deformation under No-Recrystallization Conditions: Finishing

The purpose of deformation in non-recrystallization conditions is to achieve the final thickness and produce a highly dislocated structure, rich in nucleation sites for the final transformation. Deformation passes below Tnr accumulate strain in austenite and facilitate secondary phase formation. Non-recrystallization conditions are achieved, thanks to precipitation that happens as temperature decreases. This transition in recrystallization behavior is expected to happen at the transfer bar.

The production of an austenitic microstructure suitable for final transformation is known as austenite conditioning. In CCR, the combination of roughing grain size refinement, and finishing deformation accumulation, provides numerous nucleation sites. The amount of surface per unit volume, readily available for nucleation, is known as Effective Nucleation Area (Sv) and measuring it is one way to assess austenite conditioning. A high Sv promotes high ferrite nucleation rates that refine the structure, resulting in high yield strengths and toughness[50, 71, 72].

Austenite conditioning is influenced by microalloying elements through their ability to control grain size, recrystallization or stabilize austenite[72]. Austenite stabilizers allow the deformation of austenite at colder temperatures, where the recovery process is difficult. Ti and Nb carbonitrides are well known to have a pinning effect on GBs. This helps prevent grain coarsening and can dictate occurrence of non-recrystallization conditions. Hence, precipitation during hot rolling is of great importance.

3.2.3 Precipitation During Hot Rolling

During hot rolling, precipitates form as the material cools down and is deformed, these secondary phase particles play an important role in recrystallization and grain refinement. Precipitates existing before hot rolling are responsible for a fine initial austenite. During roughing rolling, new precipitates will form and are expected to allow SRX but inhibit grain coarsening. Niobium carbides are very effective at inhibiting recrystallization[69, 73]. Niobium carbides and carbonitrides formed in unstrained austenite have shown little effect in recrystallization inhibition. On the other hand, fine NbC formed through strain-induced precipitation show the most effect on recrystallization inhibition[74, 75]. Nb solute drag has proved ineffective for pinning austenitic grain boundaries[69]. Therefore, precipitation during roughing deformation is key for achieving the no-recrystallization conditions required in finishing deformation.

3.3 Transformation and Refinement of Structure

Microstructural refinement is of crucial importance for strength and toughness in LP steels. Acicular Ferrite (AF), is a constituent that offers fine grains and random crystallographic orientation, both necessary for high-strength and high-toughness. Deformation multiplies nucleation sites. Multiple nucleation of ferrite produces competition for austenite consumption during transformation. This produces refinement, especially when aided by fast cooling.

3.3.1 Ferrite Growth from Deformed Austenite

The kinetics of nucleation and growth of a new phase can be described by the Johnson-Mehl-Avrami-Kolmogorov (JMAK) equation:

$$\mathbf{1 - \varsigma = e^{-(\pi/3) J \dot{G}^3 t^4}} \qquad \textbf{(3-4)}$$

Where $\boldsymbol{\varsigma}$, is the volume fraction transformed of the new phase; $\boldsymbol{J}$, is the nucleation rate; $\boldsymbol{\dot{G}}$, is the growth rate of the new phase; and $\boldsymbol{t}$ is time. It can be observed the exponential dependence on time, nucleation rate and growth rate. Growth rate is heavily influenced by mobility, hence by temperature. Nucleation rate is influenced by austenite conditioning and the undercooling, $\boldsymbol{\Delta T}$.

Any high energy interface present in austenite is a suitable nucleation site for ferrite, and deformation provides many high energy sites. Deformation increases the γ/γ interface area through grain elongation. Deformation accumulates as dislocations pile-up and deformation bands, which have elastic energy associated to them. Twin boundaries existing before deformation can pile-up dislocations, increasing their surface energy and loosing coherency. Accelerated cooling provides big ΔT values, making nucleation numerous and limiting diffusion. Hence, accelerated cooling combined with highly deformed austenite must provide a strong and tough final microstructure.

Morphology of the final structure is dictated greatly by the nucleation location. Ferritic grains that nucleate on GBs grow faster on the GB direction and are known to adopt ellipsoidal shapes with approximate aspect ratio 3:1[23]. Ferrite that nucleates at twin boundaries present parallel rows of grains. Precipitation at deformation bands can also show grains arranged in lines. Whereas intragranularly nucleation produces AF, the finest and most randomly oriented ferrite.

3.3.2 Optimal Conditions for Acicular Ferrite Formation

Deformation and accelerated cooling favor AF formation. Intragranular nucleation sites can be provided by deformation bands, twin boundaries or stored deformation. Inclusions can also nucleate AF intragranularly, however are well-known to have a detrimental effect on toughness as crack nucleators, so one should be careful not to abuse their use. Accelerated cooling has proved to be beneficial to AF formation in several studies.

Previous research suggests that AF transformation mechanism is identical to that of bainite[36, 76]. This means AF formation comes at the expense of bainite since they are competing components. When AF is the desirable structure, one must be careful to facilitate the beneficial factors for its transformation. For instance, grain size should not be too small, some studies have found that small austenitic grain size favors bainitic transformation[76]. This is due to bainite's growth from pre-existing grain boundaries, while AF nucleates and grow intragranularly.

Besides nucleation, adequate cooling rates must be provided, down to a suitable holding temperature. The cooling must be fast enough to avoid the formation of pro-eutectoid ferrite, but slow enough to avoid massive martensitic transformation. High cooling rates affect transformation by lowering the critical temperature of transformation A_{r3}. Having a low A_{r3} also means the diffusion-controlled processes are slowed down, so processes like partitioning or precipitation become space-limited, resulting in finer structures.

Lan, *et al*[40] studied a HTP steel and noticed that as cooling rate increased to 15°C/s, the formation of AF was preferential to that of bainite. Zhao, *et al*[38] found 20°C/s cooling rate and 400°C isothermal holding, ideal for AF formation. Other authors claim that with deformation, cooling rates of only 3 to 10°C/s are enough to form AF[37, 42]. Deformation effectively induced the formation of AF in a study by Jun, *et al*[77]. Gu, et al[78] found that the AF forms above bainitic transformation, suggesting such isothermal holding.

3.3.3 Effects of Alloying Elements

Alloying elements in solid solution may promote or delay transformation during cooling, depending on whether they are ferrite stabilizers or austenite stabilizers. Mn, Ni, Cu and C are well known austenite-stabilizers, they lower the A_{r3} temperature. Lower A_{r3} temperature promotes suppression of pro-eutectoid ferrite and pushes transformation to colder temperatures, making finer structures.

Ferrite stabilizers promote ferrite formation at high temperatures, ferrite formed at high temperatures is mostly carbide-free and coarse-grained. Many ferrite stabilizers are also carbide formers. Elements that are carbide-formers or nitride-formers may increase the effective nucleation area by providing particle/matrix interfaces, if they already precipitated. Incoherent particles will promote nucleation due to their higher interface energy as compared to coherent particles.

3.3.4 Effect of Non-Metallic Inclusions in the Ferrite Formation

Non-metallic inclusions effects must be treated carefully to avoid misleading. Non-metallic inclusions provide nucleation surface for ferrite formation; hence, their presence can refine the ferritic structure. However, when toughness requirements are key, non-metallic inclusions are regarded as undesirable flaws due to their ability to initiate cracks. Non-metallic inclusions, if present, should be small and dispersedly distributed to have a positive effect on the final structure. AF nucleates intragranularly, so it has been showed that inclusions favor AF formation over bainite, which nucleates at boundaries. Unfortunately, achieving such state is not common during hot rolling. Soft inclusions become elongated and hard inclusions are often too big to be beneficial for the formation of a fine microstructure.

3.3.5 Precipitation During Cooling

During cooling, remaining precipitation can happen in multiple ways which dictate the carbide morphology and distribution. As ferrite forms, and if time is provided, the parent austenite enriches its alloying content. If this is the case, considerable amount of precipitation can happen in the last islands of austenite to transform[79]. Austenite keeps enriching as the transformation proceeds, with C as the easiest partitioning element, tiny islands of retained austenite may survive the transformation if the enrichment stabilizes them. When precipitation occurs during final cooling, three different scenarios may happen[23]:

a) Precipitation occurs during $\gamma \rightarrow \alpha$ transformation. Precipitates can nucleate at the interphase but grow on the ferritic side. As ferrite grows through a ledge mechanism, the precipitates that form in this scenario look aligned in rows.

b) Iron carbide forms, then it transitions to alloy carbide. As carbon is faster to partition during transformation, iron carbide forms first. But a lower Gibbs free energy is associated to the formation of the alloy precipitates. Hence, the already formed carbides transition into alloy carbides. However, time is key given the diffusion dependence and low temperature.

c) Precipitation occurs directly in ferrite. This scenario happens if partitioning of the alloying elements is achieved during transformation, that is, ferrite stabilizers move to ferrite in solid solution. Further holding to temperatures above 450°C can cause precipitation of these elements and reduction of the Fe_3C fraction. These precipitates are the smallest and most randomly distributed.

3.3.6 Texture Development

The preferential orientation of crystallites in the polycrystalline HSLA is an important factor that influences anisotropy, especially in impact toughness[46]. As explained in section 2.2.1, texture matters in fracture mechanics.

Ferritic texture after hot rolling is usually inherited from austenitic texture. Preferential orientation relations such as the Kurdjumov-Sachs (KS) are attained during the austenite-ferrite transformation[46, 79]. Research has shown how micro-texture in ferrite is result of the austenite-intragranular nucleation of ferrite[79]. Polygonal ferrite, on the other hand, nucleates mainly at GBs and have more random orientations. It follows that when cooling is slow, more polygonal ferrite will form, reducing texturization of the steel.

Texture generated during hot deformation of thick plates is quite different through thickness. This is due to the non-uniform distribution of shear stress during rolling[80]. A deeper penetration of deformation can be achieved using deformation passes with higher percentage of thickness reduction. Deeper penetration of deformation reduces strain gradients, providing a more uniform structure. Having smaller strain gradients can provide a more uniform grain size, microstructure and texture.

4.0 State of the Art

Mechanical requirements in line pipe steel products demand through-thickness homogeneity that can be challenging in commercial hot-strip mills. As the product thickness increases this becomes a more serious concern.

The Dropped Weight Tear Test (DWTT) standardized for impact toughness testing demands through thickness homogeneity. A fine and homogeneous structure is targeted for these impact toughness requirements. With this purpose, high amounts of deformation are used in the finishing passes. A typical 3:1 ratio is used between the transfer bar and the final product thickness. This conducts to low finish-rolling temperatures in the conventional HTP. These low temperatures and the amount of finishing deformation usually translate into low mill productivity. To allow higher finishing temperatures, the temperature below which full recrystallization does not occur (Tnr) is raised by adding Nb, which increases cost. As can be seen, there are many challenges involved with the current method of production.

The HTP of high strength-low alloy (HSLA) steel starts with the reheating of slabs. This is followed by hot rolling, and finally cooling to room temperature either by air or accelerated cooling. During the hot thermo-mechanical processing, the parameters that govern *grain size, texture* and *precipitation* are set. These microstructural features are determinant for the mechanical properties of HSLA steel. Small grains, for instance, increase yield strength and their numerous boundaries can be crack stoppers that improve toughness. Some textures may detriment toughness[46, 47]. Precipitates, meanwhile, slow down dislocation motion and provide strength, they must be small and coherent to avoid being crack nucleators. In general, controlling both grain size and precipitation is crucial for the steel properties.

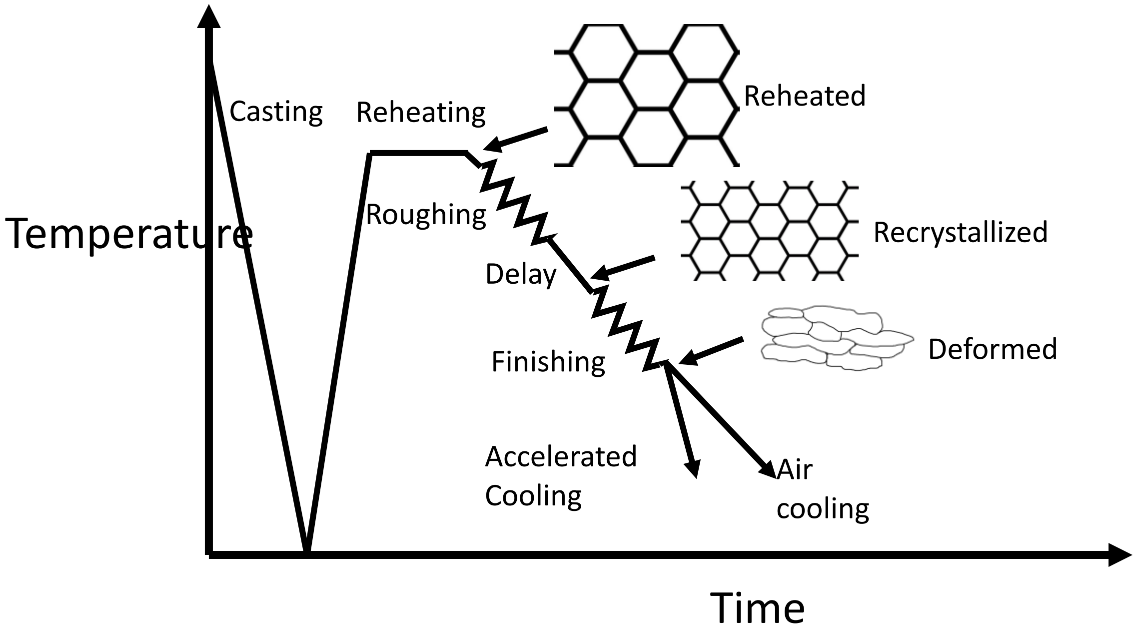

Figure 4.1. Schematic of hot rolling process and austenite structure. Adapted from [44].

Both grain size control and precipitation are benefited when some deformation is done under the non-recrystallization regime. The deformed non-recrystallized structure has a high dislocation content and provides numerous nucleation sites for precipitation, as well as for the new phases to form. Consequently, it is very important to have a non-recrystallization regime even when processing at high temperatures.

To guarantee a non-recrystallization regime in HTP, Nb additions are usually made. Due to carbo-nitrides boundary pinning and solute drag effects, Nb has been reported to slow down austenite boundary motion and recrystallization[62]. As can be seen in Figure 4.2, the effect of Nb on recrystallization retardation is remarkable when compared to other microalloying elements. However, its effectiveness comes to a price. Common Nb additions ranging from 0.08 to 0.15wt% considerably increase the cost of production.

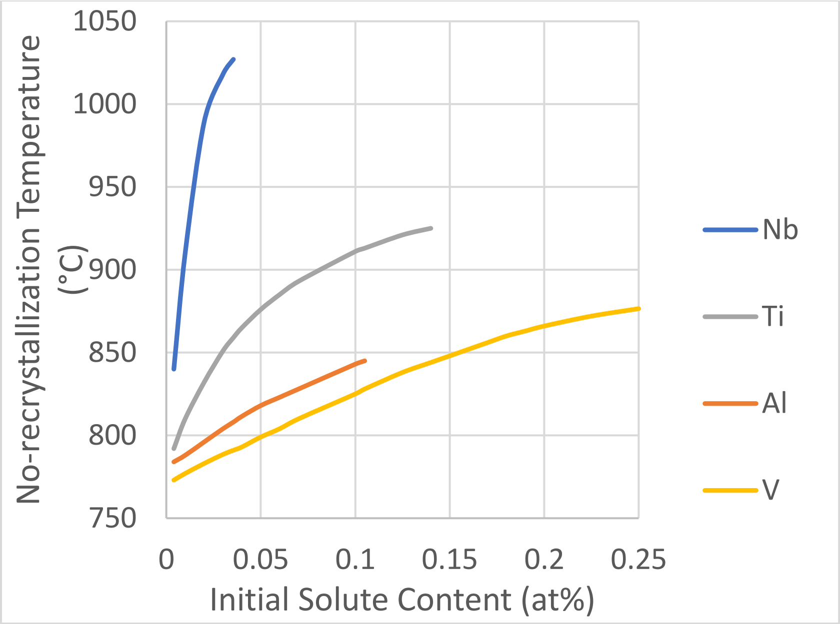

Figure 4.2. Effect of microalloy elements on the non-recrystallization temperature of austenite. Adapted from [81].

Limit I: The use of Nb represents high cost. New approaches that can reduce the Nb content can have an enormous economic impact and are a necessity.

Another important parameter to care about, is the austenite grain size. One must control the grain size of austenite, the parent phase of the final structure, to control the final grain size. This should be done first during reheating. The reheating of slabs is the preparation for hot deformation, it serves the purpose of homogenizing temperature and chemical composition in the slabs. The reheating process fully transforms steel to austenite. After deformation, austenite transforms into phases like ferrite, bainite and martensite during cooling. The mechanical properties of these final constituents improve with small prior-austenitic grain size (PAGS). Martensite, for example, has smaller laths and is stronger when the PAGS is small[82]; it also forms at lower temperatures[83, 84]. Fine PAGS increases strength of pearlite by producing small colony size[85] and similarly happens with ferrite grain size[8]. The big importance of reducing grain size is that is the only strategy that simultaneously increases both strength and toughness, so it is imperative to keep grains small.

To keep a small austenitic grain, it is common to use microalloying elements such as Ti, V and Nb to form carbides. These carbides exert forces on the austenite grain boundaries and eventually balance out the driving force for growth[1, 60]. For this grain growth inhibition to be effective, a large volume fraction of fine stable precipitates must exist[86, 87]. That is, the pinning force due to precipitation must be higher than the driving force for grain coarsening, $F_{pin}>F_{GC}$.

The reheating of slabs for HTP is usually done at temperatures which dissolve most of the carbide and nitride particles. Later, when rough deformation has taken place, new carbides are expected to precipitate to prevent austenite recrystallization.

Limit II: A deformation schedule is needed, that improves NbC precipitation kinetics at the transfer bar, that is, between roughing and final deformations.

4.1 Hot Deformation Limitations

The two goals in hot deformation are, first, to shape the steel, and second, to facilitate the development of the desired final microstructure. Interestingly, these goals are very dependent on the previous step in the process, reheating. During the reheating of slabs, attention must be given to the following parameters, which have strong influence on the hot deformation process[44]:

Austenitic grain size. A small austenitic grain size increases the flow stress during hot rolling, dificulting the operation. Small PAGS also reduces templability by providing more nucleation sites for ferrite. On the bright side, small PAGS reduces crack formation during deformation and conduces to fine ferritic grains during cooling, so the desirable conditions are to have small PAGS for hot rolling.

Dissolution of precipitates. Precipitates also increase the flow stress during hot rolling. This translates into high energy consumption and reduces the life of the rolls. Hence, it is desirable to dissolve most precipitates before the hot deformation. To guarantee full dissolution of precipitates, thermodynamic calculations of their volume fraction as a function of temperature can be made based on the known solubility products of the precipitates involved. These calculations can in turn be used for predictions of mean flow stress and prior austenitic grain size in equilibrium conditions.

Temperatures of recrystallization and non-recrystallization. The rolling temperature plays a crucial role on precipitation and recrystallization[88]. Rough hot deformation, or so called "roughing", is done under recrystallization conditions. "Finishing" deformation, in contrast, it is preferred under non-recrystallization regime. The high temperature stage facilitates deformation; while the low temperature stage, below the temperature of non-recrystallization, provides numerous nucleation sites, and hence a desirable very fine structure[88]. In other words, the deformations above Tnr do not influence significantly the microstructural changes that affect the transformations to the final microstructure[89]. The fine structure of acicular ferrite, for instance, forms almost exclusively from deformed non-recrystallized austenite[90]. From this, it is evident that recrystallization conditions are very important to know when hot deforming. These conditions depend on temperature and alloy content but also on the amount of deformation.

Deformation provides the driving force for recrystallization, so it is limited for a given composition and temperature when non-recrystallization conditions are required. Tnr is decreased when strain and strain rate are increased. Tnr is affected by alloying too, Nb has been observed to retard austenite recrystallization when present in solid solution[62, 73]. Tnr is also influenced by the interpass time between deformations. Interpass times lower than 12 seconds can decrease Tnr. Interpass times between 12 and 50 seconds increase Tnr due to increasing volume fraction of precipitates. While interpass times beyond 50 seconds can decrease Tnr due to precipitate coarsening[91]. The balance temperature-composition-deformation can be described by the Zener-Hollomon parameter. The Zener-Hollomon parameter is a measure of the relation strain-rate to temperature and helps determine dynamic or static recrystallization conditions[92]. On the low temperature side of the story, deformation at non-recrystallization conditions allow for massive nucleation sites and a finer microstructure. From all this recrystallization relations, one can observe why high-temperature deformation is beneficial for productivity, but low-temperature finishing deformation is good for properties.

Limit III: The high finishing temperatures required to improve mill productivity often struggle to provide the strength and toughness, especially in thick sections. A strategy that can achieve toughness while exploiting the benefits of high temperature deformation is required.

4.2 Solute Drag and Precipitation Control Limitations

The strengthening effect of carbides and nitrides is essential to steel, so their formation needs fine control. Carbides and nitrides precipitate first from liquid steel during casting. Most of these precipitates dissolve during slab reheating. Later, new precipitates may form due to temperature-drop and introduced dislocations during hot deformation. These particles effectiveness as strengtheners depends on their final size, which must be nanometric, their high volume fraction and their disperse distribution[86]. All these properties must be procured during reheating and during hot deformation.

Precipitation control during reheating. Some precipitates dissolve during reheating, while some are preserved for PAGS control purposes. Particles like TiN are among the last to dissolve, given their stability at high temperatures. To preserve precipitates, the homogenization temperature must be chosen below their dissolution temperature.

Solute drag. Alloying elements atoms are attracted by grain boundaries due to the distortion present in them. Grain boundary lattice distortions generate stress fields in the surroundings, these fields can interact with the impurity elements. The microalloying atoms exert a drag force on the boundary[93]. This effect may be exploited during deformation, for recrystallization retardation of austenite. Nb is one of the microalloying elements that has demonstrated this kind of effect, retarding recrystallization of austenite due to segregation near grain boundaries[62]. The solute drag effect is the first mechanism used for recrystallization retardation during hot deformation. As the material cools down, the segregated alloying elements nucleate precipitates, only then, precipitates become the main inhibitors of boundary migration.

Precipitation control during hot deformation. Precipitates are required in the final microstructure, and after hot deformation is the last chance to form them before the alloy is rapidly cooled to room temperature. Carbide particles are stabilized as the material cools down due to the diminishing of solubility product. Some particles may still require activation energy (i.e. nucleation sites) to precipitate though. This activation energy can be provided by the deformation process whenever it is done below the non-recrystallization temperature. A good example of this deformation-aided precipitation process is NbC particles. These particles have been observed to precipitate in two stages at temperatures around 900°C. First, precipitation at deformation bands and austenite grain boundaries. Second, precipitation induced by deformation-generated dislocations[73]. The latter type of particle formation is highly desirable, given its fine distribution across the grains. Epitaxial precipitation of NbC happens on preexisting TiN, according to Ma *et al*, diminishing the strain induced precipitation of NbC [94]. In their experiments, this epitaxial growth when the interspacing of TiN is less than 300nm happens to raise the austenite recrystallization stop temperature more efficiently than strain-induced NbC. NbC particles are more effective at retarding recrystallization, whereas TiN particles are not capable of doing so[63].

The finish rolling temperature has been found to reduce the precipitation hardening, however it enhances other strengthening mechanisms such as grain refinement[95].

Precipitation during coiling: Coiling at an appropriate temperature is also an opportunity for harnessing precipitation strengthening. Our preliminary study, as well as other authors have found coiling temperatures to have a special effect on strength[96].

Limit IV: High finishing temperatures do not promote the formation of precipitates as well as low temperatures. Harnessing the potential for higher precipitation strengthening at high temperatures is a challenge.

4.3 Real Case Analysis

We can relate all mentioned limits of current practice to the real case presented next. This case regards 3 different plate steel products (19mm thickness) that complied with tensile properties, yet most of them failed to comply with toughness requirements at low temperatures. Only one of the products showed good toughness and strength. This product also happened to have a very low Nb content (0.045wt%), providing evidence that mechanical requirements can be achieved for this type of steel without the high Nb contents.

On Figure 4.3 we can notice how the tensile properties of all three high-temperature-processed steel products are consistently similar. However, the toughness of the HH and AR materials shows considerable embrittlement at low temperatures.

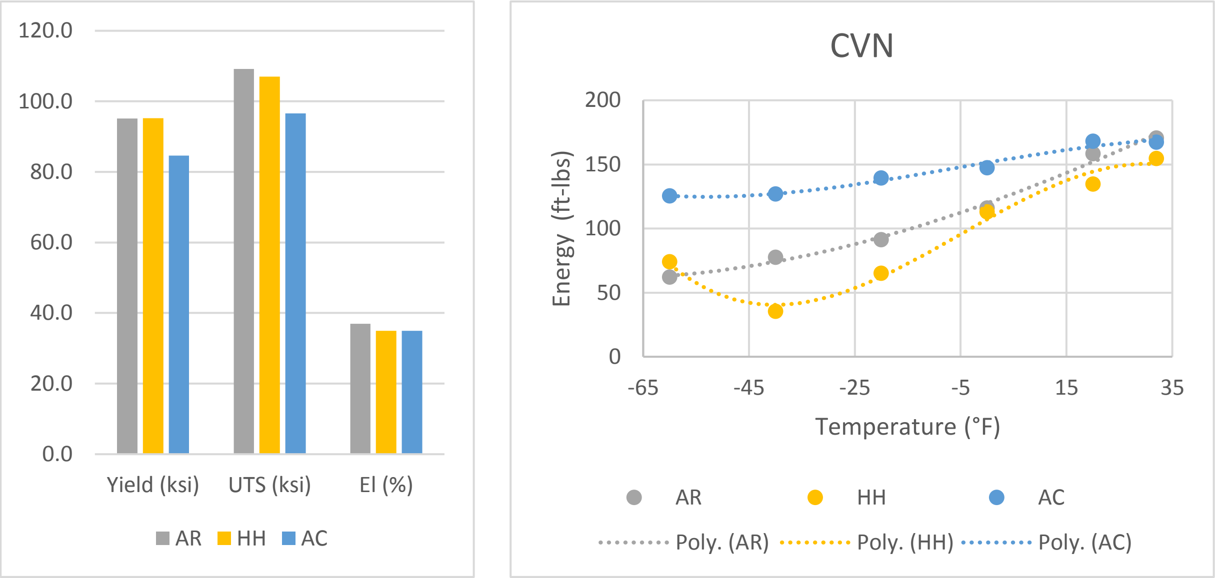

(a) (b)

Figure 4.3. Mechanical properties from the real case of 5 steel plate products: (a) Tensile properties; (b) Absorbed energy in Charpy impact test.

The mechanical characterization of these materials was contrasted to many process variables, resulting in the following observations: First, a low Nb alloy can achieve the required DWTT toughness. Second, there is an apparent maximum of toughness related to a critical finishing temperature. Third, contrary to most work reports[88, 95, 97], in these preliminary materials lower finish rolling temperature produced lower yield strength. The opposite is the normal tendency, however, experiments with independence of finishing rolling temperature to final yield strength have been reported when accelerated cooling is applied[97]. On the other hand, the observed contrasting behavior could be an indication that the finish rolling temperature was in the intercritical range for these industrial processes. Fourth, there is a critical coiling temperature that maximizes yield strength. This could be due to conditions that favor precipitation kinetics.

5.0 Research Approach

5.1 Objectives and Hypothesis

Objectives

1. Optimize precipitate formation and microstructure for strength and toughness higher than similar commercial alloys with special focus on thick products (19mm).
2. Develop a new, effective and robust high temperature process for thick linepipe steel through Intensive Recrystallization-controlled Rolling.
3. Reduce alloy content costs while effectively achieving microstructural optimization.

Hypothesis

The precipitation and grain refinement required for the strength and toughness of a linepipe steel can be achieved by means of a new hot deformation approach. This approach consists of a very high deformation at recrystallization conditions and a reduced amount of micro-alloying additions. Lower finishing reductions, higher finishing temperatures and accelerated cooling can improve toughness in thick products.

If this hypothesis is true, we can achieve our goal. The strategy to achieve the general goal of this work addresses the four identified limits of current practice from section 4.0 by proposing three key studies. First, a study of austenitic grain coarsening behavior. Second, a study of recrystallization behavior. Finally, a study of precipitation behavior and microstructural control through the proposed deformation process.

5.2 Intensive Recrystallization-Controlled Rolling (IRCR)

The proposed process consists of a higher deformation applied during “roughing”, in recrystallization conditions; followed by a lower deformation in “finishing” in no-recrystallization conditions, and faster cooling as compared to the conventional recrystallization-controlled rolling. Innovations in the intensive process were implemented to test specific aspects of the hypothesis.

The higher amount of roughing deformation comes with two benefits. First, it allows to have a thin transfer bar that can cool faster and reduce the time to cool down to non-recrystallization conditions. Second, it eliminates dead time, instead of just waiting for Tnr to be achieved, the deformation process continues. Combination of these two benefits allows to have a lower Tnr of the alloy, that is, a lower Nb content can be used.

The lower deformation during finishing is a consequence of the high deformation during roughing. Low deformation under non-recrystallization conditions derive in fewer nucleation sites for final transformation. However, if this deformation is done at the lowest temperature possible above A_{C3}, it is expected that recovery will be minimized. Deformation-generated dislocations could then nucleate a fine microstructure aided by fast cooling.

Fast cooling is then key for success of this process. It will help provide more nucleation sites and accomplish acicular ferrite microstructure. As explained before, acicular ferrite is our target microstructure due to its characteristic strength and toughness, so the cooling rate is 15°C/s down to 550°C.

A comparison of the deformation processes is provided in Figure 5.1 Temperature-time schematic comparison of conventional to intensive recrystallization controlled rolling. both processes are presented as they would be in a typical mill with 5 roughing stands (R1 to R5) and

7 finishing stands (F1 to F7). Notice that the conventional deformation schedule uses longer times and higher T_{nr}, because it is thought for higher Nb.

The total cumulative deformation for both processes is 92%, however, the distribution of the deformation is a major difference. The amount of deformation occurring above T_{nr}, in recrystallization conditions is 85% for the IRCR process, as compared to 75% for the conventional process. Similar at first sight, these two roughing approaches produce very different transfer bar thicknesses. The conventional process produces a transfer bar three times thicker than the final thickness. Whereas the IRCR process produces a transfer bar slightly less than twice as thick as the final product. The thinner transfer bar shortens the time to cool below Tnr, allowing for faster production and lower Tnr.

Notice that IRCR uses traditional finishing stands to add passes to the roughing deformations and skips a few finishing stands. The roughing deformation starts in stand R1 and is completed at stand F2. The skipping or "dummying" of F3, F4 and F5 stands is thought to give time for precipitation and transition to no-recrystallization conditions. This eliminates deadtimes as compared to the CCR process, where a thicker transfer bar takes longer times to cool down to no-recrystallization regime. This is the reason the projected time for full process in IRCR is shorter than CCR.

A more detailed schematic of the distribution of deformation in both processes is presented in Figure 5.2. Notice how the finishing deformation in the conventional process uses many passes, distributing deformation evenly among them. The IRCR process uses less final deformation, however, it applies it at the lowest temperature possible in only two passes. This allows for deformation to go deeper and have a more homogeneous result. The low temperature provides a barrier for recovery, preserving dislocations for nucleation of the final micro-constituents.

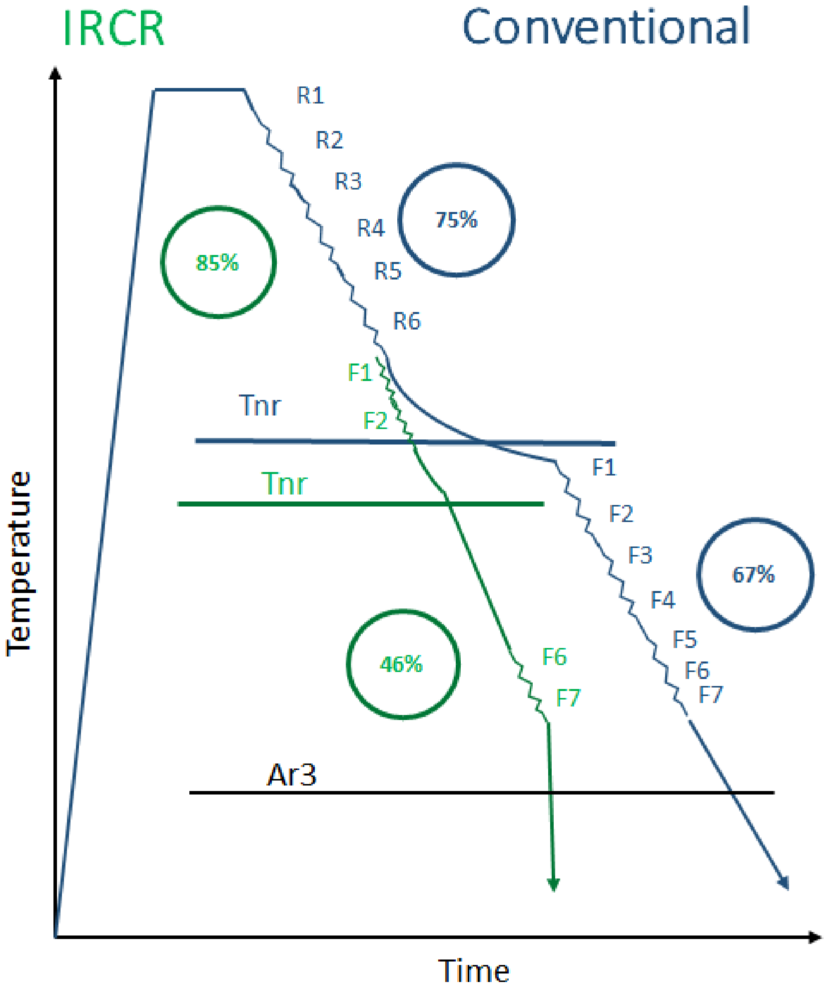

Figure 5.1 Temperature-time schematic comparison of conventional to intensive recrystallization controlled rolling.

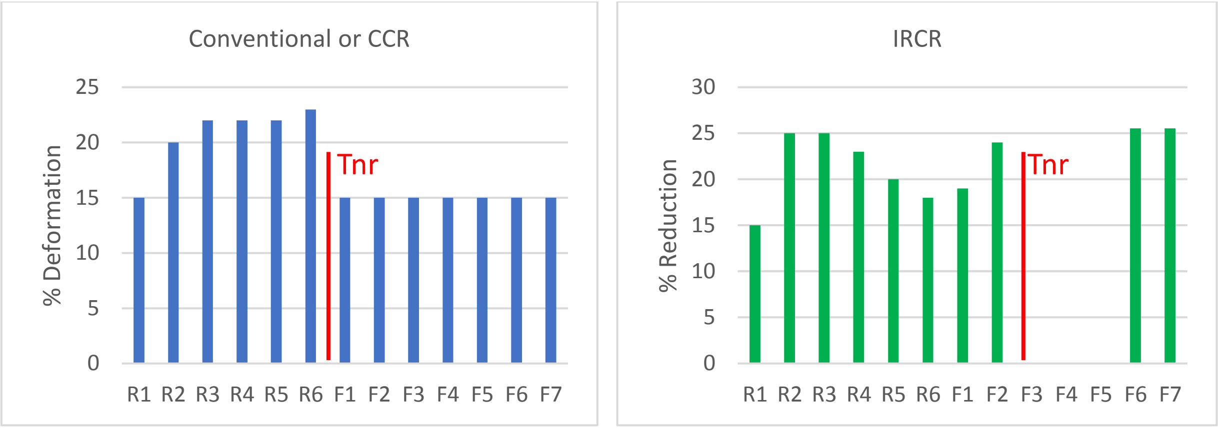

(a) (b)

Figure 5.2 Deformation schedule comparison between (a) Conventional Controlled Rolling and (b) Intensive Recrystallization Controlled Rolling.

5.3 Alloys' Selection

Three alloys were used, with Nb content as the only contrast. Nb slows recrystallization at high temperatures. Dynamic recrystallization requires higher deformations in Nb-bearing steels as compared to Nb-free steels at a given temperature[74]. Static recrystallization requires longer times in Nb-bearing steels. The mechanisms responsible for this behavior may be precipitate pinning of boundaries or solute drag effect[74]. The recrystallization retardation effect of different Nb content steels was of great importance in this study. The composition is shown in Table 5.1.

Table 5.1 Compositions (wt%) of the three used alloys.

Alloy	C	Mn	Cu +Ni +Al	Cr	Nb	Mo + V	Ti	N	Si
High-Nb	0.05	1.5	<0.4	0.25	0.09	<0.25	0.01	0.007	0.25
Med Nb	0.05	1.5	<0.4	0.25	0.07	<0.25	0.01	0.007	0.25
Low Nb	0.05	1.5	<0.4	0.25	0.05	<0.25	0.01	0.007	0.25

Three alloys were laboratory produced: The first with 0.09wt% Nb, then two modifications with lower Nb content were added. The lower Nb content is crucial part of this study. The mechanisms and phenomena studied during hot-processing aim to achieve enhanced microstructure with low Nb content.

Other alloying elements were left the same as in High-Nb steel. The High-Nb steel is based on a commercial HTP steel and is the basis of comparison to our proposed Low-Nb alloy. The Med-Nb steel was only used for verifying trends, when necessary.

5.4 Austenitic Grain Coarsening Behavior and Dissolution

The challenge in grain size control is to be able to avoid grain coarsening, despite the low alloy content. A systematic study of austenitic grain growth was conducted. The secondary phase particles pinning effect was expected to vanish at a certain temperature when the particles dissolved. This temperature then served as a reference to decide the austenitization temperature and soaking time. The optimal austenitization temperature prevented abnormal growth, this helps homogeneity of mechanical properties. The austenitization temperature must also allow for dissolution of most alloying elements, so they can precipitate homogeneously.

Methods: Thermodynamic calculations of precipitates volume fractions first helped choose the temperatures for these experiments. For the austenitic grain growth study three different austenitization temperatures were tested, 1150°C, 1200°C and 1225ºC, each with two different soaking times, 30 and 60 minutes. The samples were quenched immediately after the austenitization soaking time was completed. The austenitic grain size was revealed by tempering plus picral etching and was corroborated by Electron Back-scattered Diffraction (EBSD) mapping of quenched samples. Verification of grain size was also done by thermal grooving[98]. The use of EBSD mapping also allowed to characterize the grain boundary character distribution (GBCD) evolution through different austenitization conditions.

By analyzing the timeline of grain size for a given reheating temperature, one can determine whether there is influence of precipitates. We compared the evolution of grain size at different temperatures, the dissolution temperature of precipitates was evidenced by the appearance of abnormal growth. This dissolution evidence was supported with the use of High-Resolution Transmission Electron Microscopy (HRTEM), and electron diffraction.

5.5 Deformation and Recrystallization Behavior

This study had the purpose of experimentally determining Tnr, and MFS at the temperatures of interest. Also, compare the results of the two different roughing processes of CCR and IRCR. This study comprised first, the calculation and experimental verification of Tnr and mean-flow stress (MFS). Second, the execution of two roughing schedules devised with different amounts of deformation. The following deformations were used 75% and 85% total thickness reduction above Tnr.

The MFS, the stress necessary to keep deforming steel was theoretically calculated using Misaka, *et al* equation (See Equation 5-1), while the experimental value, MFS_{exp}, was obtained using Equation 5-2 on the hot compression test results.

$$MFS = e^{\left(0.126-1.75[C]+0.594[C]^2+\frac{2851+2968[C]-1120[C]^2}{T}\right)\varepsilon^{0.21}\dot{\varepsilon}^{0.13}} \tag{5-1}$$

$$MFS_{exp} = \frac{1}{\varepsilon_1-\varepsilon_0}\int_{\varepsilon_0}^{\varepsilon_1} \sigma \, d\varepsilon \tag{5-2}$$

Third, an evaluation of the post-deformation conditioning of austenite by means of microstructure, grain morphology, dislocation density, effective nucleation area (Sv) and texture. The austenite was evaluated after the first deformation that did not show full recrystallization. A heavily deformed austenite was obtained. The Sv of deformed austenite was used to correlate deformation to microstructure nucleation. The Sv value helps quantify the nucleation opportunities for precipitate formation[41]. In general, this deformation study allowed for comparison of experimental information to models for: recrystallization force, pinning force, solute drag and nucleation sites formation.

Methods: Using the three alloys shown in Table 5.1. Deformations were made at a Gleeble 3500-317 thermomechanical system. Specimens were rectangular prisms 15x15x20 mm. The specimens were solution-treated to 1200°C for 60 minutes and quenched, in preparation before the deformations took place. Then the specimens were reheated to 1225 for 5 minutes and subjected to hot plane-strain compression by wedge-like dies at the Gleeble system, using different deformation schedules.

There were two different deformation experiments of hot compression (See Table 5.2). The first was designed to determine MFS and Tnr experimentally. This consisted of an eight-hit 0.2 strain reiterative deformation as the sample was cooling down every 25°C from 1050 to 950°C. Whenever non-recrystallization conditions are achieved; the strain hardening must be higher during deformation. The second experiment was designed to simulate the roughing deformation.

This consisted of eight roughing steps, comparing the conventional 75% roughing reduction, to an intensive 85% roughing. Samples were quenched after roughing simulations to evaluate austenite conditioning.

Table 5.2. Experiment for determination of temperature of non-recrystallization and mean-flow stress.

	T (°C)	%Reduction	Strain rate (1/s)	Interpass time (s)	Cumulative %Reduction
Def1	1050	20	1	20	20
Def2	1025	20	1	20	36
Def3	1000	20	1	20	48.8
Def4	975	20	1	20	59
Def5	950	20	1	20	67.2
Def6	925	20	1	20	73.8
Def7	900	20	1	20	79
Def8	875	20	1	20	**83.2**

Table 5.3. Experiments simulating roughing deformation.

		%Reduction with respect to original size		%Reduction with respect to every stand	
		CCR	**IRCR**	**CCR**	**IRCR**
Above Tnr	R1	15.00%	15.00%	15	15
	R2	32%	36.25%	20	25
	R3	46.96%	52.19%	22	25
	R4	58.63%	63.18%	22	23
	R5	67.73%	70.55%	22	20
	R6	75.15%	75.85%	23	18
	F1	-	80.44%	-	19
	F2	-	**85.13%**	-	24

For a partial preservation of the microstructural conditions most specimens were quenched with the system's water-cooling tool. The quenched specimens were then characterized. They were etched with picric acid saturated solution to reveal the austenitic structure. Optical microscopy (OM) was the first-hand tool to analyze austenite and determine its recrystallization status by observing grain size and morphology. We confirmed the degree of recrystallization and texture analysis using electron backscatter diffraction. EBSD mapping allows measurements of image quality, which is related to dislocation density; texture and grain boundary character. Relating these data to the Nb content, the recrystallization effects were assessed.

5.6 Transformation and Precipitation During Deformation, Cooling and Coiling

The purpose of this study was first, to prove that Low-Nb + IRCR can provide a suitable austenite conditioning for optimized final transformation. Second, that coherent fine precipitates can form during and after deformation, that enhance strength. And third, that low finishing deformation combined with accelerated cooling can provide the fine acicular ferrite needed even in thick products. The use of low alloy in HTP steel is a new approach, hence these transformation studies were of great importance.

This study gathered and analyzed data related to development of the final microstructure and the precipitation kinetics of the alloying elements. That is, temperature of dissolution and deformation induced precipitation behavior. We identified volume fraction, size, coherency, morphology and preferred nucleation sites. Then we used all this data to make our process produce the fine precipitates that we needed for high strength and toughness.

The desired final microstructure must be tough. This translates on to characteristics as having a small effective grain size, high angle grain boundaries, etc. Therefore, as explained in section 2.2.3, our target microstructure was acicular ferrite.

One good way to obtain acicular ferrite is through deformed austenite combined with accelerated cooling[78]. Cooling rates of at least 15°C/s have been necessary to produce AF in similar steels[40]. Deformation promotes AF formation[40, 41], it has been observed that on deformed samples only 5-10°C/s cooling rates are enough to form AF[37, 39, 42]. To be able to produce acicular ferrite in thick products, we combined a highly deformed structure with a cooling rate of 16°C/s.

Methods: Hot torsion tests were done to physically simulate the roughing and finishing deformation. A Gleeble 3500 machine was used for the torsion tests and controlled cooling rates. The objective of these final experiments is to develop toughness through thickness by microstructure refinement and precipitation control. The resulting samples were characterized using SEM, TEM and EPMA to identify, analyze and assess the precipitation behavior of the alloys. Samples from austenitization, and hot deformation studies were analyzed as well to obtain a full precipitation behavior through the whole process.

Deformations were made using 75 and 85% reduction in recrystallization conditions, called "roughing" (R) and 57 and 46% reduction in no-recrystallization conditions, deformation called "finishing" (F) (See Table 5.4). Both deformation schedules were applied to the High-Nb and the Low-Nb alloys. After the final deformation, the specimens were water-quenched. The deformed samples were characterized to determine austenite conditioning. The analysis of these specimens compared the deformed austenite structure, as well as volume fractions of carbonitrides, and their size distribution.

Table 5.4. Torsion deformation schedules.

			% reduction per stand	
	T (°C)	Stand	75% R + 57% F	85% R + 45% F
Roughing: From 1200°C to experimental Tnr	1200	R1	15%	15%
		R2	25%	25%
		R3	25%	25%
		R4	23%	23%
		R5	20%	20%
		R6	18%	18%
		F1	15%	19%
	Tnr+10°C	F2	15%	24%
Below experimental Tnr but above experimental Ar3		F3	15%	Dummy
		F4	15%	Dummy
		F5	15%	Dummy
		F6	15%	25.6%
	Ar3+20°C	F7	15%	25.6%

5.6.1 Validation Experiments

A final validation was done utilizing an experimental mill. This compared the CCR process to the IRCR on both alloys. The deformation schedules had to be simplified to be able to execute the deformation in the experimental single-stand reversible mill. Plates of 0.75in thickness were targeted starting from 3.5in thick slabs previously obtained from 7in ingots. Accelerated Controlled Cooling (ACC) was applied followed by furnace cooling. The schedules are shown on Table 5.5 and Table 5.6.

Table 5.5 Simplified CCR process.

Tin (°C)	% Reduction	
1200	Reheating	
1050	35.7	Roughing
925	24	Finishing T<Tnr 67%
900	24	
875	24	
850	24	
550	Coiling	

Table 5.6 Simplified IRCR process.

Tin (°C)	% Reduction	
1200	Reheating	
1100	18	Roughing T>Tnr 61%
1070	27	
1040	35	
910	26	Finishing T<Tnr 45%
880	26	
550	Coiling	

Immediately after rolling, specimens were conveyed through a water spray to reach 550°C at a cooling rate of approximately 16°C/s, previously experimentally tested. Then the specimens were furnace cooled to simulate the slow cooling of a coil. The deformation experiments were repeated, this time followed by quenching, for analyzing the deformed structure. Infra-red pyrometers were located at both sides of the rolling stand for temperature monitoring. The interpass cooling was natural convection. A set of contact thermocouples were used right after the cooling bed to verify the final surface temperature.

The microstructure from the resulting specimens from ACC + furnace cooling, was characterized and the mechanical properties tested. The microstructure was analyzed by OM, SEM and EBSD to determine texture, GBCD and precipitation distribution. On the mechanical side, microhardness, tensile tests and Charpy V-notch impact tests were used to assess strength and toughness.

5.7 Equipment and Techniques

Experiments were performed at University of Pittsburgh Ferrous Physical Metallurgy group laboratory and at United States Steel Corporation (USS) research facilities at Homestead, PA. The melting and casting of the laboratory heats was done at USS research facilities, as well as hot deformations and carbon replica coatings. The reheating simulations and all characterization was performed at University of Pittsburgh facilities.

5.7.1 Reheating Simulations

Specimens were cut in pieces of approximately 1cm X 1cm X 1cm using a cool cut in a horizontal saw. After being washed and dried, the specimens were encapsulated in quartz tubes under moderate vacuum. The vacuum was alternated with Ar filling 5 times to ensure an inert environment inside the capsule before it was finally sealed in vacuum. One piece from each chemical composition was put in every capsule.

The capsules with the three alloys -were then austenitized at 1150°C, 1200°C, 1225°C, 1250°C and 1300°C for 30 minutes and 60 minutes soaking times. The time was counted after the furnace recovered the set temperature after loading the capsule. The furnace used was a calibrated Sentro Tech Corp ST-1500C-121216 and its temperature reading was compared to a K-type thermocouple with an external reader to verify the precision of temperature control right before the samples were inserted.

The capsules were quenched in ice brine immediately after the soaking time was reached. The thermal shock combined with the vacuum pressure in the capsules made them implode at the contact with the quenching media. The mixture was agitated for ten seconds in an eight-shaped pattern to guarantee continuous removal of locally heated water.

5.7.2 PAGS Revealing and Reconstruction

Three techniques were used for revealing PAGS in the reheating simulation samples. The first, was by picric acid solution, the second through EBSD mapping, and the third by thermal etching. The picric acid solution was prepared by heating 100 ml of distilled de-ionized water to 90°C, picric acid was added until saturation, 2g of sodium dodecylbenzenesulfonate and 6 drops of hydrochloric acid. The samples were tempered at 600°C for 24h before etching for revealing PAGS. The tempering process was intended to cause P segregation to PAGB. The samples were polished, cleaned and immediately etched by immersion and swabbing for 1-2 min.

Micrographs were taken using a Keyence Microscope Flexible Optical Microscopy and Metrology Platform, see Figure 5.3. The measurements were done by circling the perimeter of individual grains and obtaining from the software the Feret diameter for later averaging this value.

Figure 5.3. Micrograph of alloy 0.091%Nb austenitized to 1225°C per 60 min and etched with picral solution.

A separate set of austenitized-quenched specimens was not tempered. Instead, the martensitic specimens were ground and vibro-polished for EBSD orientation image mapping (OIM). EBSD maps were acquired as detailed in section 5.7.5. Post processing of the martensitic maps used MTEX Matlab toolbox and the method developed by Nyyssönen, *et al.*[99] for re-constructing prior austenite grains (PAG). This method introduced elsewhere[99-102], determines the experimental orientation relationship (OR) from martensite to its parent austenite. It starts by assuming the well-known Kurdjumov-Sachs OR and iteratively compares adjacent grains to determine the experimental OR. The experimental OR is then used along a graph-clustering algorithm by van Dongen[102] for re-constructing the PAG map (see Figure 5.4), considering all 24 possible parent orientations for every point. Further processing of the generated PAG EBSD files was done in MTEX for generating KAM and GB maps.

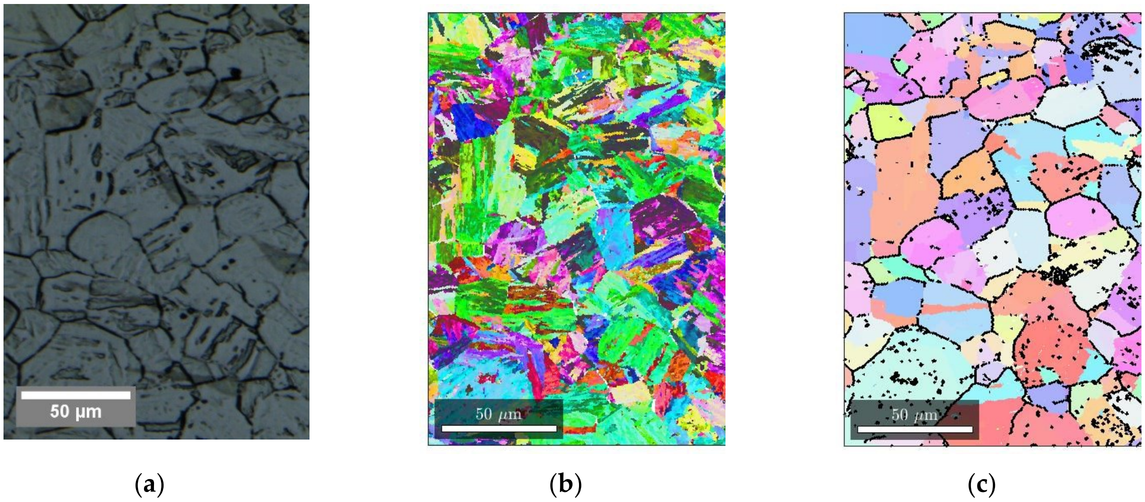

(a) (b) (c)

Figure 5.4. Comparison of the reconstructed PAGS map to a picral etched micrograph. (a) Micrograph after picral etching; (b) EBSD OIM map from quenched specimen; (c) reconstructed OIM map of austenite, based on (b). High-Nb sample austenitized to 1150 °C for 1 h.

Thermal etching was used only as a verification technique for the selected reheating temperature of 1200°C per 60 minutes, see Figure 5.5. The surfaces of interest were first polished, then the specimens were washed, cleaned and encapsulated in vacuum quartz tubes. The capsules were then austenitized to 1200°C per 60 minutes and immediately quenched in ice brine. The PAGS was observed by optical microscope Zeiss SmartZoom 5 and measured using the free software ImageJ. Fifty grains from each alloy were measured as a representative sample. The drawback of thermal etching is that the surface is known to interact with the boundaries, reducing the significance of its results.

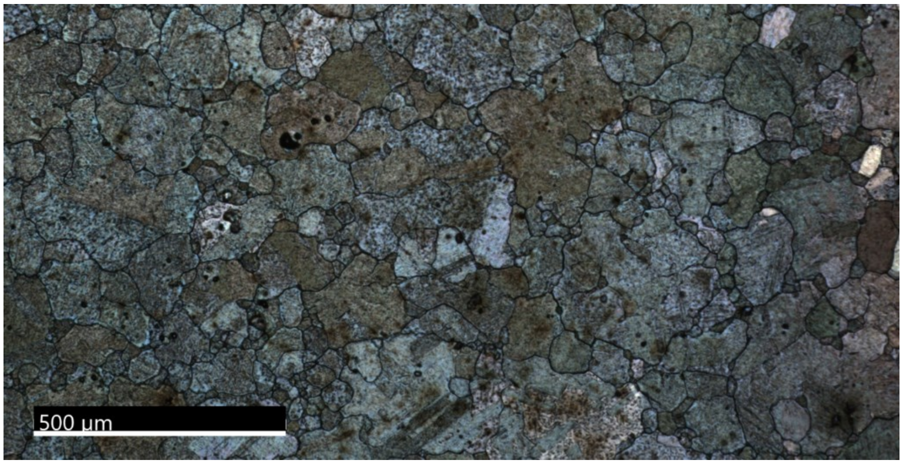

Figure 5.5. Micrograph of thermo-etched alloy with 0.05% Nb austenitized to 1200°C per 60 minutes in vacuum.

5.7.3 Electron Microscopy

Scanning electron microscopy observations were conducted on a Zeiss Sigma 500VP field emission gun SEM equipped with Oxford Aztec EDS detector. This tool was used mainly for the first assessment of precipitation, using magnifications from 50 000X up to 300 000X and resolving particles of tens of nanometers. For energy dispersive spectroscopy (EDS), a 20kV beam was used and the detection conditions were consistently: 0-20KeV energy range, 2048 channels, process time 5, and 200 000 counts.

Transmission electron microscopy was done in a JEOL JEM2100F microscope, using 200kV. This microscope was equipped with double-tilt holders, EDS detector and CCD camera.

5.7.4 Scanning Transmission Electron Microscopy (STEM)

A Zeiss Sigma 500VP field emission gun SEM with STEM capabilities was used. The specimens were as prepared for TEM and mounted on a revolver specimen holder with 6 positions. This technique was only used for faster exploration of thin foils, before TEM analysis.

5.7.5 Electron Backscattered Diffraction (EBSD) Mapping

The samples for EBSD were first polished manually. Then vibro-polished at 65Hz in a GIGA 0900 Vibratory Polisher by Pace Technologies. After vibratory polishing the samples were washed with soapy water, rinsed with water, rinsed with ethanol and cleaned with ultrasound while submersed in ethanol for 10 minutes.

Electron backscatter diffraction (EBSD) mapping was conducted at a FEI G FIB/SEM dual beam system equipped with an EDAX phosphorus EBSD specialized camera. A beam of 20kV and 13nA was used on the specimens tilted 70° towards the EBSD phosphorus screen, with 14mm of working distance. Various scan sizes were used, the step size varied from 0.2µm for scans 100µmX100µm to 0.4µm for scans twice as large. Hexagonal pattern was used for the map collection. All EBSD scans were collected at this equipment.

Post-processing of the collected EBSD maps started with clean-up routines. Grain dilation and Confidence Index (CI) standardization routines were performed in that order. A minimum grain size of 3pixels was conditioned, a minimum of 5degree GB misorientation and 0.1 as minimum confidence index. Regeneration of PAGS maps is explained in section 5.7.2.

5.7.6 Hot Deformation Techniques

Hot compression and hot torsion were done at a Gleeble 3500-317 at USS research facilities in Homestead, PA. All compression and torsion specimens were solution-treated at 1200°C and quenched before their deformations. The specimens were encapsulated in vacuum quartz tubes before the solution treatment was carried out. The capsules were broken at quenching. Specimens for hot compression were 15mmX15mmX20mm prisms. Specimens for hot torsion basic geometry is shown in Figure 5.6.

The cooling media for quenching was water, projected by internal nozzles at the Gleeble system. The controlled cooling of the torsion tests was done using N_2 gas blown at the outer diameter and through a hole drilled axially inside the specimen. The size of the hole was 3/16" inches.

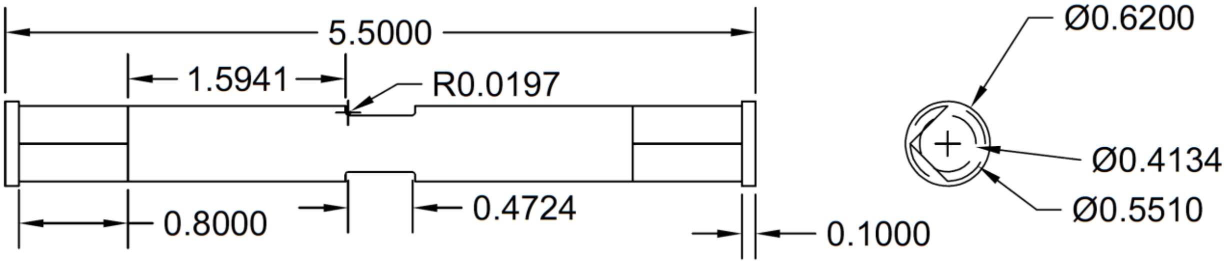

Figure 5.6 Hot torsion specimen geometry as produced by USS research team. Measurements are in inches.

5.7.7 TEM Sample Preparation

Thin foil specimens were prepared by first grinding and polishing a bulk sample. After polishing. The mountings were then broken, and the polished surface glued to a flat mounting.

Grinding was performed on the opposite side of the polished face. A controlled rate and appropriate sequence of grinding papers was chosen to get to 80-100 micrometers in thickness with a 1200 grit grinding paper. Once this thickness was reached, the foils were detached dissolving the glue in acetone.

Once thin foils were obtained, 3mm discs were punched from them in the areas of interest. The discs were then further ground in a Fischione Model 200 Dimpling Grinder to obtain either flat specimens or dimpled specimens with thickness ranging from 30-10 micrometers. Finally, electro-polishing thinning was done on the discs using a Struers-TenuPol-5 electropolishing machine. A 5% perchloric acid on ethanol solution was used as electrolyte at temperatures between -25°C to -15°C and voltages ranging from 18 to 30V.

After electropolishing, some samples required plasma cleaning or further thinning through ion beam TEM mill. Model 1070 NanoClean by Fischione was used for plasma-cleaning TEM specimens. Argon was used as gas and the specimens were cleaned while mounted on TEM holders. TEM ion milling was performed at a Model 1050 TEM Mill by Fischione. 5.5kV Ar ion beams tilted 4 to 5 degrees above and below the specimen were used while the specimen rotated continuously on its plane. Magnetization of some specimens was used as a measure to improve imaging as suggested by literature[103].

5.7.8 Carbon Replica Extractions

Carbon replica extractions were done for precipitate quantification. The first step consisted of grinding, polishing, vibro-polishing and etching the specimens using 3% nital for 20s. Secondly, the specimens were masked with transparent tape to leave exposed only the areas of interest. After masking, carbon vapor deposition of a 12nm film at 10^{-5} mBar was done at approximately 3x10-5 mBar. The equipment used for C deposition was a Leica EM ACE600 coater. After coating, floating of the C film was done by submersion of the specimens in 10% nital. The film was then fished and placed in distilled de-ionized water with 5% ethanol for cleaning and stretching before the final fishing. Carbon replica extraction technique allowed to extract not only topographical features but particles themselves[40, 104].

5.7.9 Transmission Electron Microscopy (TEM).

All TEM observation was performed on a JEOL JEM-2100F equipped with Oxford EDS detector and double-tilt holder. The analysis was done using 200kV, spot size 1 and alpha 3. Bright field micrographs were taken at eucentric height, with slight underfocus and using a high contrast aperture. Stigmation corrections were done at both the condenser and the objective lenses. High-resolution TEM was done at the thinnest locations of the samples next to the hole produced by electropolishing.

Post-processing and analysis of TEM micrographies and diffraction patterns was done using the free software Image J. Particle measurements at magnifications above 20 000X were done using the built-in particle analysis tool of the software. Less numerous measurements were traced manually.

6.0 Experimental Results

6.1 Austenitic Grain Coarsening Study Results

Calculations and experimental measurements of Prior-Austenite Grain Size (PAGS) and precipitate dissolution derived in the selection of 1200°C as the best austenitization temperature. This temperature demonstrated to provide in alloy L, both a homogeneous PAGS and dissolution of most alloying elements.

6.1.1 Thermodynamic Calculations of Dissolution

The first step to decide on a proper austenitization temperature was based on the calculated temperature of dissolution of the possible precipitates in the studied alloys. Dissolution temperatures and volume fractions of the possible precipitates in the studied systems were calculated assuming thermodynamic equilibrium and using known empirical solubility products. Based on these calculations it was decided to test the austenitization temperature above 1100°C. At these temperatures the Nb was expected to be homogeneously dissolved so it could later provide uniform non-recrystallization conditions. Experimental results proved otherwise, these are discussed in sections 6.1.2 and 6.1.3. The calculations were done considering two conditions: with and without mutual solubility of (Ti,Nb,V)(C,N).

Let us consider first the simple (insoluble) precipitates: TiN, TiC, NbN, NbN, AlN, VN, VC, and MoC; whose empirical solubility products are available in the literature. The solubility product denotes equilibrium concentrations of the alloying elements at a given temperature. For instance, the concentrations of M and N in equilibrium with the precipitate M_mN_n are given by:

$$[\boldsymbol{M}]^{\boldsymbol{m}}[\boldsymbol{N}]^{\boldsymbol{n}} = \boldsymbol{K} \tag{6-1}$$

$[\boldsymbol{M}]$ and $[\boldsymbol{N}]$ are mole fractions of **M** and **N** in solution and **K** is the solubility product[105]. The solubility product changes with temperature, allowing for dissolution at higher temperatures.

$$\boldsymbol{K} = \boldsymbol{K_o} \boldsymbol{exp}\frac{-\boldsymbol{\Delta H}}{\boldsymbol{RT}} \tag{6-2}$$

Where **ΔH** represents the precipitate's enthalpy of formation in the matrix and $\mathbf{K_o}$ is a constant. Empirical adaptations use weight percentages instead of molar fractions of the solutes, and express the solubility product as:

$$\boldsymbol{log\ Ks} = \boldsymbol{A} - \frac{\boldsymbol{B}}{\boldsymbol{T}} \tag{6-3}$$

Where **T** is the temperature of the alloy and the constants **A** and **B** are experimentally determined. These values were collected for the involved precipitates in an austenitic matrix and, combined with mass balance equations, a multiple equation system was produced. Then, these equations were solved in order of precipitate stability as expected from Gibbs free energy of formation. The preferable nitride, for instance, is TiN, the remaining N combine to form AlN, NbN and VN in that preferential order. Similarly, for carbides, the preferential order for carbon is TiC, NbC, VC, and MoC. This way, the system of equations was solved for the mass fraction of every element that is in precipitate form at temperature intervals of 10°C from 200°C to 1500°C.

Table 6.1 Solubility products utilized, and their sources.

K_s	$\log K_s = A - B/T$		Reference
	A	B	
$[Nb][C]$	3.42	7900	Gladman[10]
$[Nb][N]$	2.8	8500	Gladman[10]
$[Ti][C]$	5.33	10475	Gladman[10]
$[Ti][N]$	3.82	15020	Gladman[10]
$[Al][N]$	1.8	7750	Gao-Baker[64]
$[V][C]^{0.75}$	4.45	6560	Turkdogan[81, 106]
$[V][N]$	2.86	7700	Turkdogan[81, 106]
$[Mo][C]$	1.29	523	Pavlina, *et al*[107]

For instance, consider the presence of N and the possible formation of TiN, AlN, NbN and VN. Cooling from high temperatures, the first precipitate to be formed would be TiN. Hence, after all the possible TiN has been formed and equilibrium is reached, the following equations must hold true:

$$\boldsymbol{N_T = [N] + N_{TiN}} \tag{6-4}$$

$$\boldsymbol{Ti_T = [Ti] + Ti_{TiN}} \tag{6-5}$$

Where X_T, is the total mass fraction content in the bulk composition of species X, $[X]$, is the mass fraction of X that remains in solid solution and X_{TiN} is the mass fraction of the species X in the form of TiN. Now, considering the stoichiometric mass ratio of TiN and following the same nomenclature, Equation 6-4 can be re-written as:

$$\mathbf{N_T = [N] + \frac{7}{24} Ti_{TiN}} \quad \textbf{(6-6)}$$

The solid solution contents of N and Ti in equilibrium with TiN are related through the solubility product, K_{TiN}. So, substituting Ti_{TiN} from Equation 6-1 into Equation 6-6, we can write:

$$\mathbf{N_T = [N] + \frac{7}{24}\left(Ti_T + \frac{K_{TiN}}{[N]}\right)} \quad \textbf{(6-7)}$$

Now, notice that N_T and Ti_T are known fractions from our bulk composition, and K_{TiN} is known as a function of temperature from experimental reports in the literature. Hence, Equation 6-7 can be rearranged and solved for $[N]$ as a quadratic equation for every temperature.

$$\boldsymbol{[N]^2 + \left(\frac{7}{24}Ti_T - N_T\right)[N] - \frac{7}{24}\left(log(2.8) - \frac{8500}{T}\right) = 0} \quad \textbf{(6-8)}$$

Once $[N]$ is found as the solid solution concentration of nitrogen in equilibrium with TiN, the simple mass balance from Equation 6-4 helps us find $N_{TiN,}$ the amount of N in TiN. This way, the amount of TiN present at every temperature during cooling is found using the stoichiometric mass ratio.

Calculations for the mass fraction of every precipitate followed this method. Every new calculation considered new mass balance equations, accounting for the mass already precipitated in the higher temperature stable precipitates. For instance, when calculating MoC mass fraction, the mass balance equation for carbon must consider that precipitations of TiC, NbC and VC have already happened. Hence it must be written:

$$C_T = C_{TiC} + C_{NbC} + C_{VC} + C_{MoC} + [C] \tag{6-9}$$

When MoC precipitates, however, all other considered carbides are already present, so the amount of carbon present in each is known. Hence, the only unknowns in this equation are C_{MoC} and $[C]$.

Considering mutual insolubility of carbo-nitrides and based on the measured chemical composition of the lab heats, the total volume fraction, f_v, of precipitates calculated for each alloy is shown in Figure 6.1. Above 1100°C the total volume fraction of precipitates is the same for all the studied alloys. This was naturally expected, since the only remaining precipitate at these temperatures is TiN and all three alloys share the same N and Ti contents. These results would make us expect similar grain coarsening behavior above 1100°C, meaning Nb content can be reduced without grain coarsening problems.

The volume fraction (fv) of precipitates *vs* temperature plots in Figure 6.1 (d) show a maximum volume fraction of NbC of 0.00056, 0.00079 and 0.00101 for the L, M and H alloys respectively. The calculations predicted full dissolution of NbC at 1040°C, 1070°C and 1100°C for the L, M and H steels respectively. Based on these results it was decided to test austenitization temperatures above 1100°C to ensure complete dissolution of Nb.

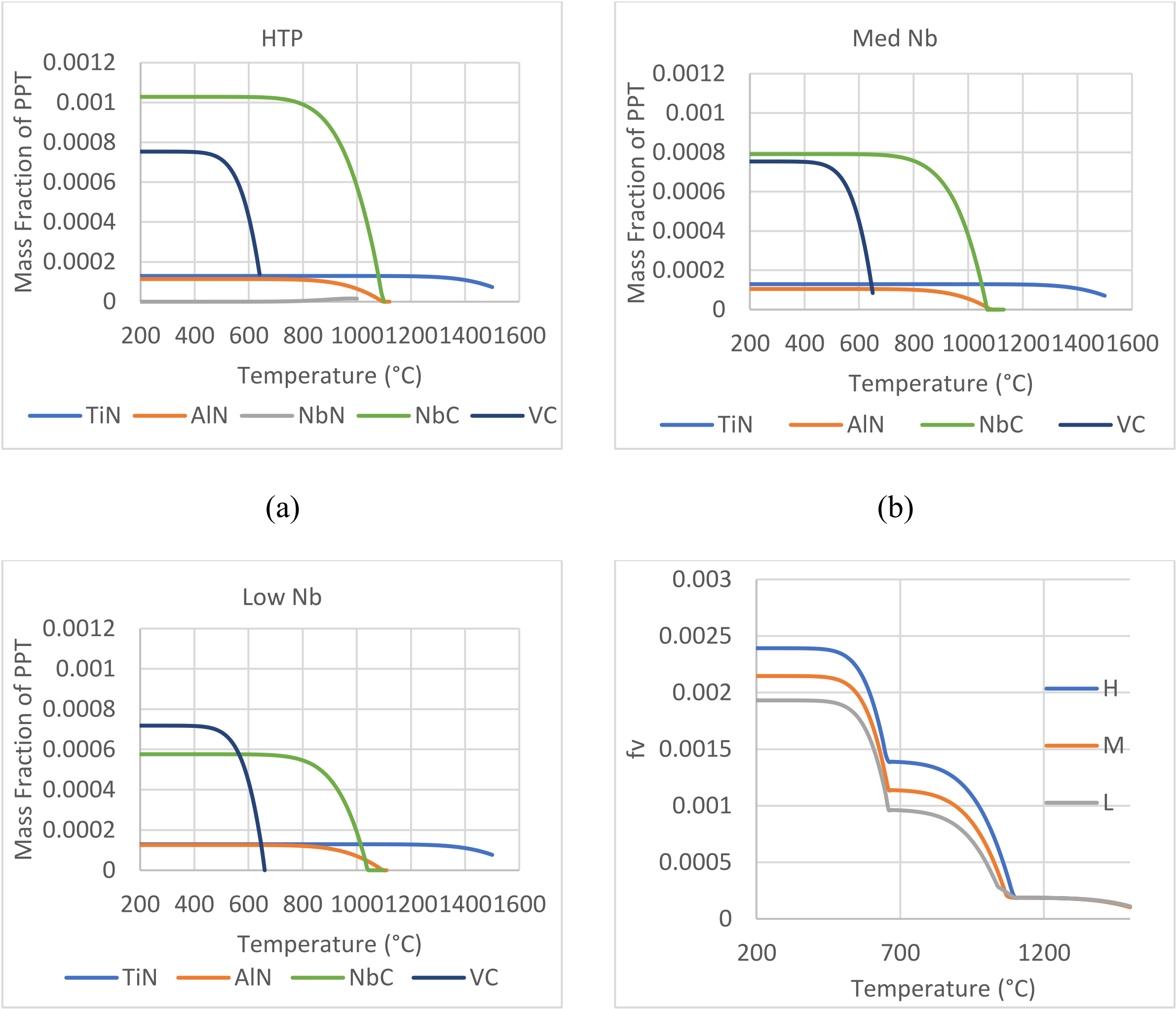

(a)

(b)

(c)

(d)

Figure 6.1 Predicted precipitate volume fractions without mutual solubility: (a) HTP or High-Nb steel; (b) Medium-Nb steel; (c) Low-Nb steel; (d) Total calculated volume fraction, fv, of precipitates.

The second type of calculations done considered the mutual solubility of Ti, Nb and V carbo-nitrides. Solubility product models that consider the complexity of precipitates mutual solubility have been proposed elsewhere[108-110]. We used a simplified system of equations, inspired by Xu, *et al*[111]. A system of 21 equations was reduced to 8 equations and 8 unknowns. The eight main equations came from 2 equations of activity of the precipitates, and 6 equations of mass balance of C, N, Ti, Nb, V and Al. These 8 equations were fed with the other 13 equations, relating solubility products of 7 precipitates (AlN, TiC, TiN, NbC, NbN, VC and VN) and activities of the 6 involved components.

The first two main equations state assumptions of activities equal to 1, for a stable precipitate in the matrix. The mutual solubility of TiC, TiN, NbC, NbN, VC and VN is considered, so the combined activity of this complex precipitate is 1, whereas AlN is insoluble, so its activity remains 1:

$$\boldsymbol{a_{TiC} + a_{TiN} + a_{NbC} + a_{NbN} + a_{VC} + a_{VN} = 1} \tag{6-10}$$

$$\boldsymbol{a_{AlN=1}} \tag{6-11}$$

Mass balance provided the other 6 main equations. For every element, the amount present in every phase must add up to the total bulk content of that component, M_T. Hence, the molar fractions, X, of three phases were considered: the matrix, the volume fraction of aluminum nitride, X_{AlN}, and the molar fraction of the mutually soluble precipitates, X_{cmplx}.

$$\boldsymbol{C_T = \left(1 - X_{cmplx} - X_{AlN}\right)[C] + (a_{TiC} + a_{NbC} + a_{VC})X_{cmplx}} \tag{6-12}$$

$$\boldsymbol{N_T = \left(1 - X_{cmplx} - X_{AlN}\right)[N] + (a_{TiN} + a_{NbN} + a_{VN})X_{cmplx} + a_{AlN}X_{AlN}} \tag{6-13}$$

$$\boldsymbol{Ti_T = \left(1 - X_{cmplx} - X_{AlN}\right)[Ti] + (a_{TiC} + a_{TiN})X_{cmplx}} \tag{6-14}$$

$$\boldsymbol{Nb_T = \left(1 - X_{cmplx} - X_{AlN}\right)[Nb] + (a_{NbC} + a_{NbN})X_{cmplx}} \tag{6-15}$$

$$\boldsymbol{V_T = \left(1 - X_{cmplx} - X_{AlN}\right)[V] + (a_{VC} + a_{VN})X_{cmplx}} \tag{6-16}$$

$$\boldsymbol{Al_T = \left(1 - X_{cmplx} - X_{AlN}\right)[Al] + a_{AlN}X_{AlN}} \tag{6-17}$$

At this point there are 14 unknowns (6 activities, 2 molar fractions and 6 concentrations) that outnumber the 8 equations, but the following equations can be considered to simplify the system. The activities of all considered nitrides and carbides can be replaced by functions of temperature and the activities of the individual elements, utilizing the solubility products, K:

$$\boldsymbol{a_{AlN} = {}^{(a_{Al}a_N)}/_{K_{AlN}}} \quad \textbf{(6-18)}$$

$$\boldsymbol{a_{TiC} = {}^{(a_{Ti}a_C)}/_{K_{TiC}}} \quad \textbf{(6-19)}$$

$$\boldsymbol{a_{TiN} = {}^{(a_{Ti}a_N)}/_{K_{TiN}}} \quad \textbf{(6-20)}$$

$$\boldsymbol{a_{NbC} = {}^{(a_{Nb}a_C)}/_{K_{NbC}}} \quad \textbf{(6-21)}$$

$$\boldsymbol{a_{NbN} = {}^{(a_{Nb}a_N)}/_{K_{NbN}}} \quad \textbf{(6-22)}$$

$$\boldsymbol{a_{VC} = {}^{(a_V a_C)}/_{K_{VC}}} \quad \textbf{(6-23)}$$

$$\boldsymbol{a_{VN} = {}^{(a_V a_N)}/_{K_{VN}}} \quad \textbf{(6-24)}$$

Therefore, the activity of every element may be replaced by the product of the activity coefficient, γ, of the element, and that element's concentration in solution $[M]$. γ can be written as a function of concentrations and Wagner interaction coefficients, e_{M1}^{M2}, of every component on a given element. These coefficients can be found in the literature:

$$a_C = [C] * \left(e_C^C * [C] + e_C^N * [N] + e_C^{Ti} * [Ti] + e_C^{Nb} * [Nb] + e_C^V * [V] + e_C^{AL} * [Al]\right) \qquad (6\text{-}25)$$

$$a_N = [N] * \left(e_N^C * [C] + e_N^N * [N] + e_N^{Ti} * [Ti] + e_N^{Nb} * [Nb] + e_N^V * [V] + e_N^{AL} * [Al]\right) \qquad (6\text{-}26)$$

$$a_{Ti} = [Ti] * \left(e_{Ti}^C * [C] + e_{Ti}^N * [N] + e_{Ti}^{Ti} * [Ti] + e_{Ti}^{Nb} * [Nb] + e_{Ti}^V * [V] + e_{Ti}^{AL} * [Al]\right) \qquad (6\text{-}27)$$

$$a_{Nb} = [Nb] * \left(e_{Nb}^C * [C] + e_{Nb}^N * [N] + e_{Nb}^{Ti} * [Ti] + e_{Nb}^{Nb} * [Nb] + e_{Nb}^V * [V] + e_{Nb}^{AL} * [Al]\right) \qquad (6\text{-}28)$$

$$a_V = [V] * \left(e_V^C * [C] + e_V^N * [N] + e_V^{Ti} * [Ti] + e_V^{Nb} * [Nb] + e_V^V * [V] + e_{\substack{v \\ V}}^{AL} * [Al]\right) \qquad (6\text{-}29)$$

$$a_{Al} = [Al] * \left(e_{Ti}^C * [C] + e_{Ti}^N * [N] + e_{Ti}^{Ti} * [Ti] + e_{Ti}^{Nb} * [Nb] + e_{Ti}^V * [V] + e_{Ti}^{AL} * [Al]\right) \qquad (6\text{-}30)$$

Substituting activities from equations 6-25 to 6-30 into equations 6-18 to 6-24, and then substituting equations 6-18 to 6-24 into equations 6-10 to 6-17; transforms equations 6-10 to 6-17 in a system of 8 equations with 8 unknowns. Furthermore, if the solid solution is regarded as dilute, due to the very small amounts of solutes; the activities of the individual components can be approximated to their concentration in solid solution. This transforms equations 6-10 to 6-17 into a much simpler system of 8 equations and 8 unknowns (6 concentrations and 2 molar fractions):

$$\frac{[Ti][C]}{K_{TiC}}+\frac{[Ti][N]}{K_{TiN}}+\frac{[Nb][C]}{K_{NbC}}+\frac{[Nb][N]}{K_{NbN}}+\frac{[V][C]}{K_{VC}}+\frac{[V][N]}{K_{VN}}=1 \qquad (6\text{-}31)$$

$$\frac{[Al][N]}{K_{AlN}}=1 \qquad (6\text{-}32)$$

$$C_T=\left(1-X_{cmplx}-X_{AlN}\right)[C]+\left(\frac{[Ti][C]}{K_{TiC}}+\frac{[Nb][C]}{K_{NbC}}+\frac{[V][C]}{K_{VC}}\right)X_{cmplx} \qquad (6\text{-}33)$$

$$N_T=\left(1-X_{cmplx}-X_{AlN}\right)[N]+\left(\frac{[Ti][N]}{K_{TiN}}+\frac{[Nb][N]}{K_{NbN}}+\frac{[V][N]}{K_{VN}}\right)X_{cmplx}+X_{AlN} \qquad (6\text{-}34)$$

$$Ti_T=\left(1-X_{cmplx}-X_{AlN}\right)[Ti]+\left(\frac{[Ti][C]}{K_{TiC}}+\frac{[Ti][N]}{K_{TiN}}\right)X_{cmplx} \qquad (6\text{-}35)$$

$$Nb_T=\left(1-X_{cmplx}-X_{AlN}\right)[Nb]+\left(\frac{[Nb][C]}{K_{NbC}}+\frac{[Nb][N]}{K_{NbN}}\right)X_{cmplx} \qquad (6\text{-}36)$$

$$V_T=\left(1-X_{cmplx}-X_{AlN}\right)[V]+\left(\frac{[V][C]}{K_{VC}}+\frac{[V][N]}{K_{VN}}\right)X_{cmplx} \qquad (6\text{-}37)$$

$$Al_T=\left(1-X_{cmplx}-X_{AlN}\right)[Al]+X_{AlN} \qquad (6\text{-}38)$$

This system has numerous sets of solutions for a given temperature. Many of these solutions include complex and negative numbers, others fail to provide concentration values between zero and the bulk content of a component. Discretion was used to choose the right solution and obtain a reliable trend. The system of equations was solved with Wolfram Mathematica® computing software.

Figure 6.2 shows the results of this calculation. The reduction of Nb to half, in the Low-Nb steel, reduces the volume fraction of complex carbo-nitrides.

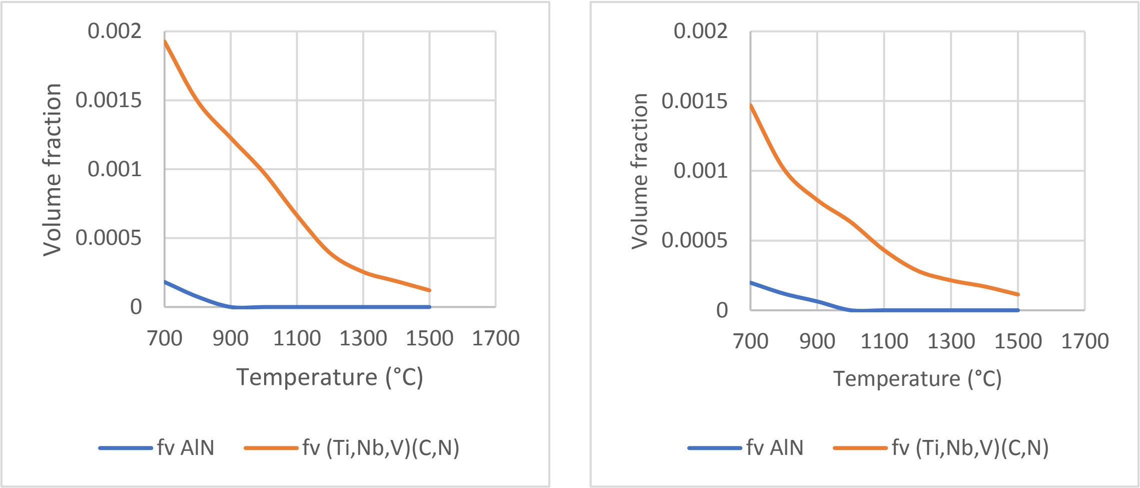

(a) (b)

Figure 6.2 Volume fractions of precipitates considering mutual solubility of Ti, Nb and V carbo-nitrides: (a) High-Nb steel; and (b) Low-Nb steel.

6.1.2 Prior Austenitic Grain Size Measurements

After austenitizing to 1150°C, 1200°C, 1225°C, 1250°C and 1300°C, PAGS were measured, results are plotted on Figure 6.3. The 95% confidence interval is shown, as calculated from a T-distribution. The effect of high Nb content on the average PAGS is minimum at 1200°C.This suggests the presence of undissolved particles.

At 1200°C soaking for 1 hour, the grain size of the Low-Nb steel is homogeneous, despite being slightly bigger than steel H. Abnormal growth starting at 1225°C for all three steels, demonstrating these Nb variations do not affect the onset of grain coarsening considerably.

In Figure 6.4 micrographs from steel L are compared for austenitizations at 1200°C and 1250°C for 1h. The inhomogeneity of the 1225°C sample contrasts with the more uniform PAGS of the 1200°C sample, signaling abnormal growth.

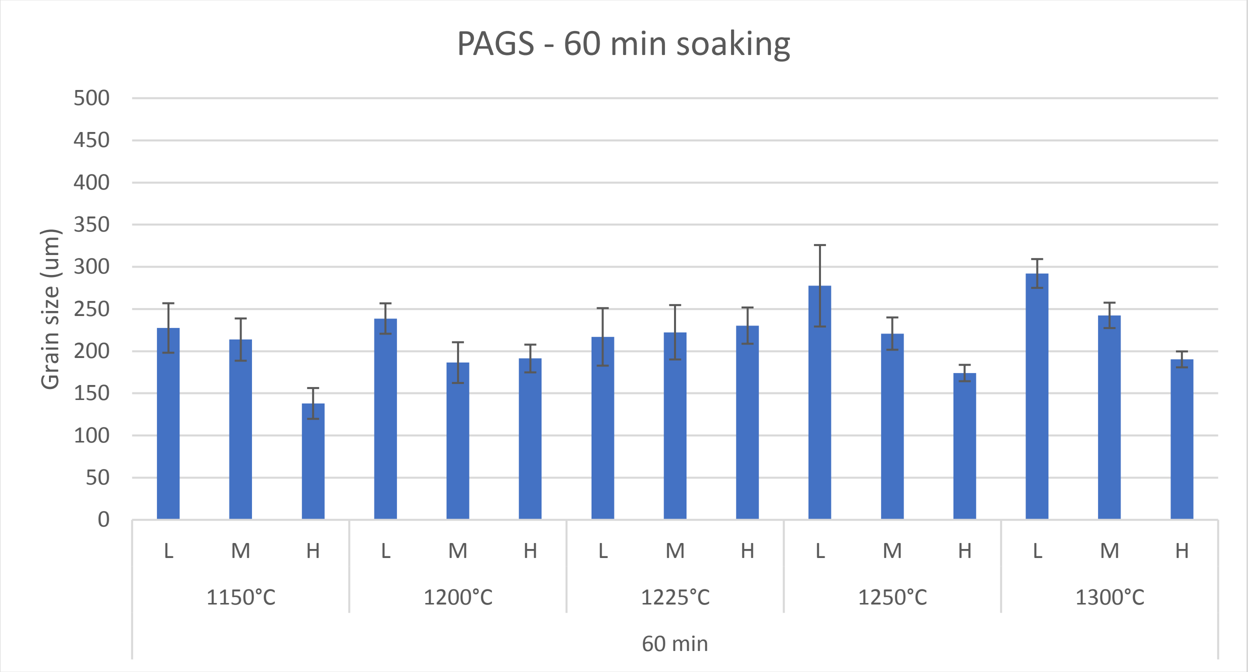

Figure 6.3. Averaged prior austenite grain diameter of austenitization for 60 min. 95% confidence interval shown. L stands for low, M for medium and H for high Nb content.

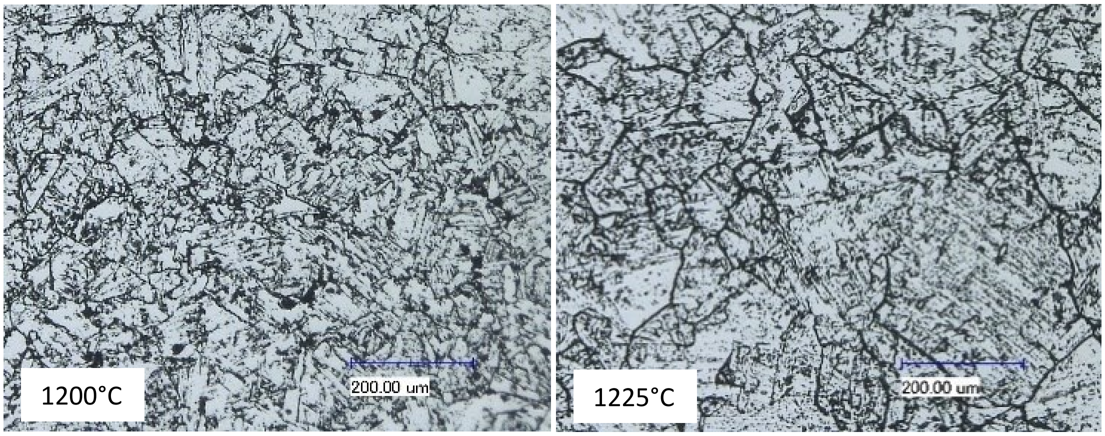

Figure 6.4 Alloy L austenitized for 1h and quenched, etched with picric aqueous solution. Abnormal grain growth can be noticed at 1225°C.

Zener model for precipitate-limited grain size was utilized to predict a PAGS. Results on Figure 6.5 show coarsening starting at 1250°C for the Low-Nb and 1300°C for the High-Nb alloy. Three other models by Gladman-Hillert[57], Rios[58, 59], and Nishizawa, *et al.*[56] were used, predicting one order of magnitude smaller PAGS. However, a bigger mismatch is there if the measured precipite volume fraction is used for estimating the PAGS. The estimation is too little compared to experimental results, these models need further reviewing for the present alloys.

Reconstructed austenite EBSD-OIM maps were utilized as a third method of grain size verification. EBSD maps were produced from the austenitized-quenched specimens. The maps were post-processed using MTEX to re-construct PAGS, utilizing the method proposed by Nyyssönen, *et al*[99]. A good match between the traditional method and the reconstructed EBSD map can be observed in Figure 6.6. The results agree with the chemically-etched based measurements. Figure 6.7 and Figure 6.8 illustrate a comparison of the chemical and the electronic methods.

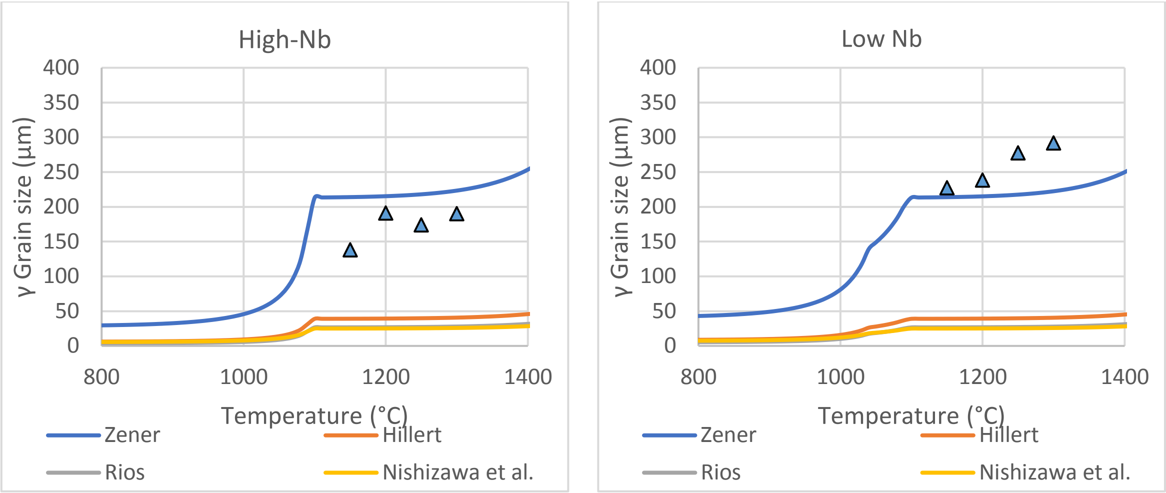

(a) (b)

Figure 6.5. Experimentally determined PAGS compared to calculated predictions.

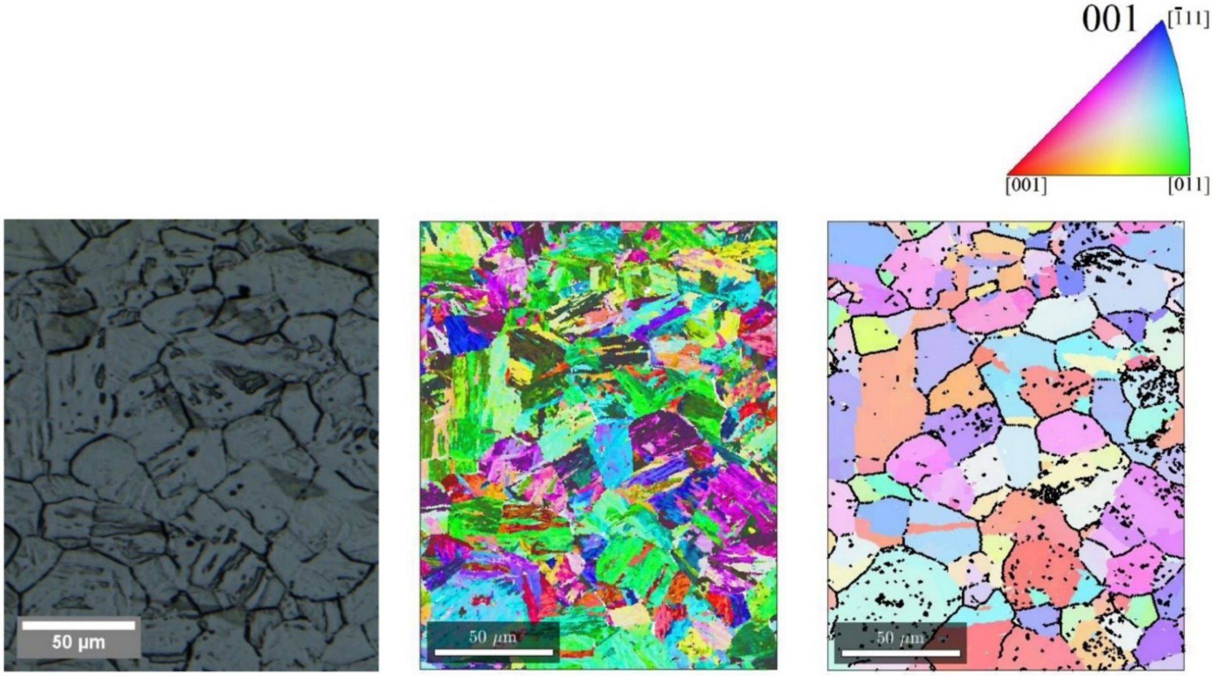

(a) (b) (c)

Figure 6.6. EBSD-OIM from (a) High-Nb steel austenitized to 1150°C for 1h and quenched; (b) its corresponding reconstructed austenite EBSD-OIM; (c) the calculated deviation of the reconstruction process.

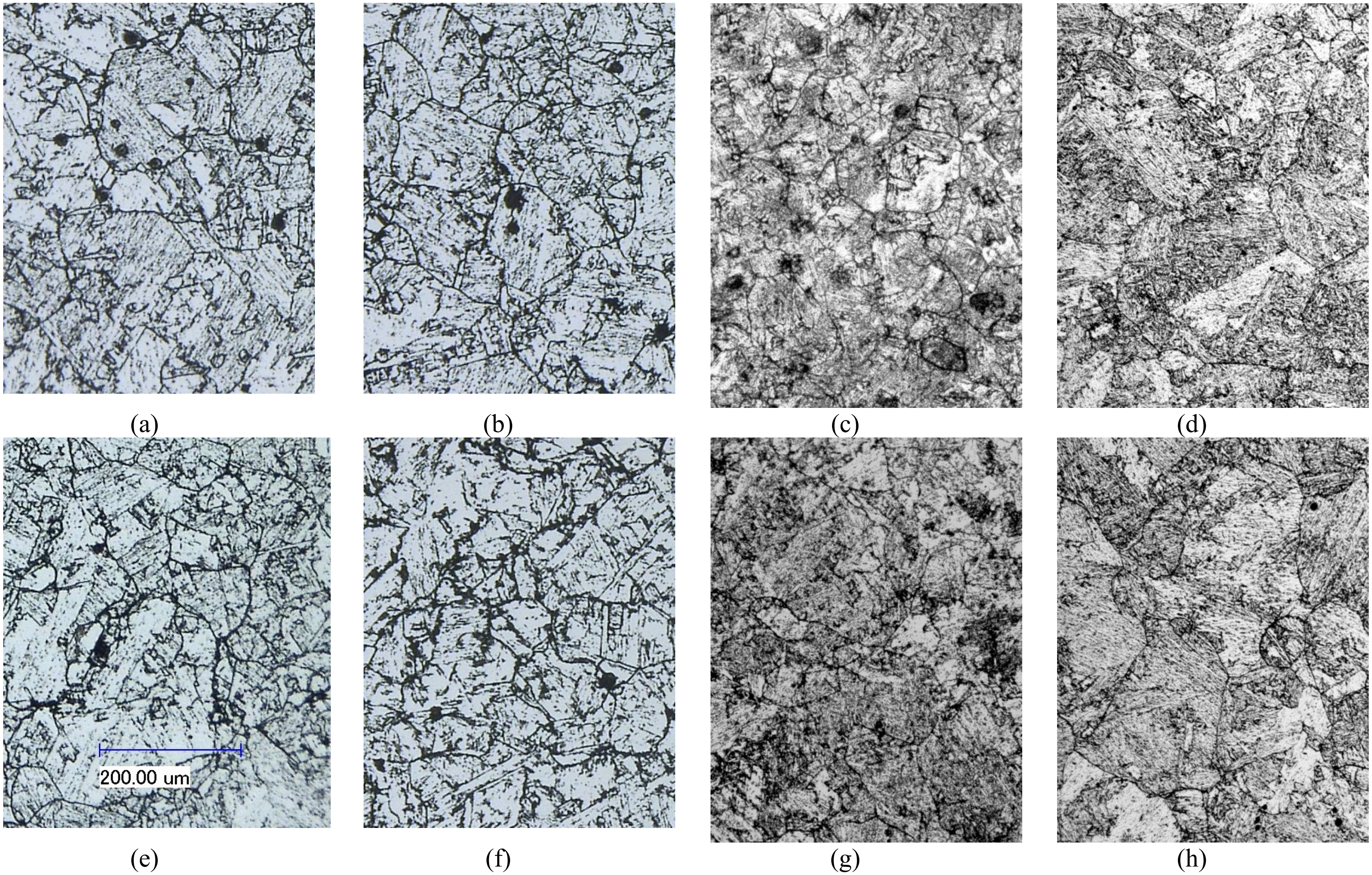

Figure 6.7 PAGS from 1h austenitizations High-Nb: (a) 1150°C, (b) 1200°C, (c) 1250°C and (d) 1300°C and Low-Nb: (e) 1150°C, (f) 1200°C, (g) 1250°C and (h) 1300°C. All images are 440X560μm, obtained after picral etching.

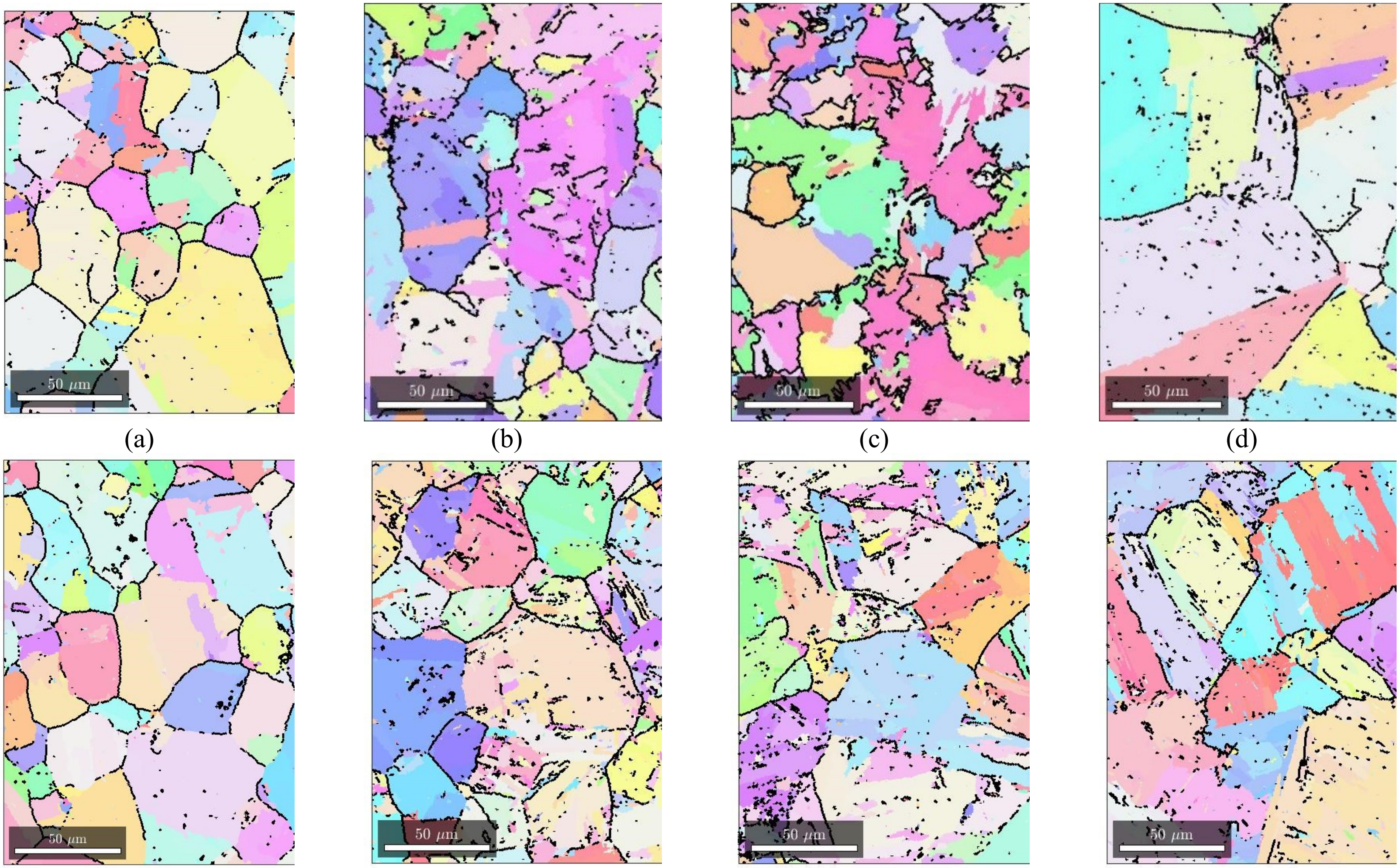

(a) (b) (c) (d)

(e) (f) (g) (h)

Figure 6.8 Reconstructed EBSD maps of austenite from austenitized and quenched specimens. High-Nb 1h at: (a) 1150°C, (b) 1200°C, (c) 1250°C and (d) 1300°C. Low-Nb 1h at: (e) 1150°C, (f) 1200°C, (g) 1250°C and (h) 1300°C. All images are 150 X 190 um.

Prior austenite grain size EBSD maps reconstruction allowed for GB misorientation analysis. GB misorientation maps are shown in Figure 6.9. As a general trend, low angle GBs from approximately 25° to 45° are abundant at low temperatures of austenization. They gradually reduce in fraction as the austenitization temperature increases, whereas GBs with misorientations higher than 50° increase as the grains coarsen at higher austenitization temperatures.

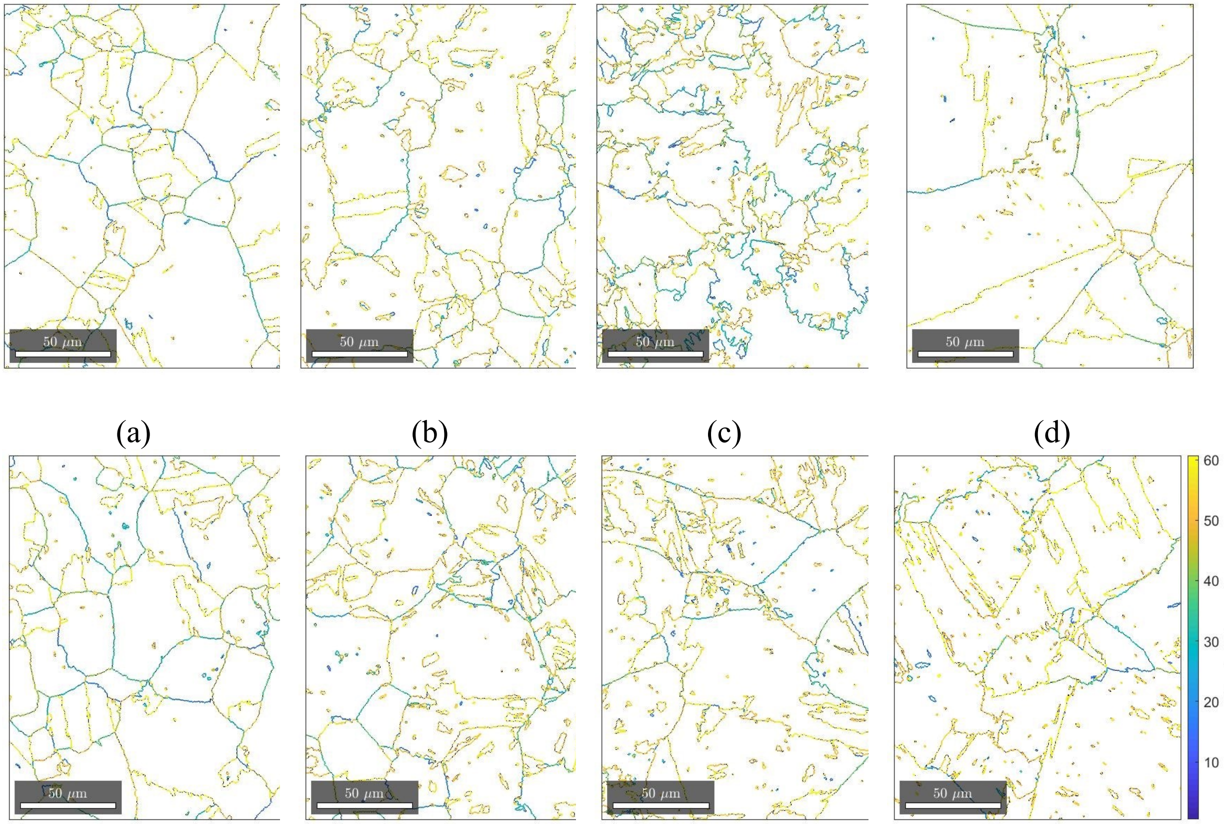

(a) (b) (c) (d)

(e) (f) (g) (h)

Figure 6.9 Prior austenite GB misorientation maps of High-Nb specimens austenitized for 1h at: (a) 1150°C, (b) 1200°C, (c) 1250°C and (d) 1300°C; and of Low-Nb alloy austenitized to (e) 1150°C, (b) 1200°C, (c) 1250°C and (d) 1300°C.

This behavior is more evident at the histograms of GB misorientation Figures Figure 6.10Figure 6.11. In Figure 6.10 the peak of GB misorientation above 50° is clearly increasing with austenitization temperature. Whereas boundaries between 20° and 45°h misorientation decrease, suggesting higher mobility of these GBs.

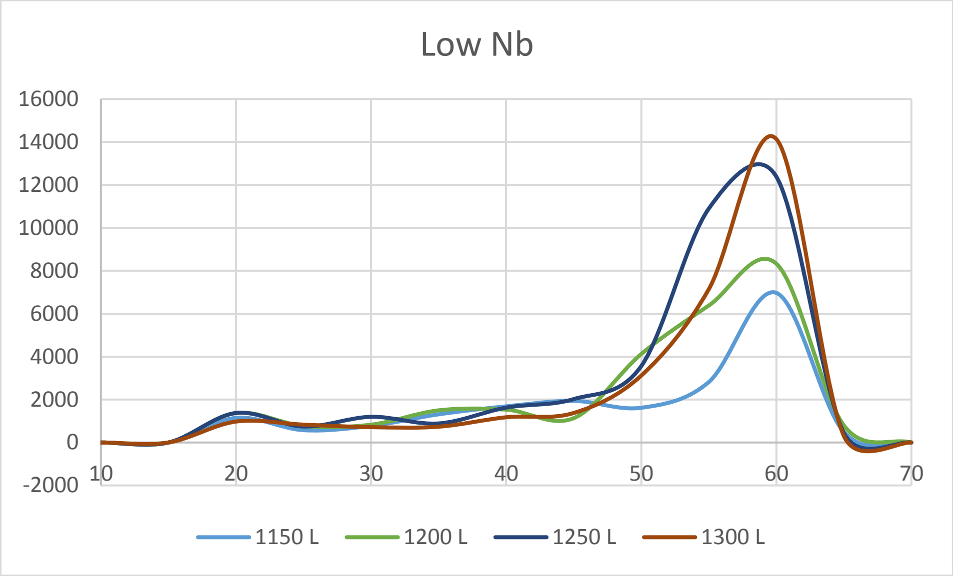

Figure 6.10 Austenite GB misorientation histogram from austenitization of Low-Nb steel at different temperatures for 1h. Obtained from reconstructed austenite maps.

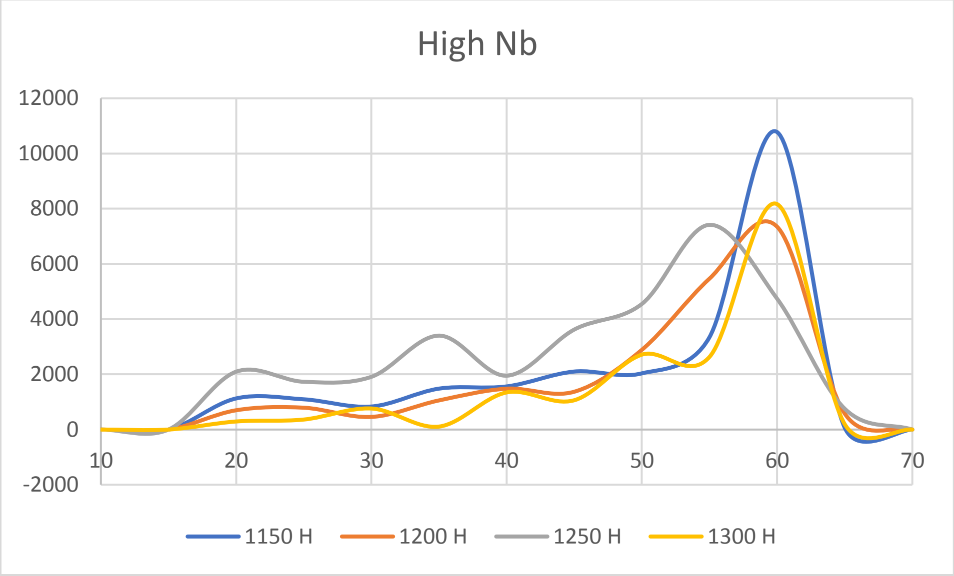

Figure 6.11 Austenite GB misorientation histogram from austenitization of High-Nb steel at different temperatures for 1h. Obtained from reconstructed austenite maps.

Similar GB misorientation observations have been associated with faster PPT coarsening and have been considered crucial to the onset of grain coarsening [86, 112-115].

The GB character has been observed to influence the way PPTs coarsen and consequently their effectiveness at pinning GBs in diverse alloying systems[86, 114-117]. One example comes from aluminum with alumina particles. In a study by Tweed, *et al*. [118], alumina particles pinned low-angle GBs better than they did high-angle GBs. In the former case, the pinning was even stronger than what the Zener relation predicted. This example suggests that GB character distribution affects grain growth.

A second example comes from electric steels, where the frequency of GB with misorientations between 20° and 45° decreases with increasing austenization holding time. Simultaneously, GB with misorientations less than 15° and higher than 50° increase in frequency[113, 114]. These observations suggest a higher mobility of the boundaries in the former group. Similar examples are found elsewhere[86, 115, 117]. A general observation from these studies is that the high mobility of GBs with 20°-50° misorientation facilitates grain coarsening. Results from Low-Nb steel agree with these observations.

6.1.3 Precipitates Measurements

Experimental evidence suggests the dissolution of particles containing Nb was not complete in any of the tested austenitization conditions. Tested temperatures were 1150°C, 1200°C, 1250°C and 1300°C with 1 hour soaking time. NbC dissolves at 1096°C according to calculations based on solubility products in section 6.1.1. The presence of NbC and Nb-Ti complex carbonitrides was assessed by SEM and TEM on the reheated samples. Incomplete dissolution of Nb has a positive effect in austenite grain size control, this supports the possibility of using Low-Nb alloy.

Precipitation size measurements were done using SEM and TEM micrographs. TEM's higher resolution allowed the observation of small-sized abundant precipitates. Micrographs were taken from random locations to ensure a representative sample. Based on the TEM micrographs, measurements of the precipitates' volume fraction and size were obtained.

The results of the dissolution study by TEM are plotted on Figure 6.12. 95% confidence intervals are shown in error-bars. The enlarged confidence index at samples austenitized to 1300°C is the result of Ostwald ripening and the presence of very few particles in the explored area. The explored area, however, was representative, especially for measuring particles in samples austenitized below 1300°C. As expected, the volume fraction decreases as austenitization temperature increases. Average particle size, on the other hand, increased with austenitization temperature.

The stability of Nb-rich precipitates was higher than expected at temperatures above 1100°C. The average diameter of observed particles is very similar for both alloys up to 1250°C, then it increases dramatically at 1300°C amid a volume fraction reduction. The dissolution of small particles and Ostwald ripening of the big particles are the responsible phenomena for this average size increase.

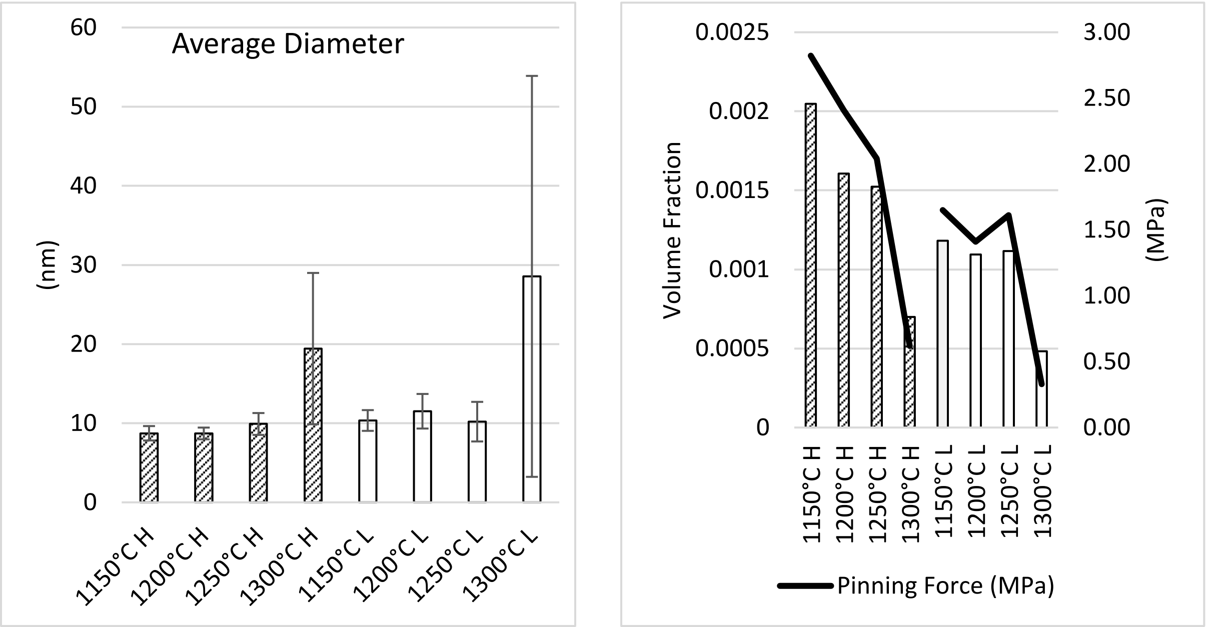

(a) (b)

Figure 6.12. (a) Average particle diameters at the different austenitization temperatures with soaking time of 1h; (b) corresponding volume fraction of precipitates and pinning force.

The pinning force associated to the particles was calculated using Zener's model as expanded by Gladman for flexible boundaries[119].

$$\boldsymbol{F_{PIN} = 4r\sigma N_s} \tag{6-39}$$

Where, r, is the mean average particle radius, σ, is the interfacial energy particle/austenite per unit area and Ns, is the number of particles per unit area, that for a flexible boundary is given by[62]:

$$\boldsymbol{N_s = \frac{3f_v^{2/3}}{4\pi r^2}} \tag{6-40}$$

Where f_v, is the volume fraction of particles and, r, the mean particle radius. Pinning force calculations showed a trend dominated by volume fraction. The pinning force was high at austenitizing temperatures below 1250°C for both alloys. In the Low-Nb steel, the pinning force was only 21% below the High-Nb alloy. This allowed for both alloys to have homogeneous and very similar grain size at 1250°C.

Size distribution of precipitates, shown in Figure 6.13, was analyzed in two categories for better visualization: precipitates smaller than 40nm, namely small precipitates and precipitates 40nm and bigger, namely big precipitates. The size distribution change with temperature evidences the simultaneous occurrence of Ostwald ripening phenomena and dissolution. Fortunately, the small particles show considerable stability at 1250°C and below in the Low-Nb steel.

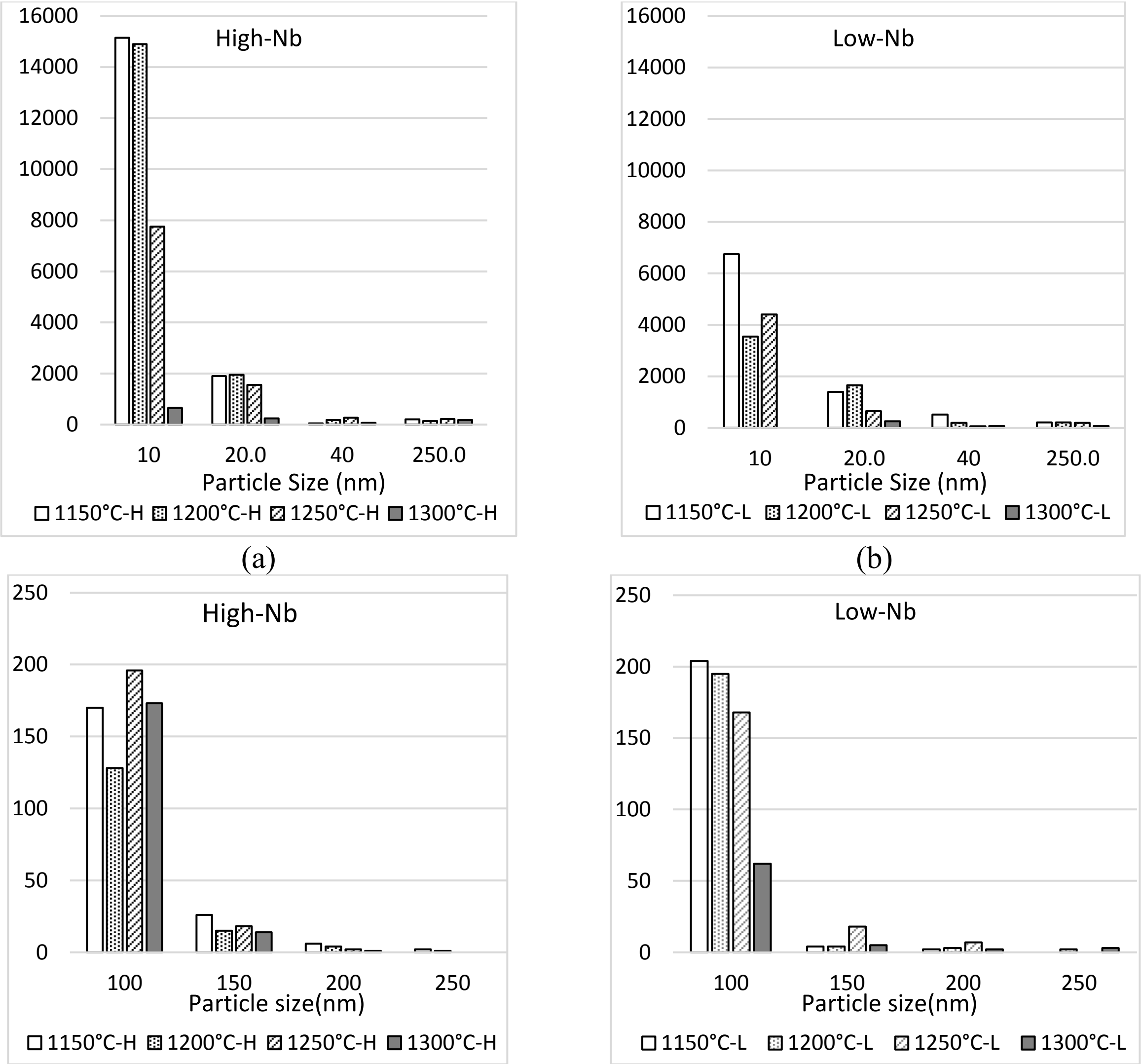

(a) (b)

(c) (d)

Figure 6.13 Distribution of particle size: (a) and (b)Particles smaller than 40nm; (c) and (d) particles bigger than 40nm.

The first observations were made on SEM at random areas, these included randomly selected grain boundaries, intergranular regions and triple boundaries. SEM showed presence of mostly complex carbides containing both Nb and Ti, with about 300 nm in size. A few Nb-only (i.e. without Ti) particles, much smaller, were observed. However, in specimens austenitized to 1250°C and 1300°C these Nb-only particles were not found using SEM.

Complex carbides were predominating at the highest temperatures, containing both Nb and Ti in the same particle. This can be due to the NbC nucleating on TiN epitaxially as reported elsewhere[94, 120-126] or due to complex particles. The coarsened particles were complex (Nb,Ti)(C,N) with various compositions. Particle coarsening by Ostwald ripening is well-known to occur at temperatures where there is high solute diffusivity and the particles are stable. Many of these particles were single-phase solid solution complex precipitates, whereas others showed diverse epitaxial morphologies.

The carbides were identified by TEM analysis, confirming their complexity. Dark Field (DF), Bright Field (BF), EDS and Selected Area Diffraction Pattern (SADP) were used. In Figure 6.14 a NbC particle precipitated at the TiN habit plane is shown. SADP is consistent with TiN (004) interplanar spacing. SADP shows plane (101) from NbC is parallel to (002) from the Fe (α') matrix. This is evidence of coherence between the two particles. EDS detected Ti and Nb. V was also detected, it is undeterminable by this technique whether V is in the matrix, or at the particles.

Coherency was found by HRTEM in big complex particles, an example is presented in Figure 6.15. At the matrix/particle interface, the fringes are continuous. The Fast Fourier Transform (FFT), shown to the right of the micrograph shows parallelism between planes [2 0 2] from the carbide, and plane [2 0 0] from the matrix.

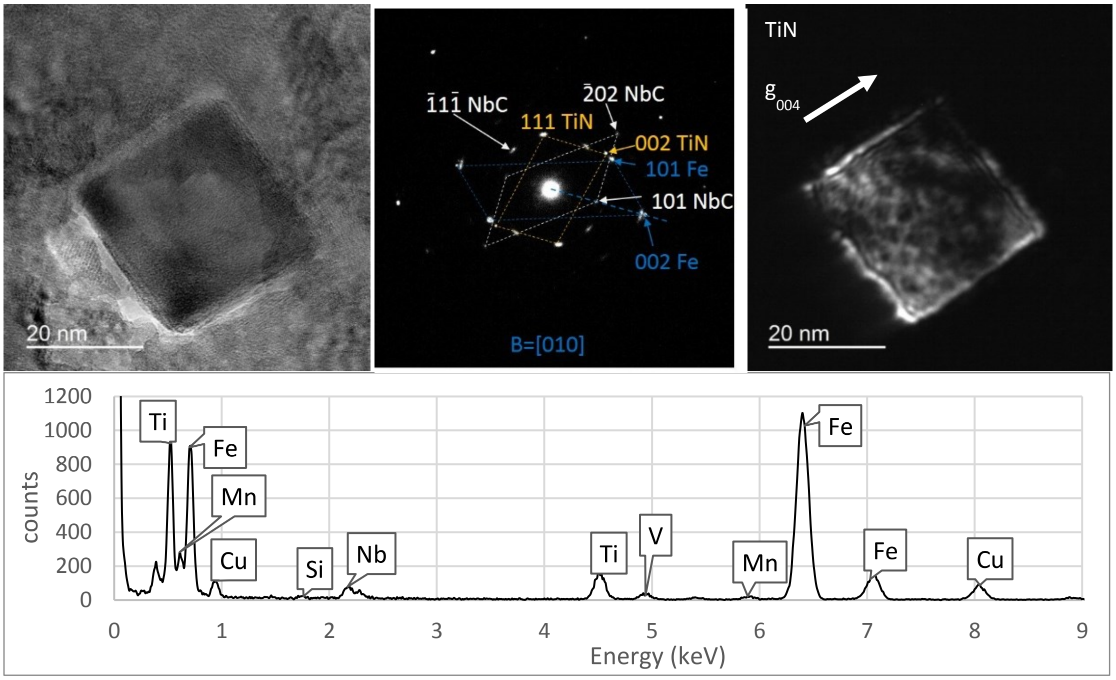

Figure 6.14 BF-DF, SADP and EDS of a precipitate found in Low-Nb steel. 1200°C 1h.

Nb-rich particles were a common finding among the particles bigger than 50nm. NbC grew on pre-existing TiN forming the early stages of cruciform complex precipitates. This kind of precipitate nucleation has been reported in previous research works[94, 125, 126] as being formed during the solidification process. In the present study, the reheating conditions are not enough to completely dissolve these complex particles. These particles have reportedly been effective at GB pinning and recrystallization inhibition[69].

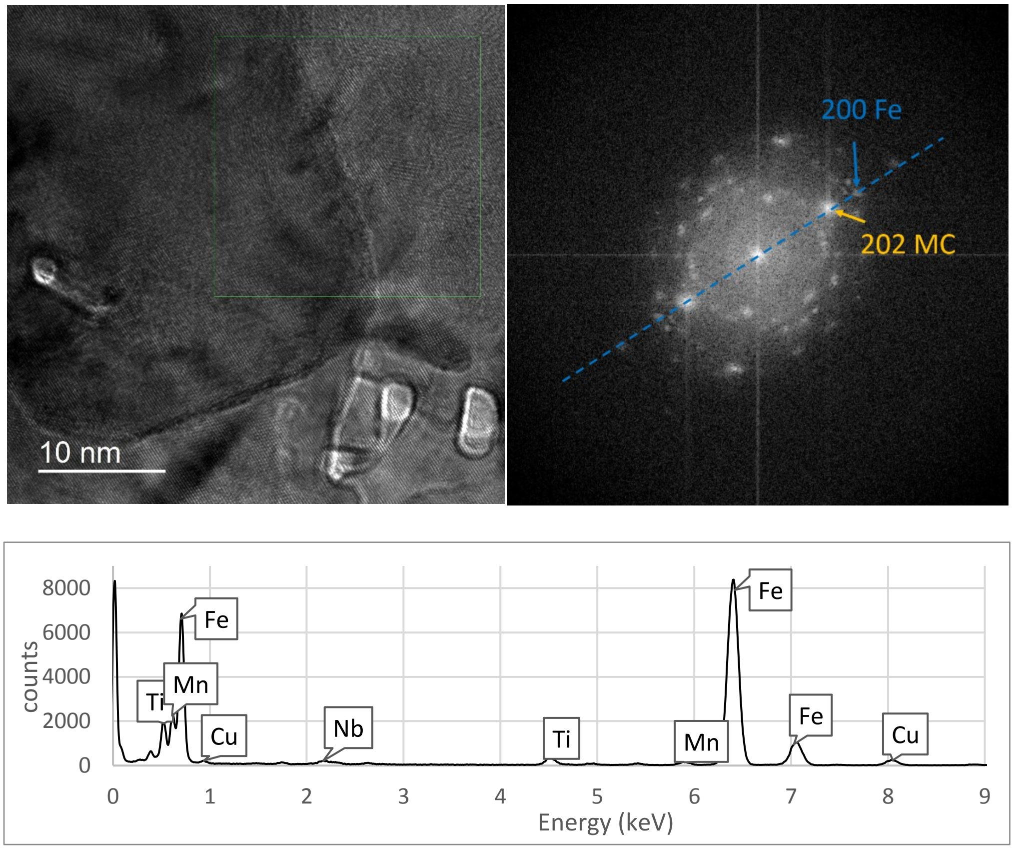

EDS	Si	Ti	Mn	Fe	Cu	Nb
at% / wt%	0.74 / 0.4	3.21 / 2.8	1.38 / 1.4	91.1 / 91.1	2.83 / 3.2	0.73 / 1.2

Figure 6.15. HRTEM, FFT and EDS of a precipitate in Low-Nb steel, 1200°C 1h.

Precipitates on Figure 6.16 are examples of the complex precipitates found in both alloys within the 1150°C to 1300°C austenitization temperature range. Figure 6.16 (a) is a particle found in Low-Nb steel austenitized to 1300°C for 1h. Diffraction shows the [0 1 0] zone axis from where the beam [4 0 2] was used to produce the corresponding DF image. This DF shows only half of the particle, evidencing the bicrystalline nature of the particle. The precipitate on Figure 6.16 (b) is an example of the presence of these complex precipitates at low austenitization temperatures. It was found in High-Nb steel austenitized to 1150°C for 1h. Again, the DF reveals the bicrystalline nature of this particle.

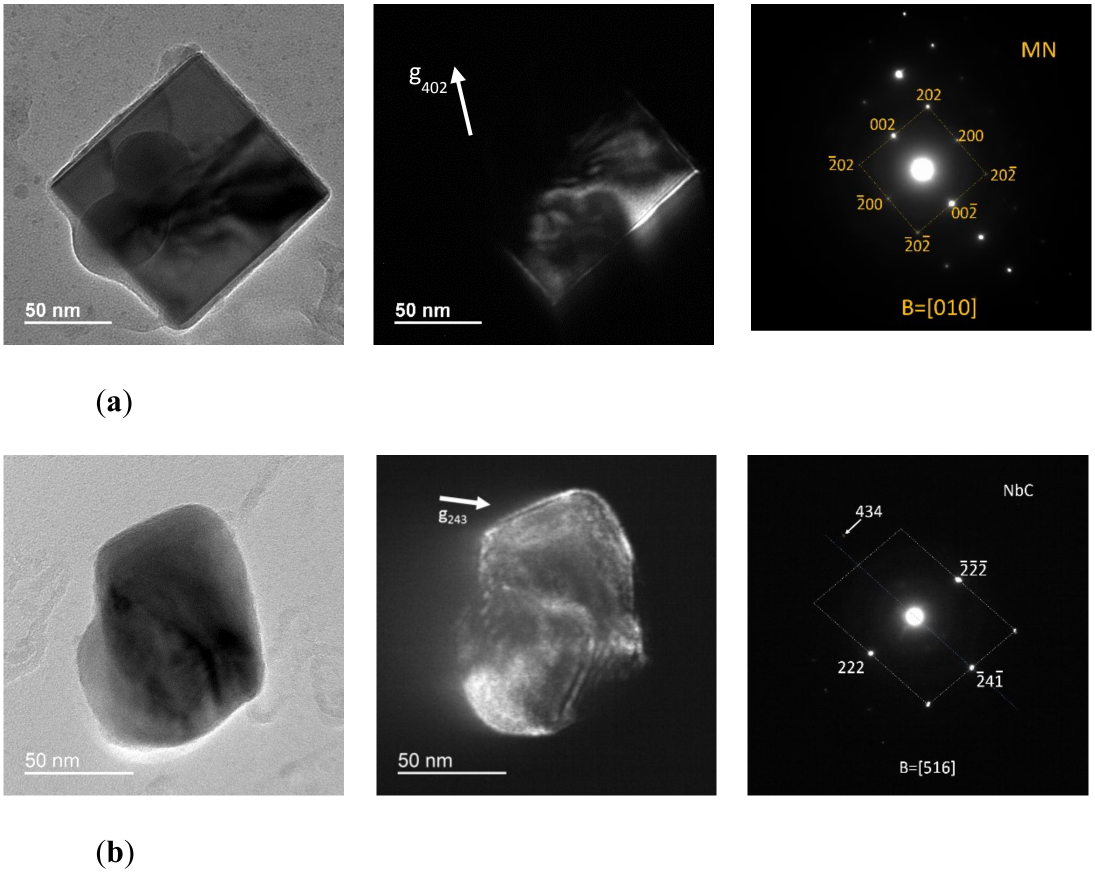

Figure 6.16 BF, DF and SADP of complex particles: (a) Low-Nb steel 1300°C for 1h; (b) High-Nb steel 1150°C for 1h.

Dissolution of precipitates was first calculated using thermodynamic equilibrium conditions. Later, experimental measurements were done. The measured precipitation behavior did not follow the thermodynamic predictions, the experimental volume fractions of Nb-bearing particles exceeded the calculated ones. This evidence suggests that reheating was not done under equilibrium conditions. Despite incomplete dissolution of all alloying elements, 1200°C continues to be the best reheating temperature, for inhomogeneous PAGS cannot be afforded.

Comparing calculated to experimentally measured precipitate volume fraction, a shift in the dissolution behavior is observed, see Figure 6.17. Experimentally measured volume fraction is higher than equilibrium conditions. After 1h of soaking at temperatures above 1100°C, complete dissolution of NbC was theoretically expected. Evidently, those equilibrium conditions are not reached, so dissolution is delayed. At these temperatures Nb was found in complex particles containing both Nb and Ti, either in mutual solid solution or in epitaxially grown particles.

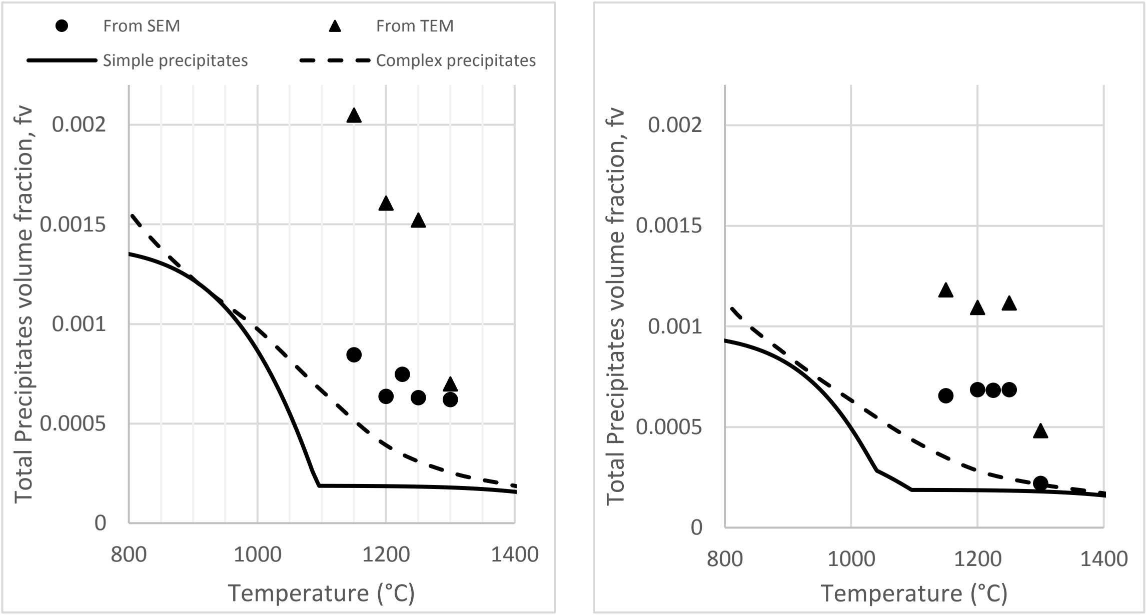

(a) **(b)**

Figure 6.17 Experimental volume fraction of precipitates, compared to the calculated expectations: (a) High-Nb steel; (b) Low-Nb steel.

The particles' morphology and complexity may explain the higher experimental volume fraction of precipitates, as compared to the calculated one. Two phenomena can be directly associated to the difficult dissolution of epitaxially grown precipitates: the reduction of matrix/particle surface area, and the low energy of particle/particle interfaces. Both phenomena hurdle the dissolution process. TEM evidence clearly shows complex carbonitrides that may be retarding dissolution. The unexpected resistance to austenitic grain coarsening of the Low-Nb steel can be understood as a consequence of complex carbide formation.

6.2 Deformation and Recrystallization Results

6.2.1 Experimental Hot Properties of Studied Alloys

The deformation and recrystallization behavior of the three alloys was analyzed from plain-strain hot compression experiments at a Gleeble machine. A set of deformation steps of 20% reduction each, with interpass times of 20s was performed on each allow at different temperature range to experimentally determine the temperature below which full recrystallization is not achieved (Tnr). The Mean Flow Stress (MFS) was experimentally determined. Tnr showed sensibility to Nb content, as expected, whereas MFS was insensitive to it.

The experimental range of temperature for these tests was based on Tnr predictions by empirical equations (See Table 6.2). Equations by Boratto, Bai and Fletcher[127] are among the most accurate in predicting Tnr[81]. However, Boratto equation is based on chemical composition only, disregarding strain, and even fails to consider N content, a strong precipitate former. Bai developed an equation in 2011 including N content as an important factor but disregarding strain. Bai also developed a model for Tnr considering the effect of strain, the well-known driving force for recrystallization. This model was modified by Fletcher to produce an empirical equation combining chemical and strain effects. All equations acknowledge the remarkable influence of Nb content on Tnr.

Table 6.2 Empirical models for prediction of Tnr [81].

$T_{nr} = 887 + 464C + \left(6445Nb - 644\sqrt{Nb}\right) + \left(732V - 230\sqrt{V}\right) + 890Ti + 363Al - 357Si$	Boratto
$T_{nr} = \beta e^{-0.36\varepsilon}$	Bai 1993
$T_{nr} = 174log\left[Nb\left(C + \frac{12}{14}N\right)\right] + 1444$	Bai 2011
$T_{nr} = 203 - 310C - 149\sqrt{V} + 657\sqrt{Nb} + 683e^{-0.36\varepsilon}$	Fletcher

Fletcher equation was used to determine Tnr in the three steels as a function of strain. JMAT Pro software was used to determine the critical temperature Ar3. Both are plotted in Figure 6.18. Fletcher predictions helped design the experiments for determining Tnr on the three steels.

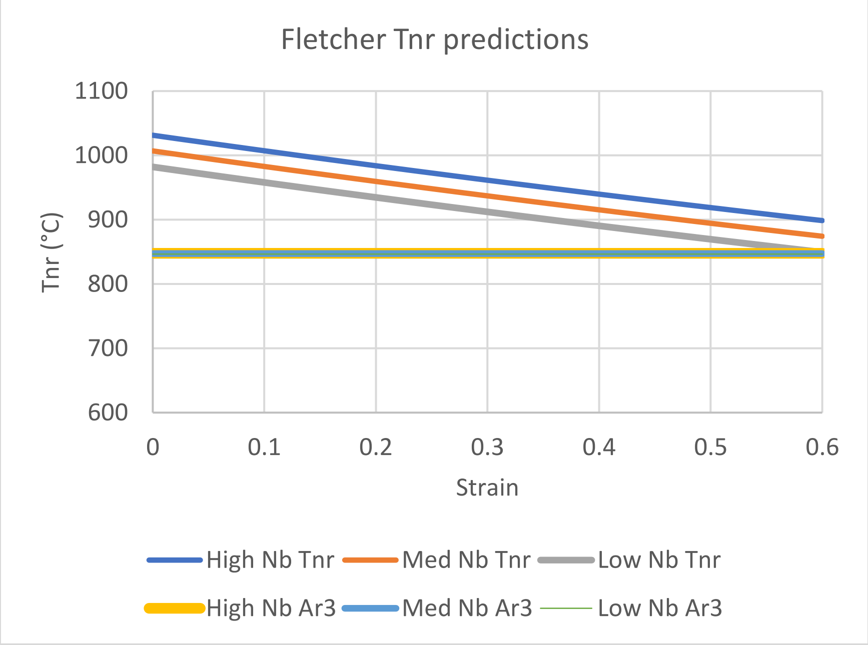

Figure 6.18 Tnr and Ar3 predictions by Fletcher equation and by JMAT Pro software respectively.

Deformation experiments consisted of repeated 20% reduction passes with 20s interpass times at temperature intervals of 50°C. A comparison between the behavior of the three steels is provided in Figure 6.19. Notice the almost continuous strain hardening of steels with high Nb at 975 and 925°C, indicating non-recrystallizing conditions. The change of strength with respect to temperature was used as indication for Tnr.

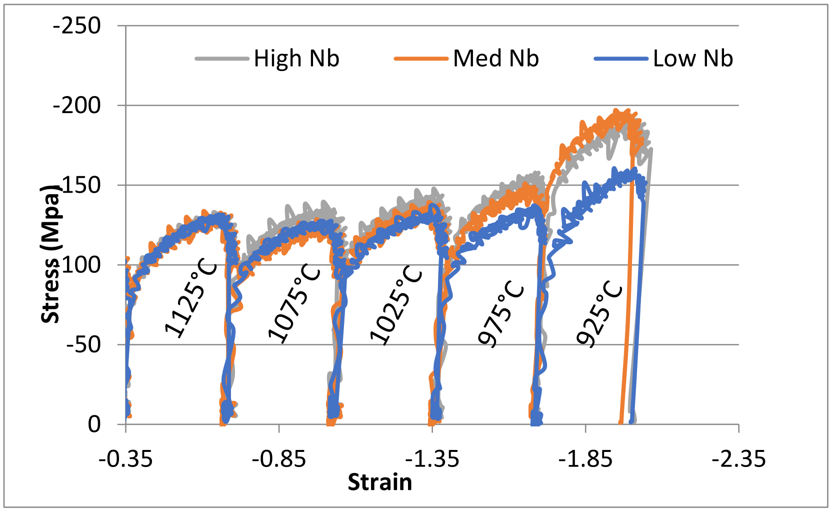

Figure 6.19 Stress-strain recordings of 5 compression heats.

Hot compression tests with more than six deformation passes were prone to failure, hence, only five passes-experiments were used for determining Tnr. In order to have a finer resolution, two sets of deformations were run for each composition with an offset of 25°C. This yield ten deformations with 25°C offsets as shown in Figure 6.20.

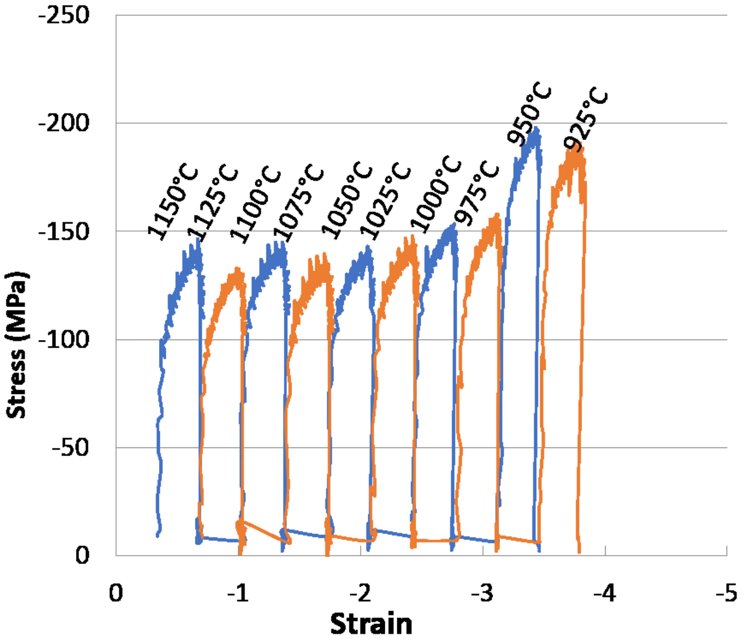

Figure 6.20 High- Nb stress-strain plot of all deformations performed for T_{NR} determination.

Strength-temperature plots from Figure 6.21 show a transition of the change of strength with temperature. The rate of change is low and uniform at high temperatures, then suddenly increases at low temperatures. This change is associated to the transition from full-recrystallization to non-recrystallization conditions[81].

Having fully recrystallized strain-free grains after every pass, means strain hardening is not accumulated. The increase of strength as temperature decreases must then only come from grain refinement and a decrease in dislocation mobility. At lower temperatures, as NbC particles start to precipitate, complete recrystallization is not achieved, and strain hardening begins to accumulate. This transition was clear for both High-Nb and Low-Nb steel. Figure 6.21 shows how the transition from recrystallization to non-recrystallization does not match the predictions by Fletcher equation, in red.

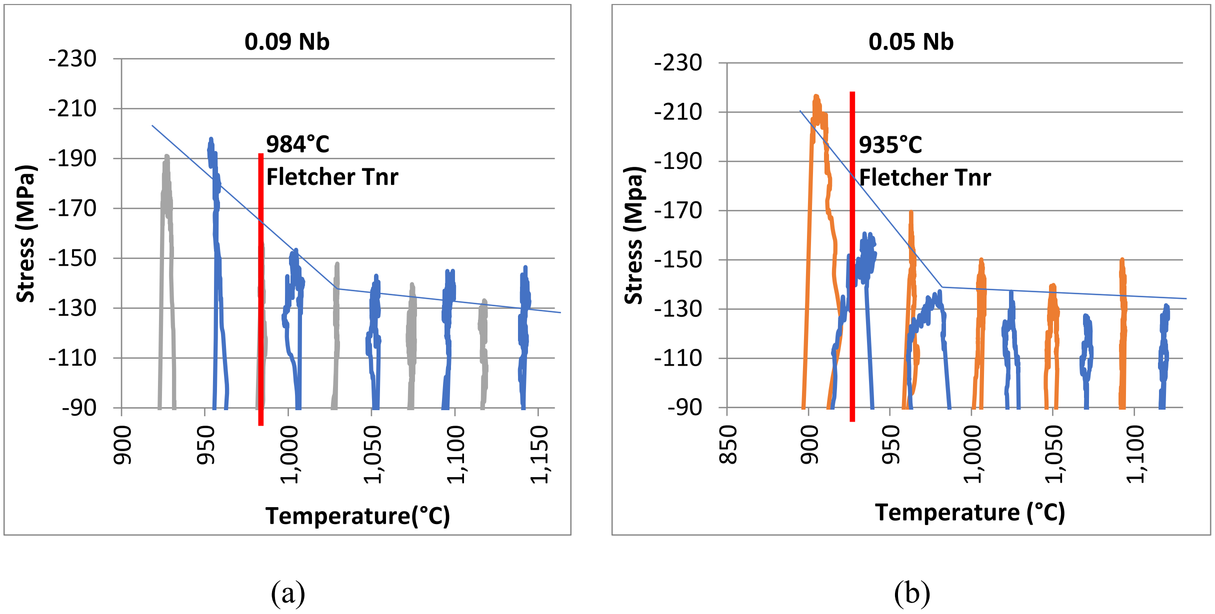

Figure 6.21 Experimental observance of T_{NR}. Experimentally determined Tnr for the two alloys of interest presented in Table 6.3. Both alloys transition temperatures differ from predictions. Recrystallization models need reviewing.

Table 6.3 Temperatures of no-recrystallization.

	Experimental Tnr	Boratto 1988	Fletcher 2008	Bai 2011
Low Nb	~975°C	1100°C	935°C	1001°C
High Nb	~1025°C	1309°C	984°C	1043°C

The experimental determination of MFS was based on thorough analysis of the flow curves (See Figure 6.22). First, the slope of the elastic zone was measured and the 0.2% offset linear function was determined. Second, the intersection from the 0.2% linear function and the experimental data was used to mark the yield stress. Third, the elastic zone area was determined using Matlab. Finally, the experimental formula could be applied.

$$\boldsymbol{MFS = \frac{1}{\varepsilon_1 - \varepsilon_0} \int_{\varepsilon_0}^{\varepsilon_1} \sigma \, d\varepsilon} \tag{6-41}$$

Where $\boldsymbol{\varepsilon_0}$ and $\boldsymbol{\varepsilon_1}$ represent strain at yield and at ultimate strength respectively, and the integral denotes the area below the elastic region curve.

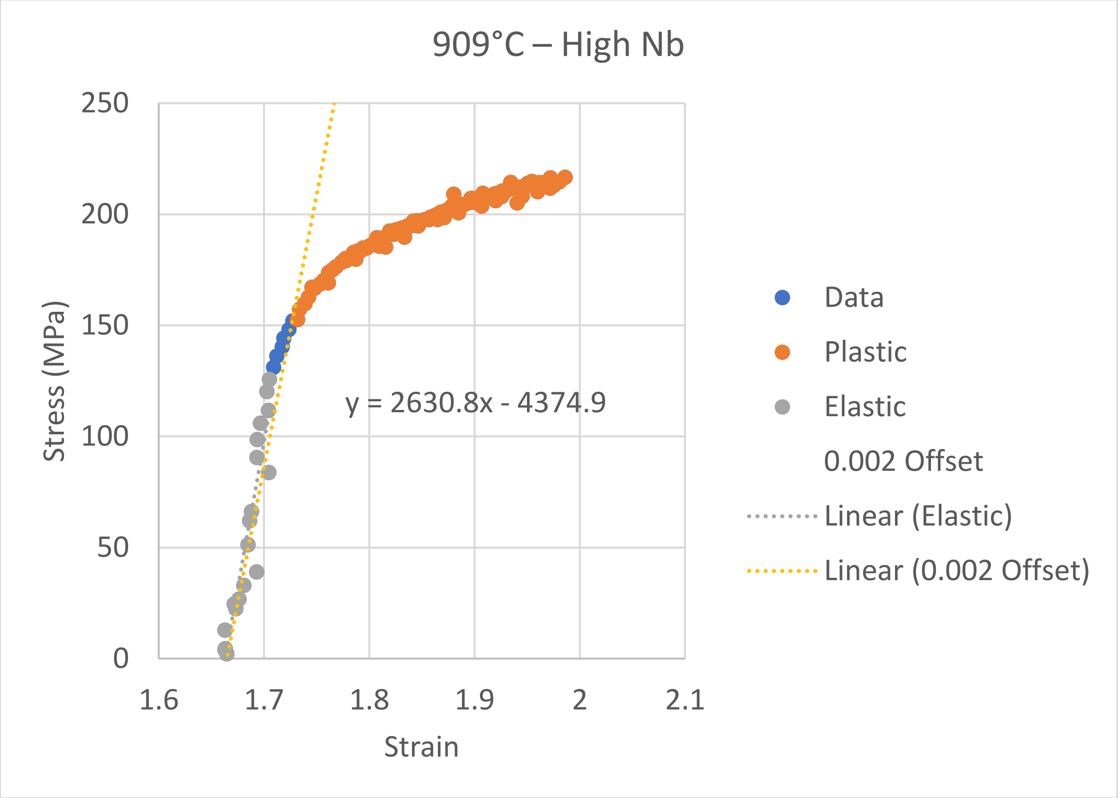

Figure 6.22 Illustration of the MFS experimental extraction procedure.

Equation 6-42 was proposed by Misaka and Yoshimoto[128] for predicting MFS as a function of strain, $\boldsymbol{\varepsilon}$, strain rate, $\dot{\boldsymbol{\varepsilon}}$, and carbon content in solid solution $[\boldsymbol{C}]$.

$$\boldsymbol{MFS = e^{\left(0.126-1.75[C]+0.594[C]^2+\frac{2851+2968[C]-1120[C]^2}{T}\right)\varepsilon^{0.21}\dot{\varepsilon}^{0.13}}} \qquad \textbf{(6-42)}$$

This equation was later improved by Siciliano, et al[68], accounting for Mn content, accumulated strain and static and dynamic recrystallization:

$$\boldsymbol{MFS = (0.78 + 0.137[Mn]) * (MFS_{Misaka}) * \left(1 - X_{dyn}\right) + K\sigma_{ss}X_{dyn}} \qquad \textbf{(6-43)}$$

Where $[Mn]$ is the manganese content in solution, σ_{ss}, is the steady state stress necessary for dynamic recrystallization, and X_{dyn} is the softening from the peak to the steady state stress.

Misaka, *et al.* and Siciliano *et al.* models were applied to the experimental conditions. A comparison between predictions and experimental measurement of MFS is presented in Figure 6.23. Experimental MFS values show a slightly different slope than predicted. It appears that there are two independent trends, one for recrystallizing conditions and another for non-recrystallizing conditions. Misaka and Siciliano models are pretty good at predicting MFS for this alloy, even though Misaka's model does not explicitly account for recrystallization effects.

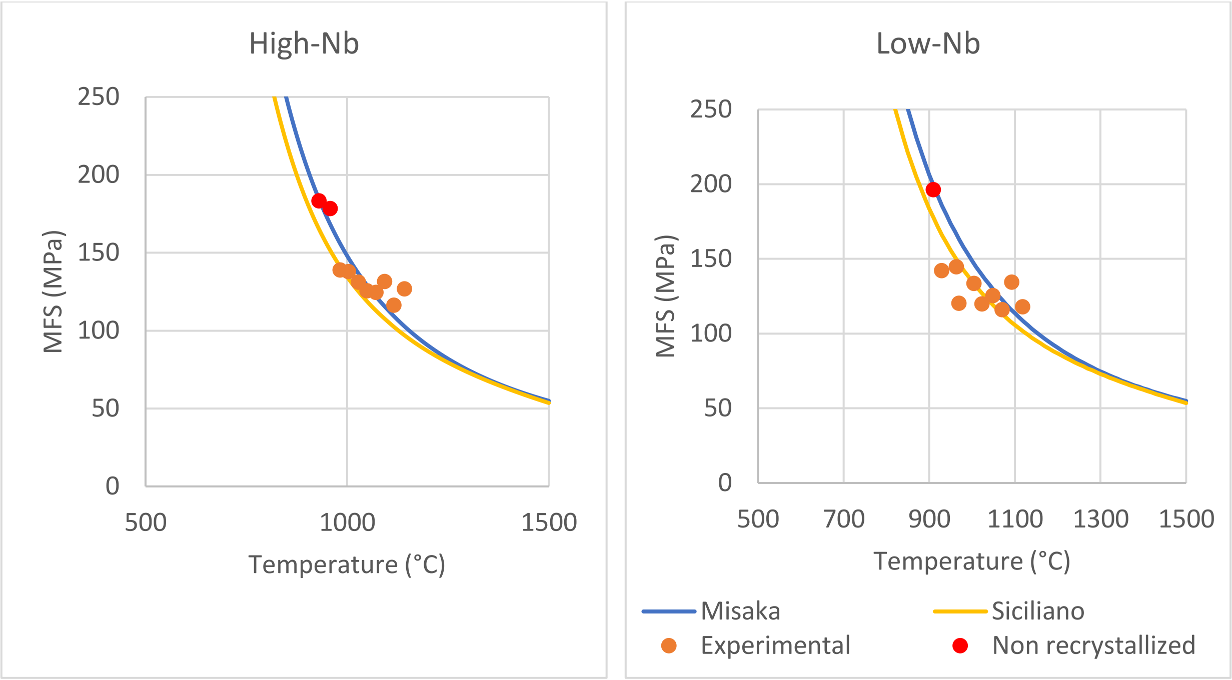

(a) (b)

Figure 6.23 Comparison of experimental MFS to Misaka, *et al* model.

The experimental MFS results show a jump when recrystallization stops happening below Tnr. Experimental data shows two linear behaviors with the change of slope at Tnr. Misaka and Siciliano models sow a rather exponential trend but manage to predict the values closely.

6.2.2 Recrystallization Control

With the purpose of determining what controls recrystallization in these steels, a set of specimens was deformed, quenched and characterized. Specimens from both alloys were repeatedly deformed and after the 975°C cooled down to 925°C in 20s and quenched. The red spot in Figure 6.24 marks the point at which these specimens were quenched. Notice that this point represents the transition to non-recrystallization for the Low-Nb steel, while the High-Nb steel has already entered said condition before the 975°C pass. Hence, the High-Nb steel should have accumulated strain, whereas Low-Nb steel should be recrystallized for the last time. Comparison of the specimens' characterization was oriented to understand the two different recrystallization-control behaviors. The question was whether recrystallization is stopped by precipitation or solute drag.

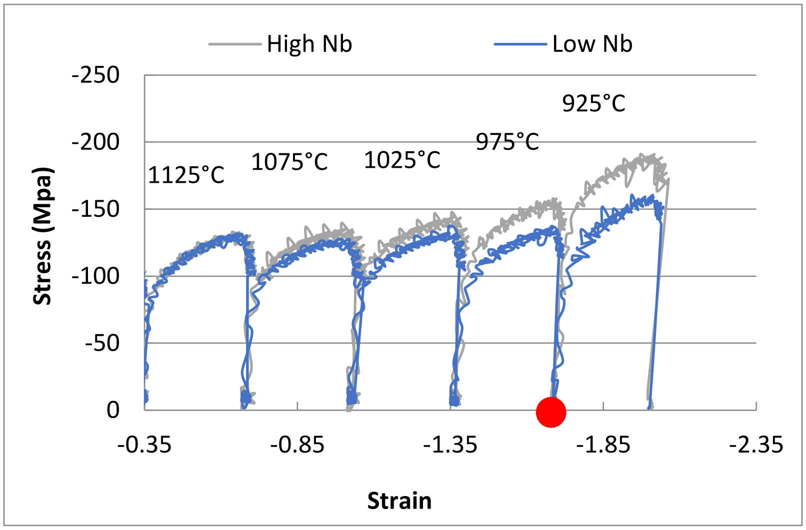

Figure 6.24 Illustration of the experiment for comparing recrystallization behavior differences. The red point represents where specimens were quenched.

The first important measurement is the precipitate analysis. The measured volume fraction was 0.0015 for the High-Nb and 0.00068 for the Low-Nb. Size distribution, in Figure 6.25, shows similar distribution of size, the average particle diameter was 76.7nm and 77.8nm for the High and Low-Nb respectively. In other words, the precipitates are the same size and distribution, and the Low-Nb steel shows half the amount the High-Nb does.

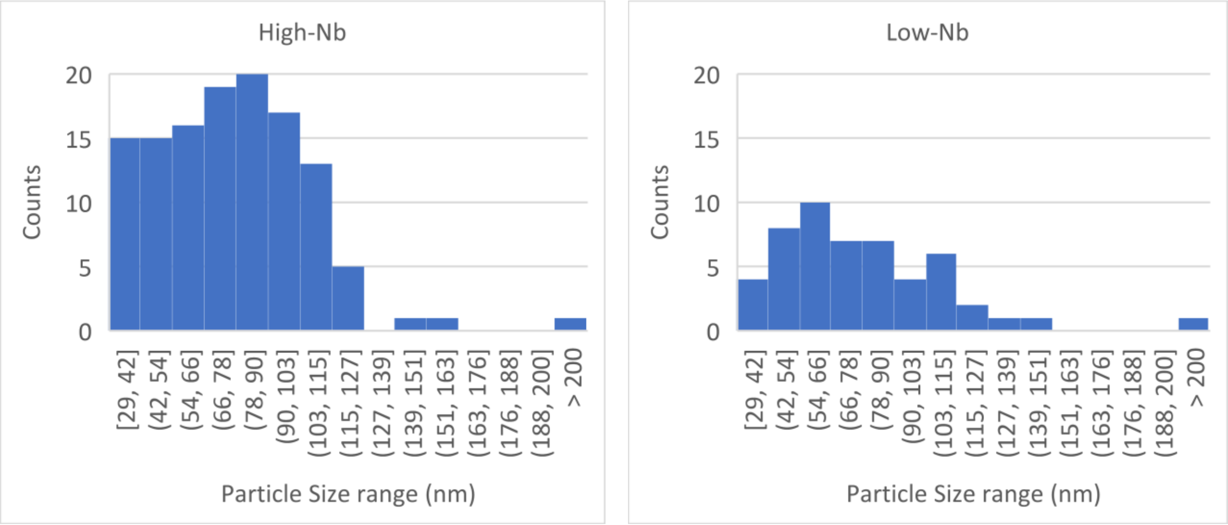

(a) (b)

Figure 6.25 Precipitate size distribution of samples deformed in 5 hits deformed and quenched 20s after 975°C hit.

Once the precipitates had been measured, the pinning force was calculated, according to Zener equation and Gladman’s flexible boundary model. Recrystallization force was calculated using the method by Palmiere, *et al*[62].

$$\boldsymbol{F_{RXN}} = \frac{\mathbf{12.5}\boldsymbol{\Delta\sigma^2}}{\boldsymbol{\mu}} \qquad \textbf{(6-44)}$$

Where $\boldsymbol{\Delta\sigma}$, is the increase from yield strength to ultimate strength, and $\boldsymbol{\mu}$, stands for the shear modulus of austenite, approximately 40 GPa. Table 6.4 shows the results of these calculations. In the case of High-Nb steel, F_{PIN} is lower than F_{RXN}, however the experimental behavior indicated non-recrystallyzation conditions were attained. This means that an additional force could be opposing GB migration.

Table 6.4 Recrystallization force vs pinning force comparison.

	F_{PIN}	F_{RXN}
High-Nb	0.0323MPa	0.525 MPa
Low-Nb	0.0141MPa	0.151 MPa

Another type of force that opposes GB movement is the solute drag force. As explained in section 3.1.3, segregation of solutes at GB's vicinity can lower the GB's energy and mobility. To verify if this phenomenon was occurring in any of the two steels, WDS Electron Probe Microanalysis (EPMA) was performed across GBs. After sixteen line-analyses where all found elements concentrations were plotted against location, only a few examples showed slight segregation of C, Nb and P. Figure 6.26 shows an example of the few segregation cases found. The concentration line of Nb shows a trend increasing towards the GB. However, the change is too abrupt, it may be related to a precipitate. The carbon concentration profile is more likely to represent segregation although this is minimal.

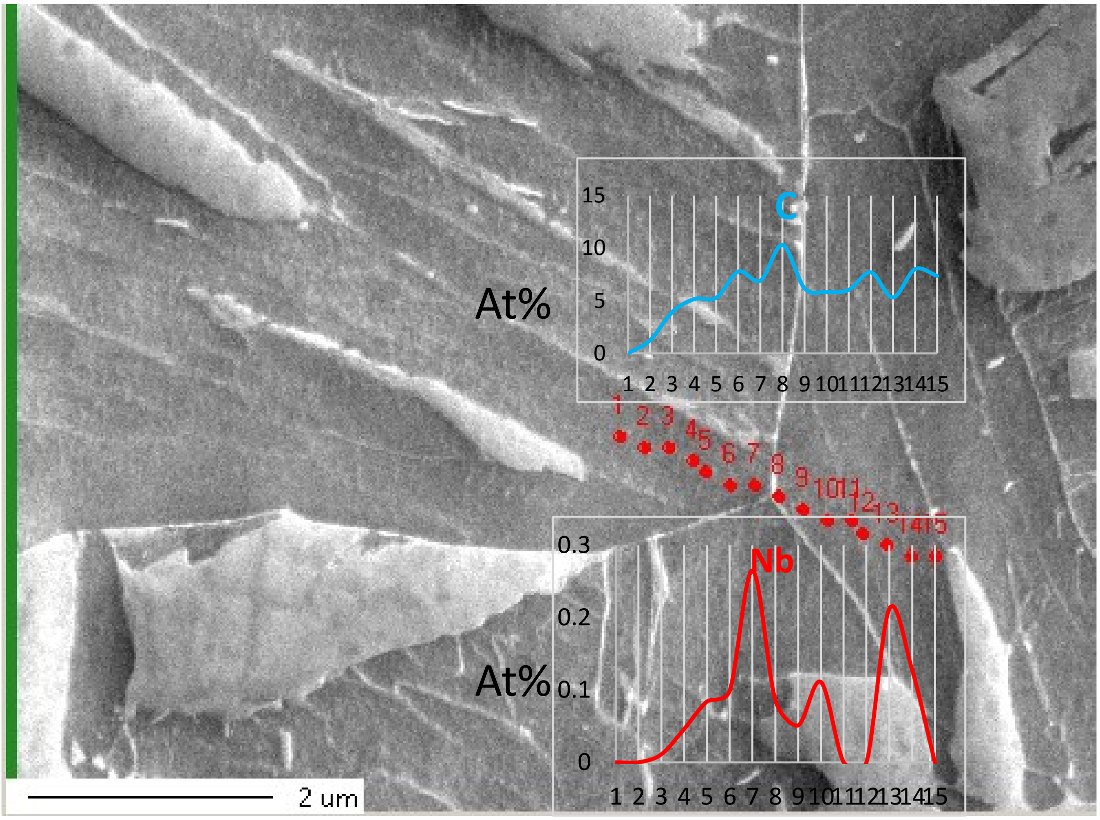

Figure 6.26 EPMA of High-Nb steel deformed to 975°C and quenched after 20s.

As a general observation, the cases of segregation were limited and precipitation abundant. It was evident that precipitates and not solutes were responsible for recrystallization control. Later experiments (reported in next section) proved that the missing force in Table 6.4 comes from more precipitates that were not resolved with SEM.

EDS analysis of the precipitates in SEM and TEM showed abundant occurrence of complex precipitates containing Nb, Ti and sometimes V. Few examples contained Nb only. Standalone NbC precipitates were considerably smaller than the complex (Ti,Nb)(C,N) particles. Figure 6.27 was obtained from the Low-Nb steel specimen, deformed repeatedly, down to 975°C, then cooled down to 925°C in 20 seconds and quenched. At experimental Tnr, the complex precipitates are big and abundant and the simple NbC are smaller and minority.

Similar is the case of High-Nb steel, although the volume fraction is bigger in this case. Figure 6.28 was obtained from the High-Nb steel quenched as deformed in non-recrystallization conditions, approximately 100°C below its Tnr. Thin foils were prepared and analyzed in TEM. The complexity of precipitates was revealed. Similar precipitates to those in reheated specimens were found, see Figure 6.29.

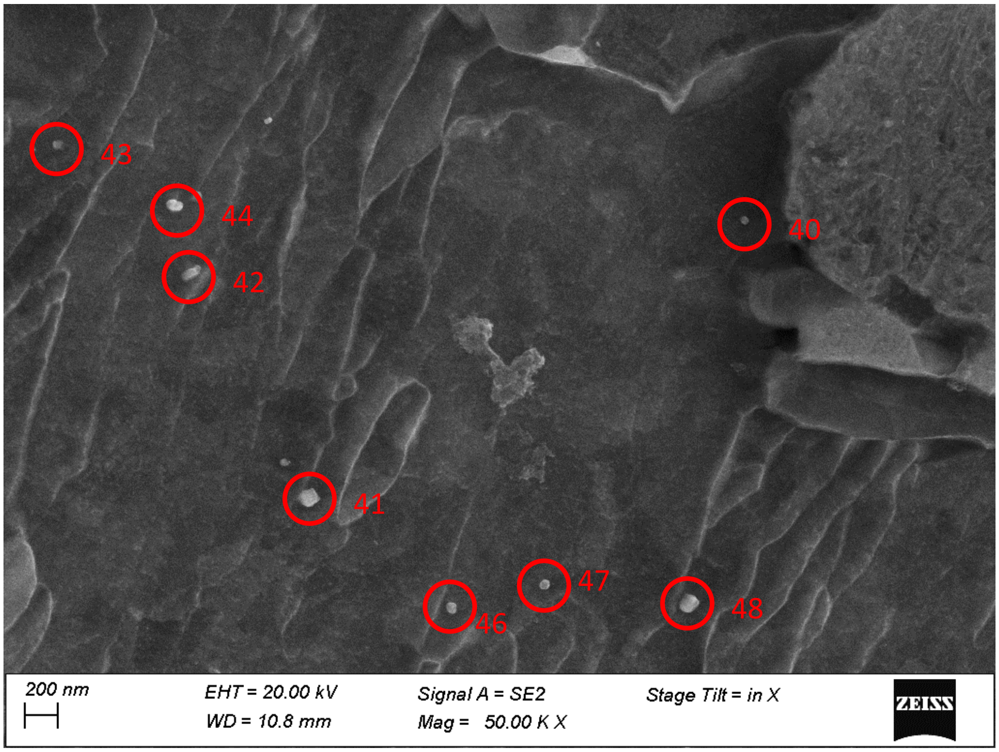

Spectrum (Wt%)	C	**N**	Si	**Ti**	**V**	Cr	Mn	Fe	**Nb**
40	10.38		0.22				1.47	86.36	**1.57**
41	10.3	**3.24**	0.29	**1.57**		0.32	1.37	81.38	**1.53**
42	10.12	**3.41**	0.31	**2**		0.36	1.29	80.87	**1.63**
43	10.94		0.33			0.27	1.57	85.89	**1**
44	11.03		0.27	**0.76**		0.26	1.52	83.62	**2.53**
46	10.1	**2.95**	0.35	**0.9**	**0.22**	0.25	1.36	82.75	**1.13**
47	11.65		0.24				1.57	83.69	**2.85**
48	10.37	**3.62**	0.31	**2.25**	**0.24**	0.28	1.22	80.06	**1.65**

Figure 6.27 SEM-EDS analysis Low-Nb steel deformed to 975°C and quenched after 20s. At Tnr.

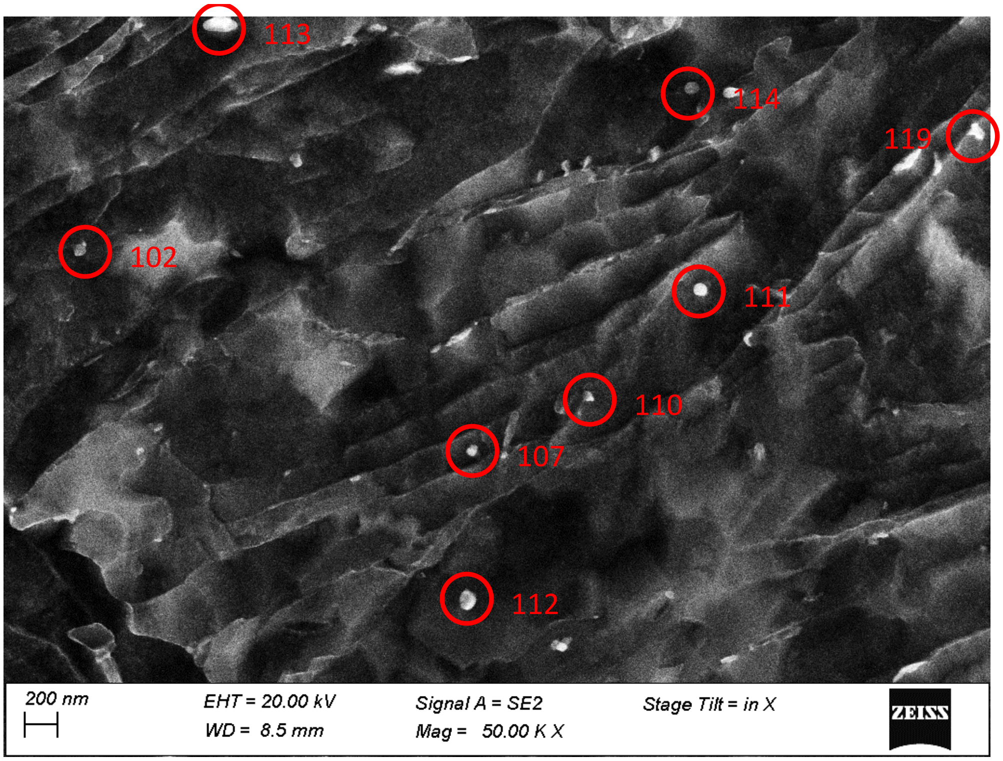

Spectrum (Wt%)	B	C	Si	P	**Ti**	Cr	Mn	Fe	**Nb**
102		6.45			**1.05**	0.25	1.45	86.37	**4.42**
107		8.07	0.26		**0.36**	0.33	1.46	84.77	**4.74**
110	7.27	11.14	0.23	0.05	**0.03**		1.46	79.81	
111		8.97	0.25			0.27	1.45	80.7	**8.36**
112		7.67	0.21		**0.53**	0.28	1.54	85.59	**4.19**
113		8.98	0.34		**1.01**		1.52	82.16	**5.99**
114	13.99	9.29	0.16		**0.71**	0.24	1.13	67.92	**6.56**
119		10.22	0.31			0.27	1.55	87.12	**0.54**

Figure 6.28 SEM-EDS analysis High-Nb steel deformed to 975°C and quenched after 20s. 100°C below experimental Tnr.

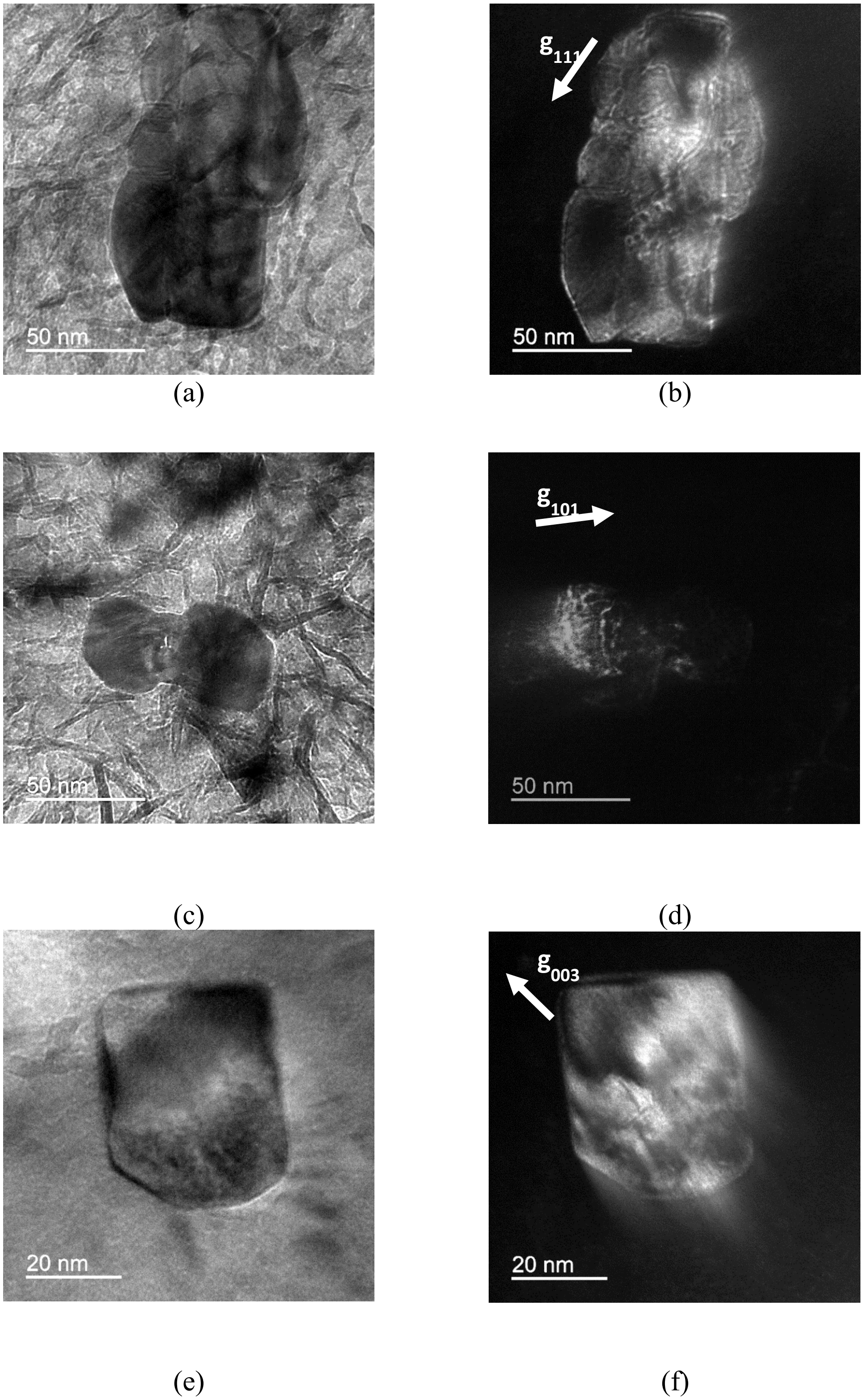

(a) (b)

(c) (d)

(e) (f)

	Wt%
C	6.4
N	14.6
O	66.42
Si	0.13
Cl	0.5
Ti	0.72
V	0.02
Cr	0.02
Mn	0.04
Fe	2.02
Cu	0.08
Nb	9.06

	Wt%
O	76.28
Si	0.7
Cl	1.83
Ti	0.27
V	0.04
Cr	0.07
Mn	0.22
Fe	9.29
Cu	0.35
Nb	10.96

	Wt%
N	75.65
Si	0.73
Cl	0.39
Ti	1.45
V	0.07
Cr	0.08
Mn	0.29
Fe	12.28
Cu	0.38
Nb	8.68

Figure 6.29 BF-DF and EDS of complex particles from deformed-delayed-quenched specimens of: (a), (b), (c) and (d) High-Nb Steel; (e) and (f) Low-Nb steel.

SEM had already shown the abundance of complex precipitates and TEM verified their intricate polycrystalline structure. Focused beam EDS performed in TEM showed simultaneous presence of Nb, Ti and V in these particles. The presence of this type of precipitates has reportedly lower the occurrence of strain induced NbC precipitates[94]. Strain-induced precipitation is minority in the present steels, there is not considerable solute segregation and Tnr was higher than predicted by empirical equations. It follows that the presence of complex particles must be responsible for recrystallization inhibition at 975°C in the present steels.

6.2.3 Recrystallization Inhibition at the Transfer Bar

To simulate what happens at the transfer bar, roughing simulation experiments were followed by a delay time. During this delay the specimen cooled as precipitates formed and achieved non-recrystallization conditions. The microstructure and precipitates before and after the delay time were studied to determine what controls recrystallization in both processes.

During rough deformation simulations, recrystallization was allowed through high deformation-high temperature passes. The conventional process comprises 75% thickness reduction in roughing, distributed in 6 passes. The IRCR process utilizes 85% deformation distributed in 8 passes (the first four passes were simplified in only two, hence both processes consisted of six passes). The more intensive roughing deformation of IRCR was expected to enhance precipitation and produce non-recrystallization conditions utilizing less alloying.

Microstructure of the specimens quenched right after the last deformation pass are shown in Figure 6.30 Optical micrograph of specimens quenched right after Conventional RCR roughing. Specimens processed by IRCR show finer microstructure than conventional RCR specimens. The grain size refines due to deformation-recrystallization cycles, and more nucleation area is provided which is beneficial for final properties.

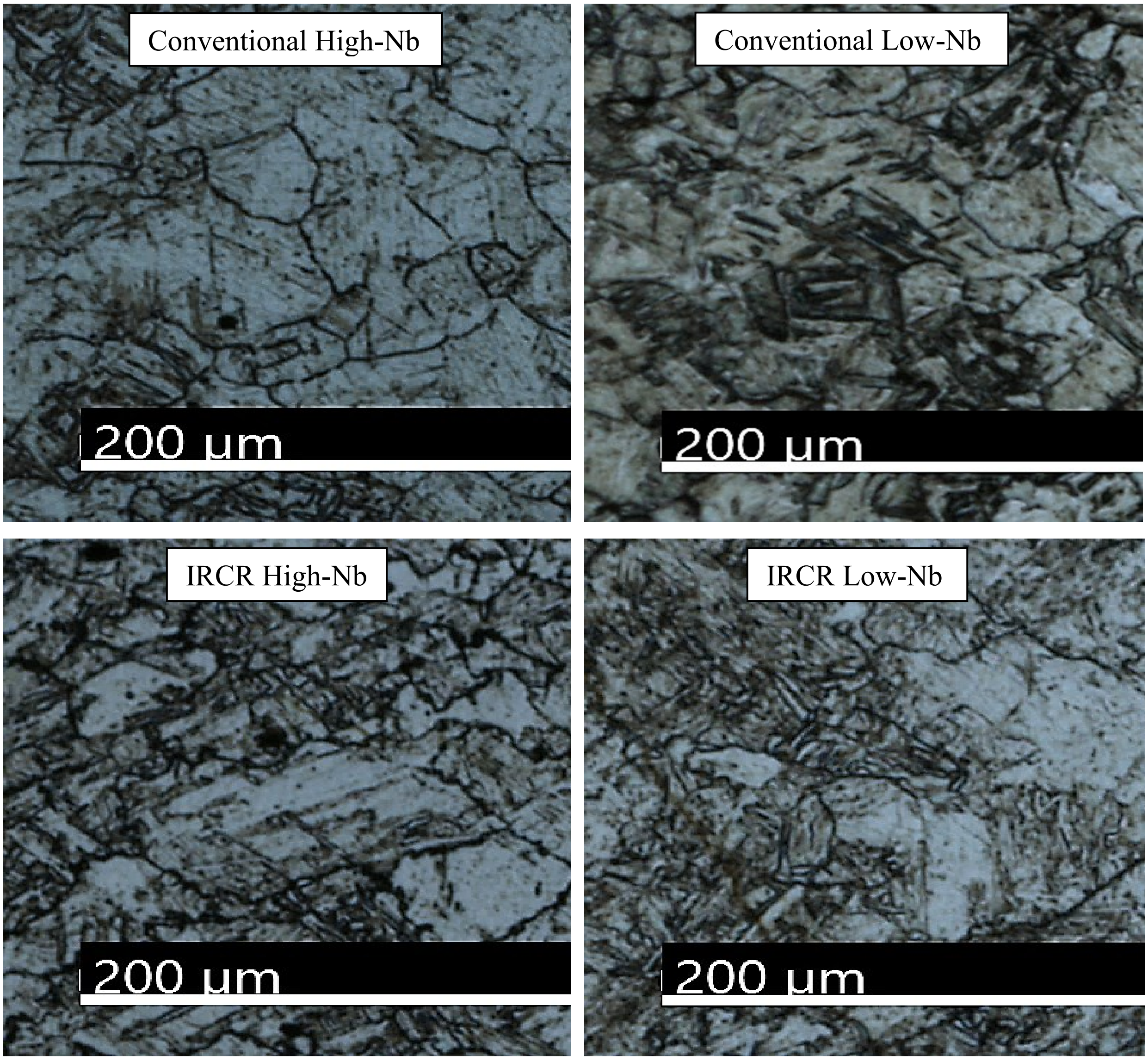

Figure 6.30 Optical micrograph of specimens quenched right after Conventional RCR roughing.

After the last roughing pass, a delay time was allowed for simulating the transfer bar. During this time the steel can recrystallize for the last time and precipitates form, that will prevent further recrystallization. Figure 6.31 shows the austenitic microstructure after the delay time. This can be regarded as the microstructure of the steel as it enters finishing deformation.

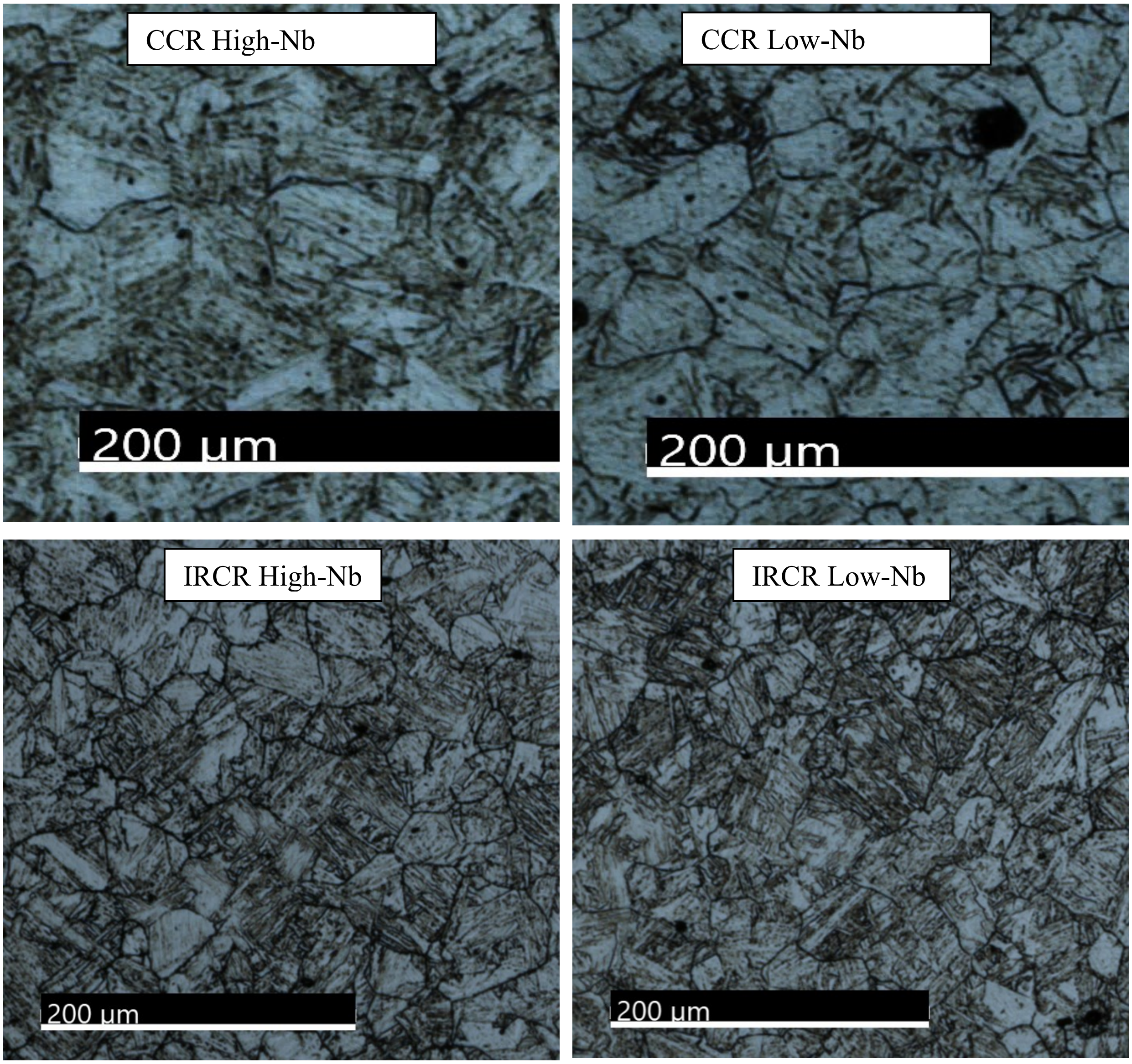

Figure 6.31 Optical micrographs of PAGS after roughing simulation + transfer bar simulation.

The comparison of precipitation before and after transfer bar simulation provided remarkable results that support the hypothesis. Samples were deformed following the roughing schedules of 75% thickness reduction for CCR and 85% for IRCR. The samples were quenched right after the last deformation pass. The experiments were repeated, but this time the transfer bar was simulated by a delay-time after the last roughing deformation, then quenched. In Figure 6.32, measurements of the precipitate size and volume fraction are presented for both High-Nb (H) and Low Nb(L). The 95% confidence intervals are shown at the size charts. Figure 6.32 shows more precipitate content in every steel, when processed by IRCR than CCR. This is true before and after the transfer bar. It is remarkable that the Low-Nb steel, processed by IRCR, has more precipitates than the High-Nb steel processed by CCR. The higher volume fractions in IRCR can be explained as a consequence of the higher strain applied in roughing. This is called strain induced precipitation. Having bigger precipitates and volume fraction in the IRCR process is indication that precipitation was optimized.

An example of the precipitation at the transfer bar of IRCR process can be seen in figure Figure 6.33. The big precipitates were observed after reheating, so it is assumed they are pre-existing to roughing. The new precipitation, during roughing and transfer bar, happens in little ~3nm particles and on the pre-existing particles.

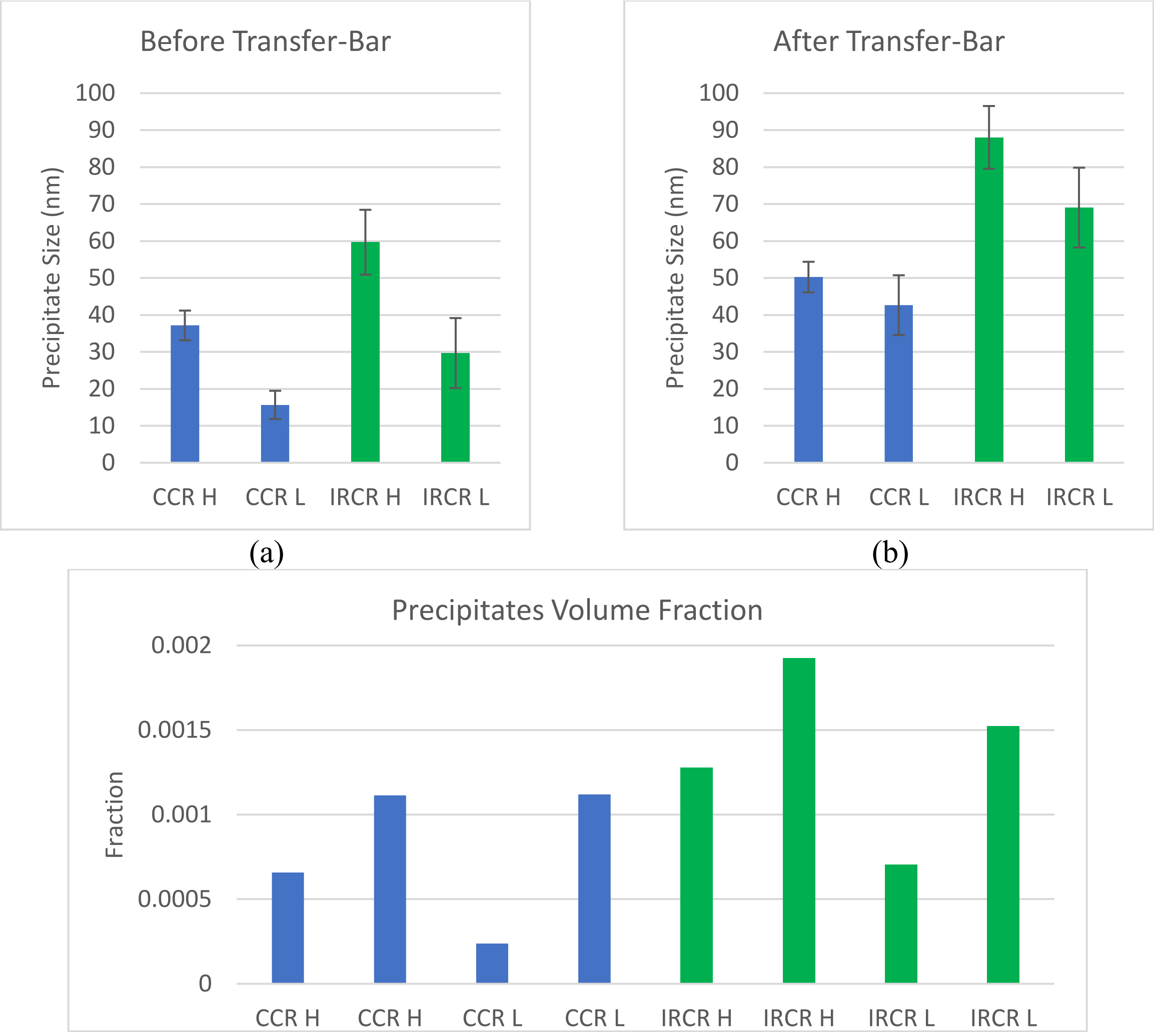

(a)

(b)

(c)

Figure 6.32 Precipitation measurements before and after transfer bar simulation. H stands for High-Nb and L for Low-Nb

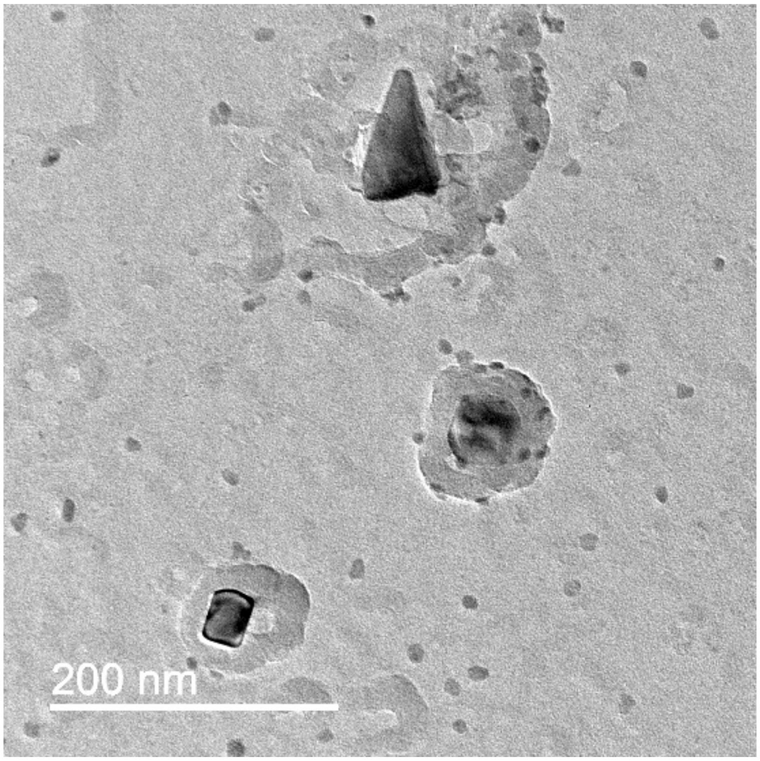

Figure 6.33 TEM micrograph of IRCR Low-Nb steel after transfer bar.

Precipitate volume fractions obtained from measurements after transfer bar simulations in Figure 6.34 provide pinning forces that inhibit recrystallization. Using the Zener's flexible model (from Table 3.2) the pinning forces after transfer bar are 9.54 MPa and 8.94MPa for High-Nb and Low-Nb steels respectively. Meanwhile, the recrystallization force (see Equation 6-44) given the increase in stress is 0.18 and 0.23MPa for high-Nb and low-Nb steels respectively. These values guarantee no-recrystallization conditions for finishing operations, regardless of any solute drag that could be present.

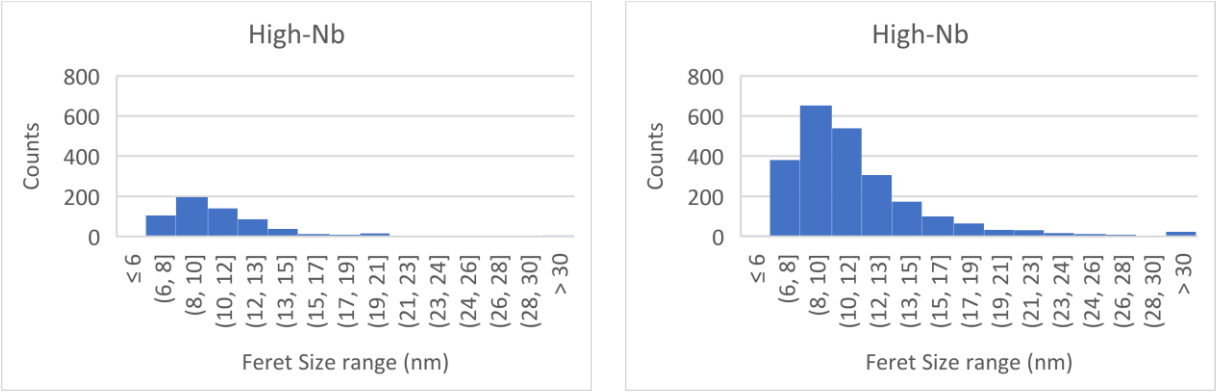

Average PPT size	10.94	nm
SD	6.90	nm
Volume fraction	0.00456	

(a)

Average PPT size	11.50	nm
SD	6.90	nm
Volume fraction	0.01926	

(b)

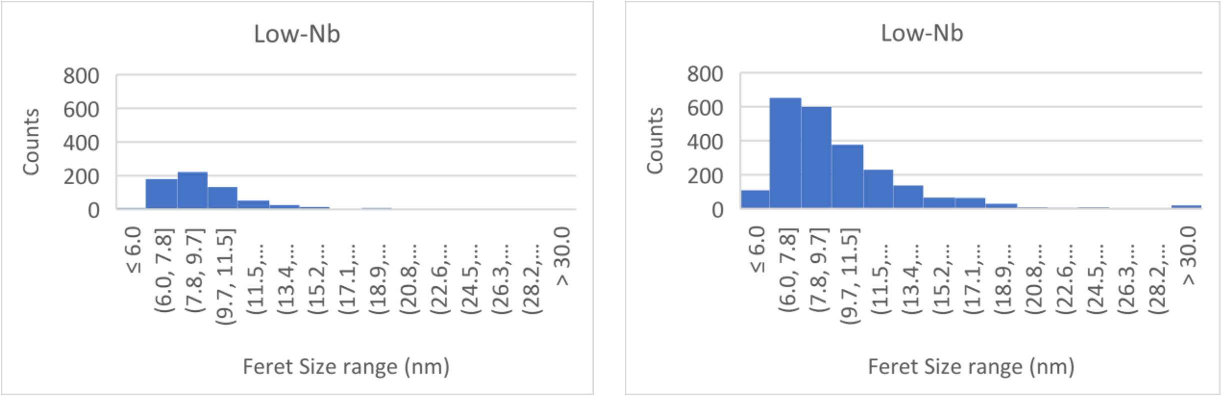

Average PPT size	10.06	nm
SD	4.87	nm
Fraction	0.00491	

(c)

Average PPT size	10.21	nm
SD	5.26	nm
Volume fraction	0.01476	

(d)

Figure 6.34 Precipitate size distribution of IRCR steels: (a) High-Nb Q; (b) High-Nb DQ; (c) Low-Nb Q and (d) Low-Nb DQ.

6.2.4 Austenite Conditioning During Hot Deformation Experiments

Austenite conditioning was evaluated utilizing two techniques: by measuring the effective nucleation area, Sv, and by mapping the Kernel Average Misorientation (KAM) through EBSD. Both techniques agreed in the high nucleation potential of the IRCR process, this later derived in fine-homogeneous microstructure.

Mathematically, the Sv value is defined by Kozasu as[129]:

$$\boldsymbol{S_V(gb+db) = 0.429(N_L)_{||} + 1.571(N_L)_{\perp}} \qquad \textbf{(6-45)}$$

Where $(N_L)_{||}$ and $(N_L)_{\perp}$ represent the number of intersections per unit length in the directions parallel and perpendicular to the elongated grains. The counting was done manually with the aid of the software ImageJ (See Figure 6.35) considering a total of 5000μm in every direction.

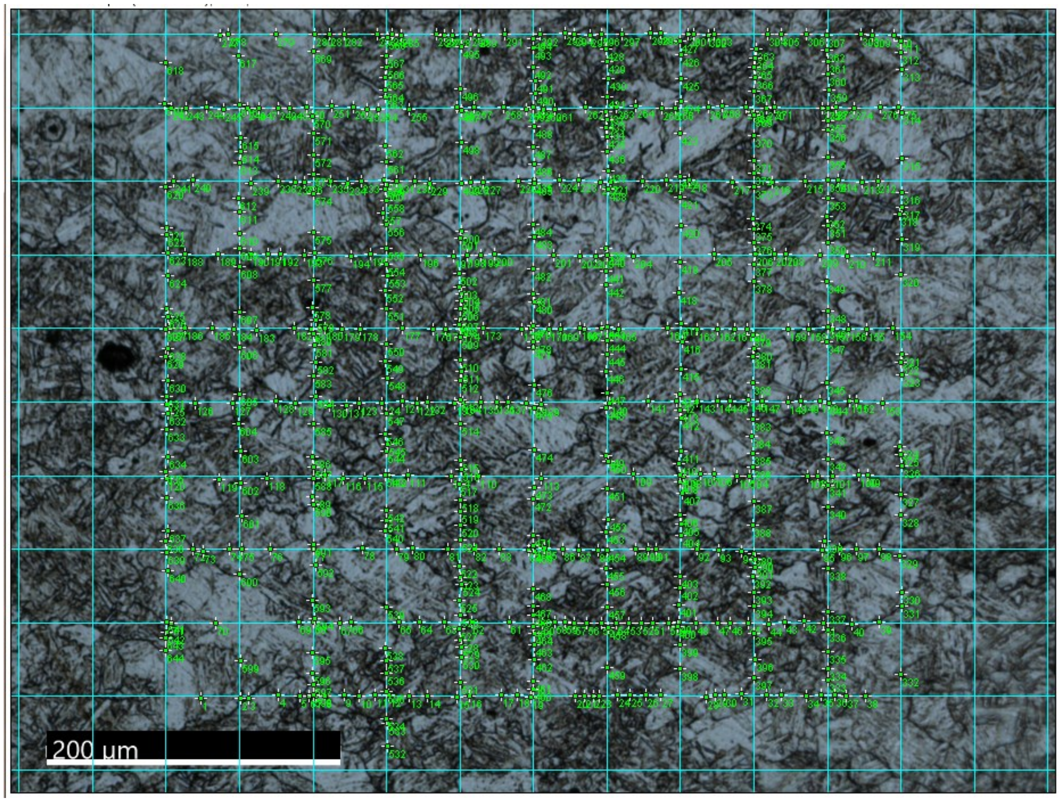

Figure 6.35 Counting of intersections for measurement of Effective Nucleation Area, Sv. Sample deformed by IRCR process and quenched immediately after last pass.

The Sv value was obtained from the samples quenched right after the last roughing deformation (Figure 6.36) and the samples quenched after the delay time that simulates transfer bar (denoted as DQ). The results presented in Figure 6.36 show a slightly higher Sv value for the specimens deformed by IRCR. This result is naturally expected due to the higher deformation. The higher Sv value for IRCR at this point of the process provided a positive feedback for the possibility of a fine and homogeneous microstructure with Low-Nb.

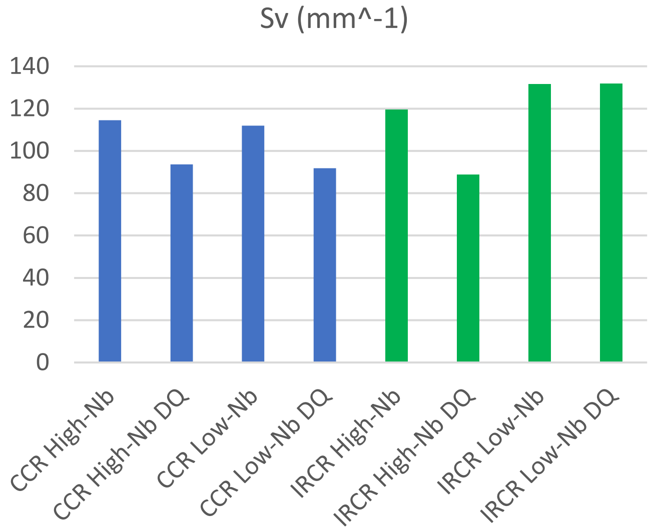

Figure 6.36 Effective Nucleation Area (Sv) results from specimens after roughing simulation.

Electron Backscatter Diffraction maps were built from specimens quenched right after the last roughing pass. From the martensitic EBSD maps austenitic maps were obtained as explained before. Then KAM maps were generated from the regenerated austenitic EBSD maps. KAM maps are widely accepted for observance of Geometrically Necessary Dislocations (GND). KAM maps on Figure 6.37 show a dislocation-rich microstructure generated form the IRCR process. The KAM on Low-Nb steel rivals that of the High-Nb on both conventional and IRCR processes. From these results it is apparent that at this point of the process the High-Nb steel offers no advantage over the Low-Nb steel.

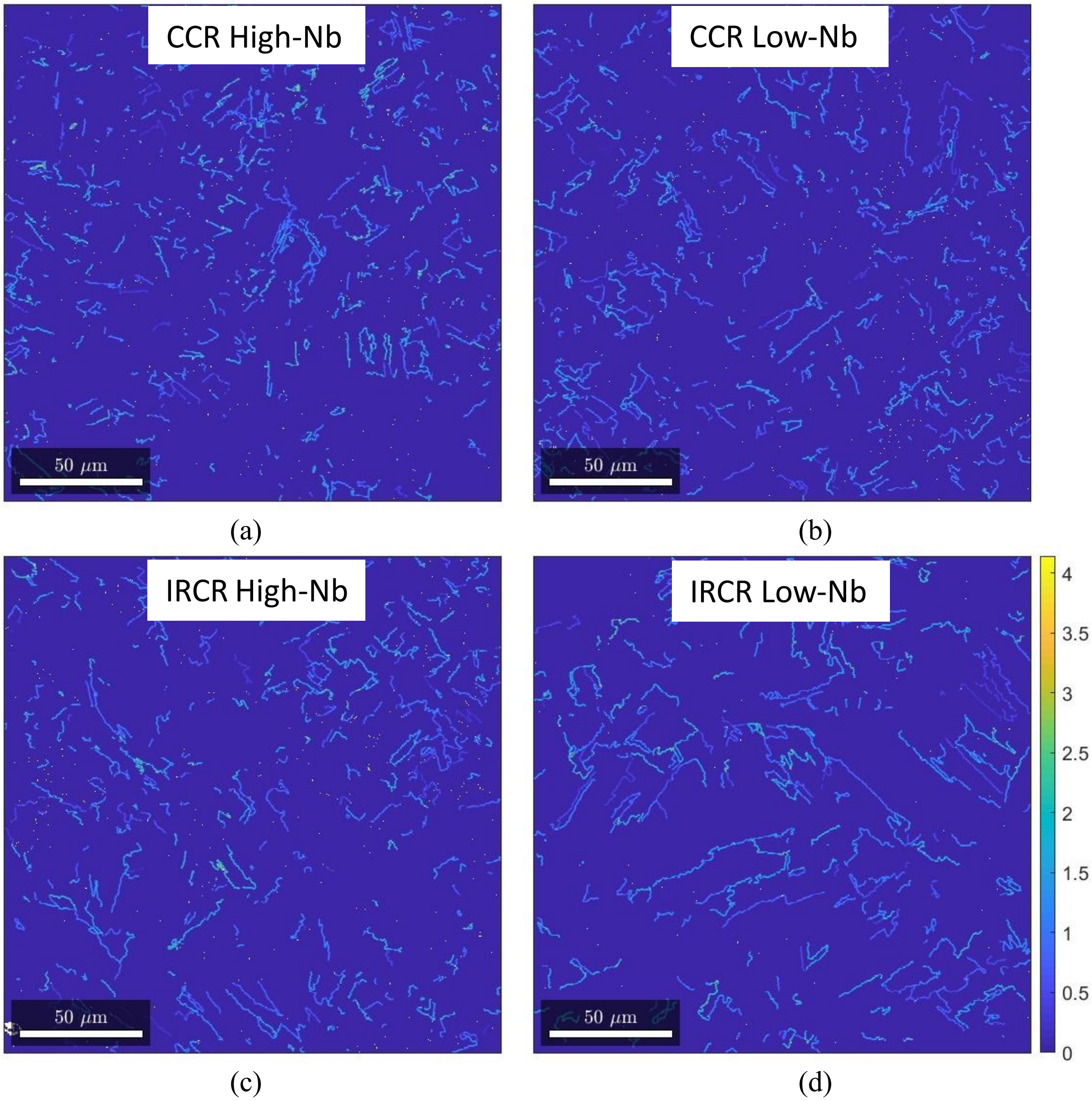

(a) (b) (c) (d)

Figure 6.37 KAM maps from regenerated austenite EBSD maps of specimens quenched right after last roughing pass. Color code shows misorientation in degrees.

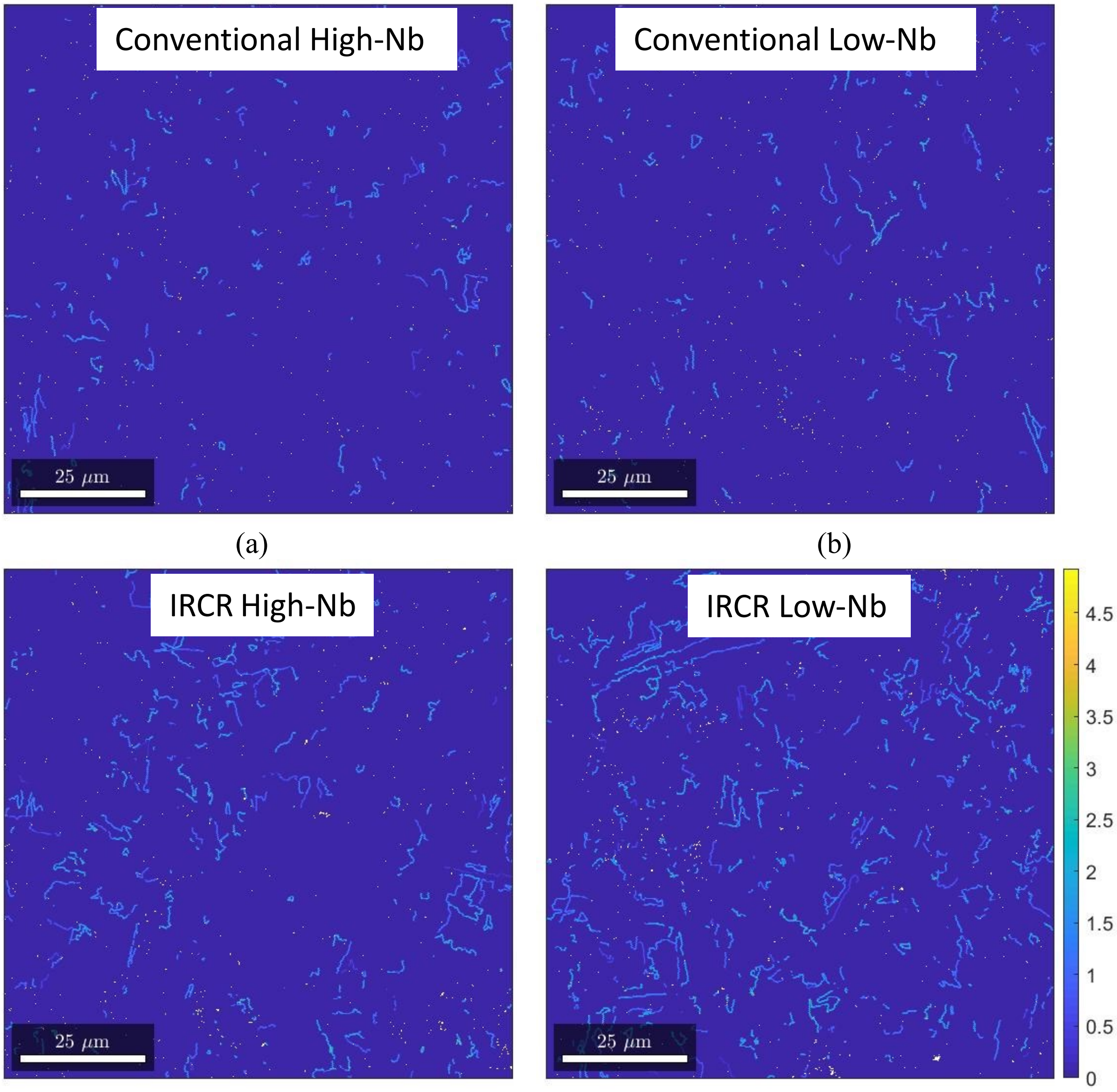

(a) (b)

(c) (d)

Figure 6.38 KAM maps from regenerated austenite EBSD maps of specimens quenched right after last finishing pass of torsion tests. Color code shows misorientation in degrees.

Austenite conditioning was also assessed on specimens quenched right after the last pass of finishing deformation in torsion tests. Austenite conditioning at this point is critical for the final transformation that occurs right after this point during accelerated cooling and coiling.

KAM maps on Figure 6.38 show a considerably higher dislocation density on the IRCR processed specimens. This derives in more available nucleation sites for the final transformation. Hence one should expect a finer microstructure from the IRCR process than the conventional.

To understand why the IRCR process, despite having less deformation under non-recrystallization conditions, shows higher dislocation density one must look at the deformation schedule. Recalling Figure 5.2, the distribution of deformation can be observed. During finishing, the 67% deformation of the conventional process is distributed among the typical 7 finishing passes. Meanwhile, the 46% deformation of IRCR finishing is concentrated on two passes only, at a much lower temperature. Considering non-recrystallization conditions, the only phenomenon that can be responsible for such difference in KAM is recovery.

Recovery is capable of rearrangement and annihilation of dislocations. Although more evident in pure metals, where dislocations travel more freely, recovery can considerably rearrange and decrease dislocation density[130]. Stored energy from deformation is the driving force for recovery and recrystallization, and temperature strongly influences dislocation mobility[60]. The high deformation passes in the IRCR are more likely to induce recovery. The re-arrangement of dislocations then derives in more visible local misorientation i.e. KAM.

6.3 Validation Experiments Results

6.3.1 Austenite Conditioning

Consistency was found between austenite conditioning of rolled specimens and torsion specimens. When analyzing the finished rolled specimens KAM maps, shown in Figure 6.39, the trend is like that of torsion KAM maps in Figure 6.38. The specimens that went through IRCR show the most kernel average misorientation. This is indication of a more deformed structure, with more readily available nucleation sites.

The specimens quenched right after last rolling pass were mapped by EBSD with the same technique as previously deformed specimens. The martensitic OIM scans were used for re-constructing austenitic OIM maps. KAM maps were extracted from the reconstructed austenite maps. In Figure 6.39 KAM calculations consider first nearest neighbors and maps misorientations from 0 to 5 degrees.

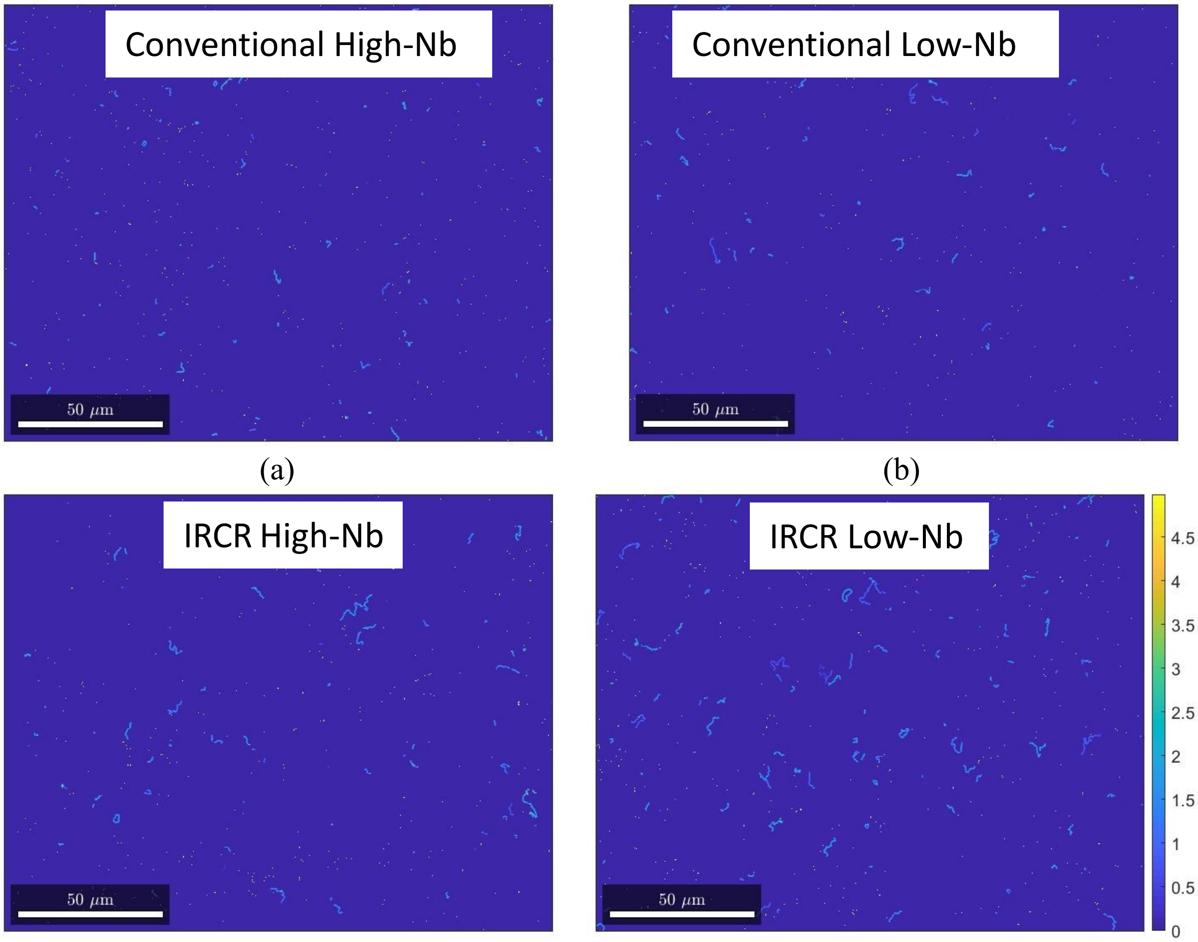

(a) (b)

(c) (d)

Figure 6.39 KAM maps from regenerated austenite EBSD maps of specimens quenched right after last finishing pass of rolling.

6.3.2 Transformation and Grain Refinement Results

The final microstructures denoted similar average grain sizes in all four final conditions, the IRCR-processed steels had only 5-10% smaller grains. Transformation was slightly different, carbon-rich constituents, including MA, had more presence in CCR specimens. MA, however, had more presence in the IRCR specimens. The size of MA was rather small, less than 1.5µm.

Figure 6.41 shows SEM micrographs of the resulting microstructures. The following microstructural constituents can be observed: Polygonal ferrite (PF), acicular ferrite (AF), granular bainite (GB) and its associate Martensite-Austenite (MA).

PF, formed at high temperatures, is not the best constituent for toughness. PF has relatively large size as compared to AF. PF presence increases the effective grain size. More undesirable is MA, this constituent is well known for its detrimental effect on toughness. MA formation starts with the formation of carbide-free bainite which leads to enrichment and stabilization of untransformed austenite. Later, this enriched austenite may form carbides and MA if cooling is not fast enough[32]. To avoid MA, faster cooling is necessary that avoids the formation of GB, preventing austenite from enriching in carbon and stabilizing.

MA was quantified from SEM micrographs; the average size was close to 1.4µm in all alloys. The area fractions were: 0.0033 in the CCR High-Nb steel; 0.0035 in the CCR Low-Nb steel; 0.0078 in the IRCR High-Nb steel and 0.0075 in the IRCR Low-Nb steel.

Further phase volume fraction analysis, by EBSD Image Quality (IQ), showed higher fractions of C-rich constituents in the CCR steels (see Table 6.5). These C-rich constituents were considered as MA plus carbides.

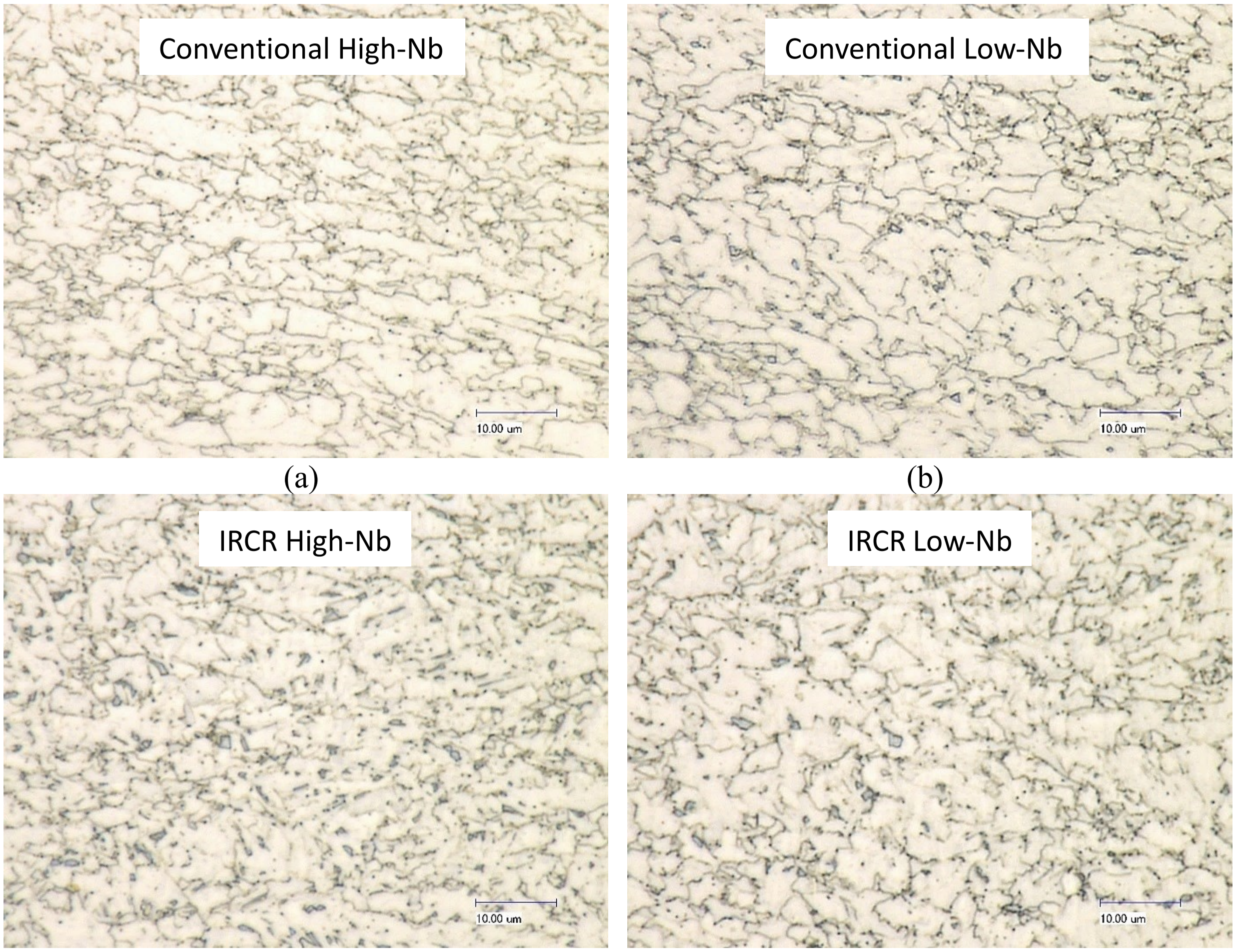

(a) (b)

(c) (d)

Figure 6.40. Optical micrographs of final microstructures revealed by Marshall's etchant.

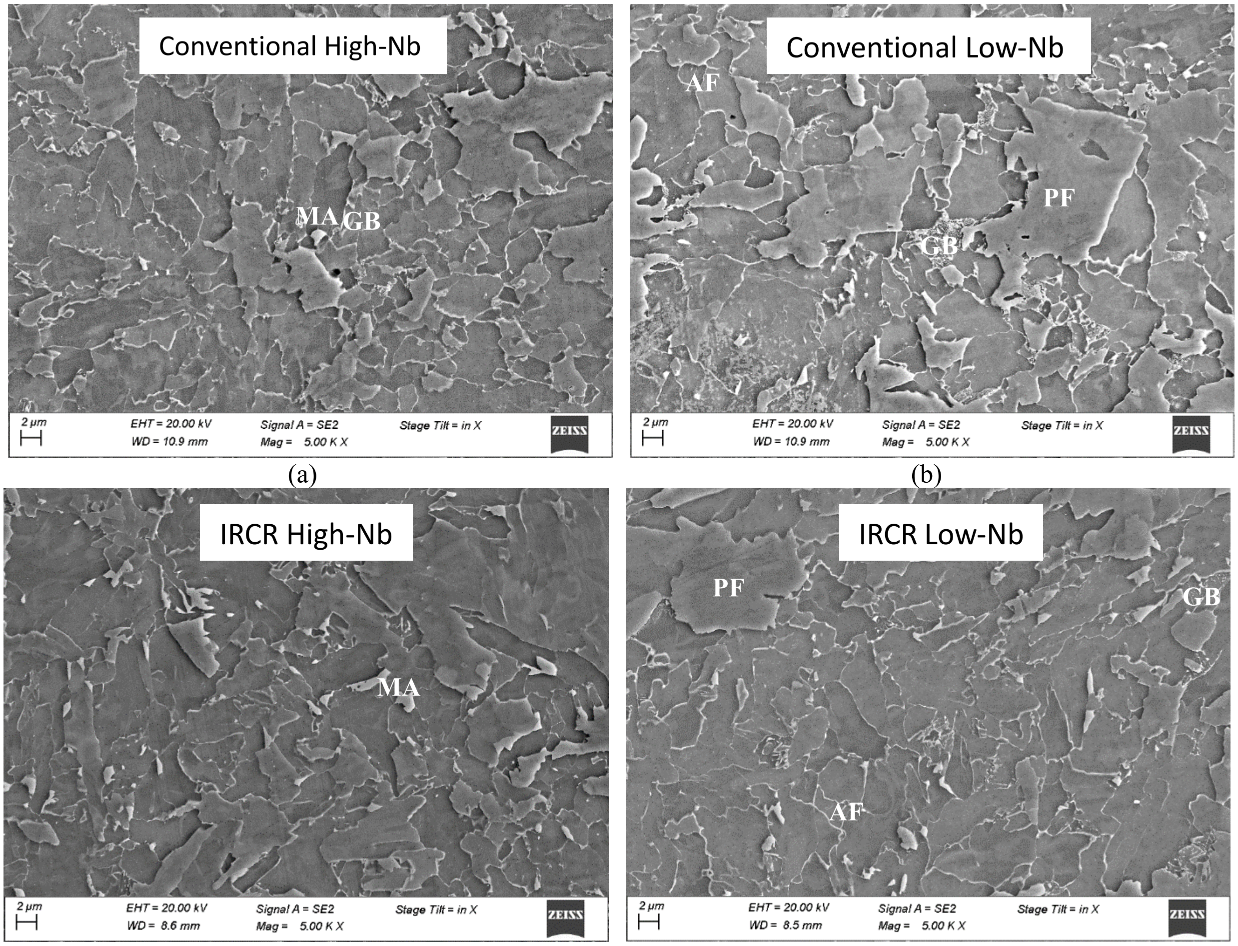

(a) (b)

(c) (d)

Figure 6.41 SEM micrograph of the final microstructures, obtained from ACC.

Table 6.5 Micro-constituents quantifications by EBSD – IQ analysis.

Constituent	CCR High-Nb	CCR Low-Nb	IRCR High-Nb	IRCR Low-Nb
Polygonal ferrite	55.39%	53.17%	60.91%	54.55%
Non-polygonal ferrite	41.26%	44.34%	38.11%	44.55%
C-rich constituents	3.35%	2.50%	0.98%	0.91%

The EBSD-IQ analysis is based on similitude of the scanned points to the database definition of ferrite. The IQ is a numeric representation of band contrast in Kikuchi patterns. Band contrast is better when the crystal is not distorted, hence, high IQ values represent low strain or strain-free crystallites[131]. In the present analysis, low IQ was associated to phases other than ferrite, and interpreted according to the recommendations by Wu[131].

Figure 6.42 is a normalized frequency distribution of the IQ of every point in the EBSD scan of specimen CCR Low-Nb. By simulating a regression, the total distribution can be broken in smaller, normal population groups that can be interpreted as microstructural constituents. From these curves' populations, the fractions of those constituents were obtained.

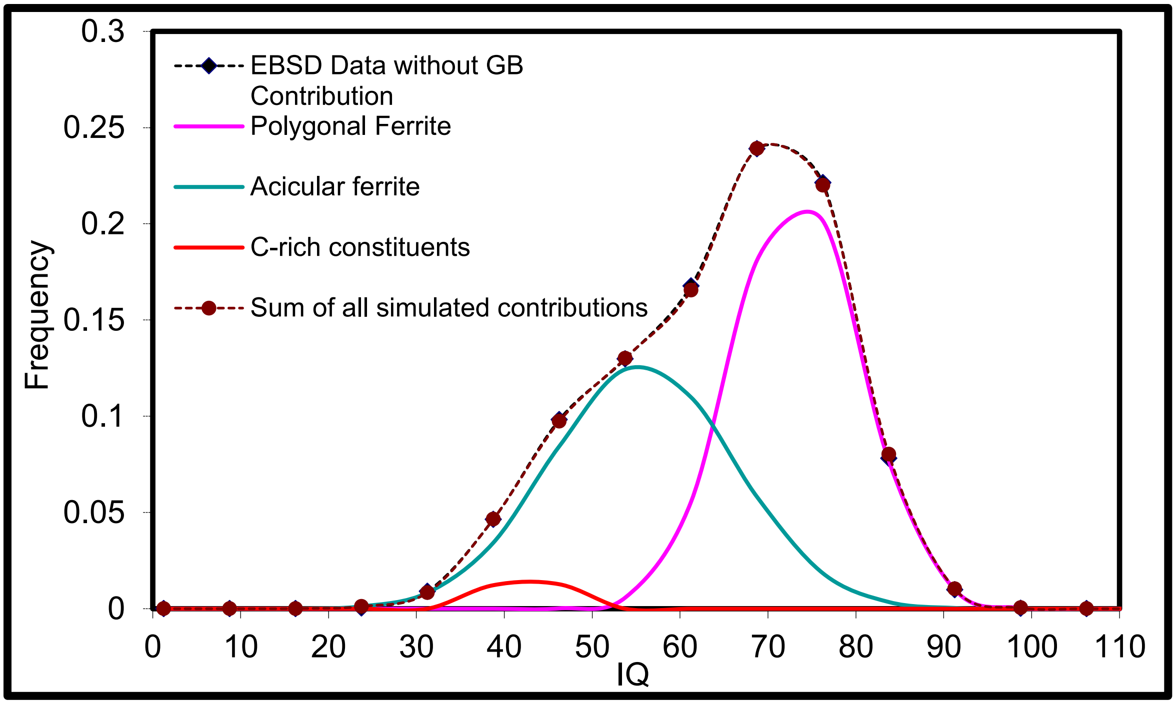

Figure 6.42 EBSD IQ analysis of CCR Low-Nb steel.

6.3.3 Effective Grain Size

Microstructural grain size resulted slightly smaller than effective grain size. Microstructural grain size was assessed through OM micrographs of Marshalls etched specimens, whereas effective grain size was obtained from EBSD scans.

Effective grain size was assessed through EBSD by considering 15° misorientation boundaries, as suggested by the literature[42]. 15° misorientation boundaries are considered to limit UCP. Later, SEM micrographs of fractured Charpy specimens were used for comparison, by measuring the CFS. In Figure 6.43 the microstructural grain size is compared to the effective grain size, based on grain boundary misorientation.

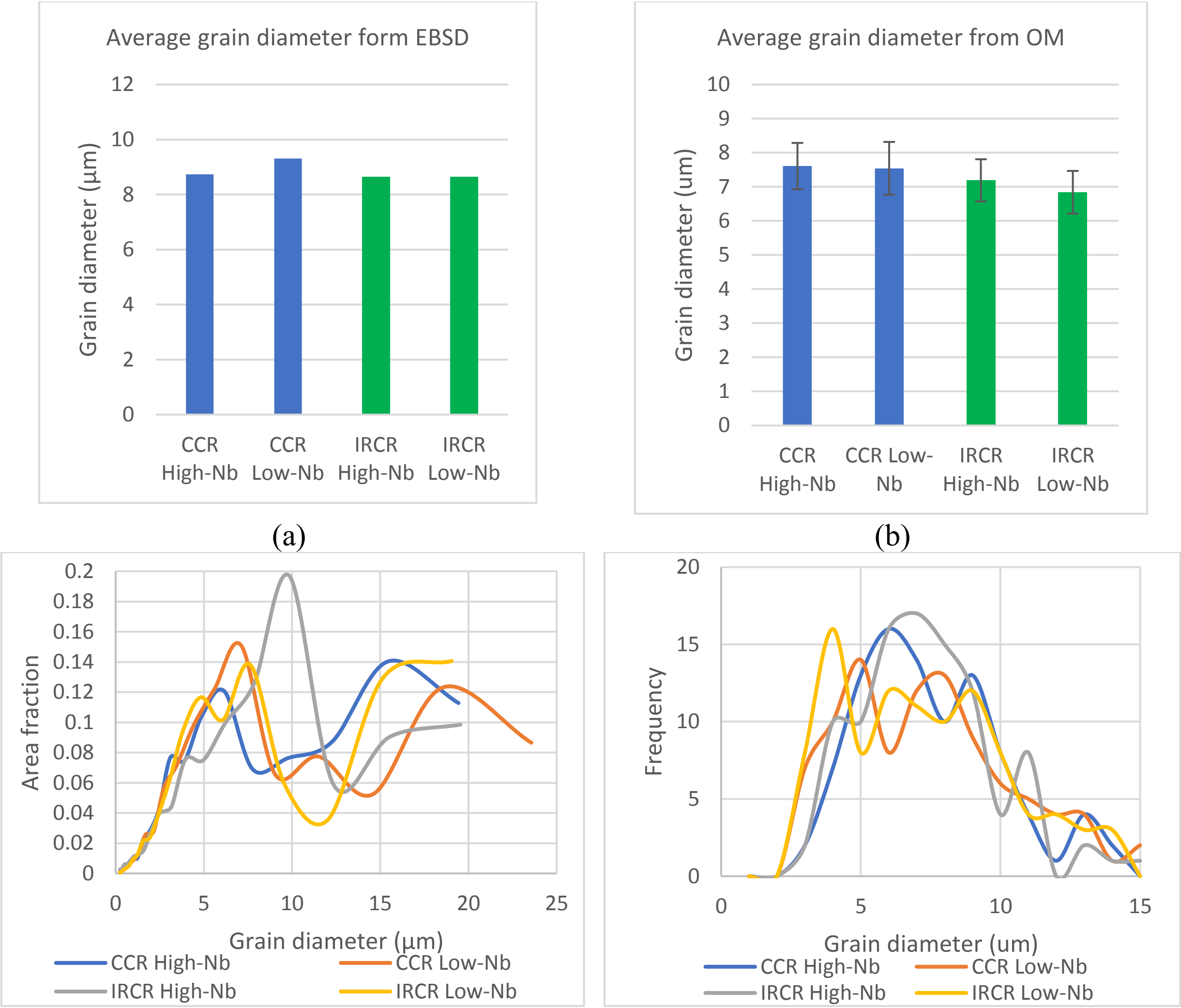

(a) (b)

(c) (d)

Figure 6.43. Grain size measurements from (a) GB with misorientation >15°; (b) Marshall's etchant and OM; Grain size distribution of: (c) EBSD based measurements; (b) Marshall's etching OM-based measurements.

6.3.4 Precipitation in a Nb-Ti Steel Processed by IRCR

Precipitation assessed in the final specimens shows a recollection of particles formed at different stages of the process. Undissolved precipitates from reheating, precipitates formed during roughing deformation, during transfer bar and during final cooling. SEM micrographs, and TEM were used for assessing precipitation. Thin foils for determining precipitates type and coherency to the matrix, and C-replicas for quantification.

Figure 6.44 (a) shows a similar average precipitate size for all four steels, the standard deviation speaks of a broad size distribution. Figure 6.44 (b) shows the precipitate volume fractions. The volume fractions are consistent with the MA volume fraction trend, which is opposite. This may mean that MA formation disrupted precipitate formation during coiling. These final volume fractions contrast with those of transfer bar, where the higher deformation of IRCR promoted a more numerous nucleation than CCR. These results show room for improvement, if the appropriate cooling is done to reduce MA precipitate volume fraction can increase. Consequently, yield strength and toughness can improve.

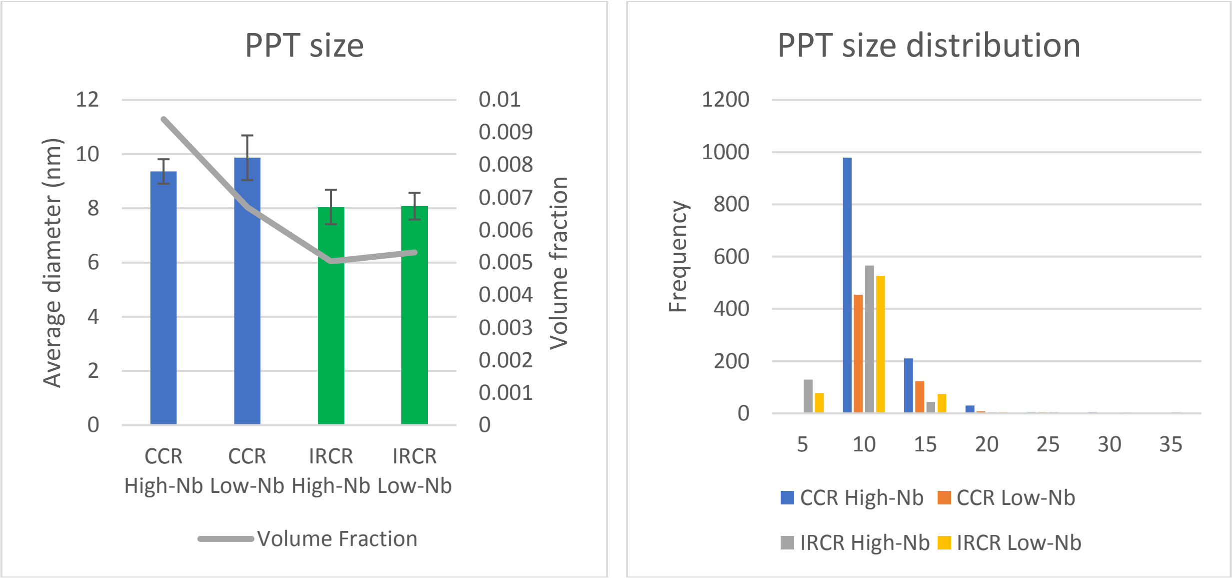

(a) (b)

Figure 6.44 Final precipitates: (a) size and volume fraction; (b) size distribution.

The progress of precipitate content throughout the process can be seen in micrographs on Figure 6.45 for the High-Nb CCR and for the Low-Nb steel IRCR. It can be noticed that the IRCR-processed steel has copious precipitation happening after roughing, but not as much after the final transformation.

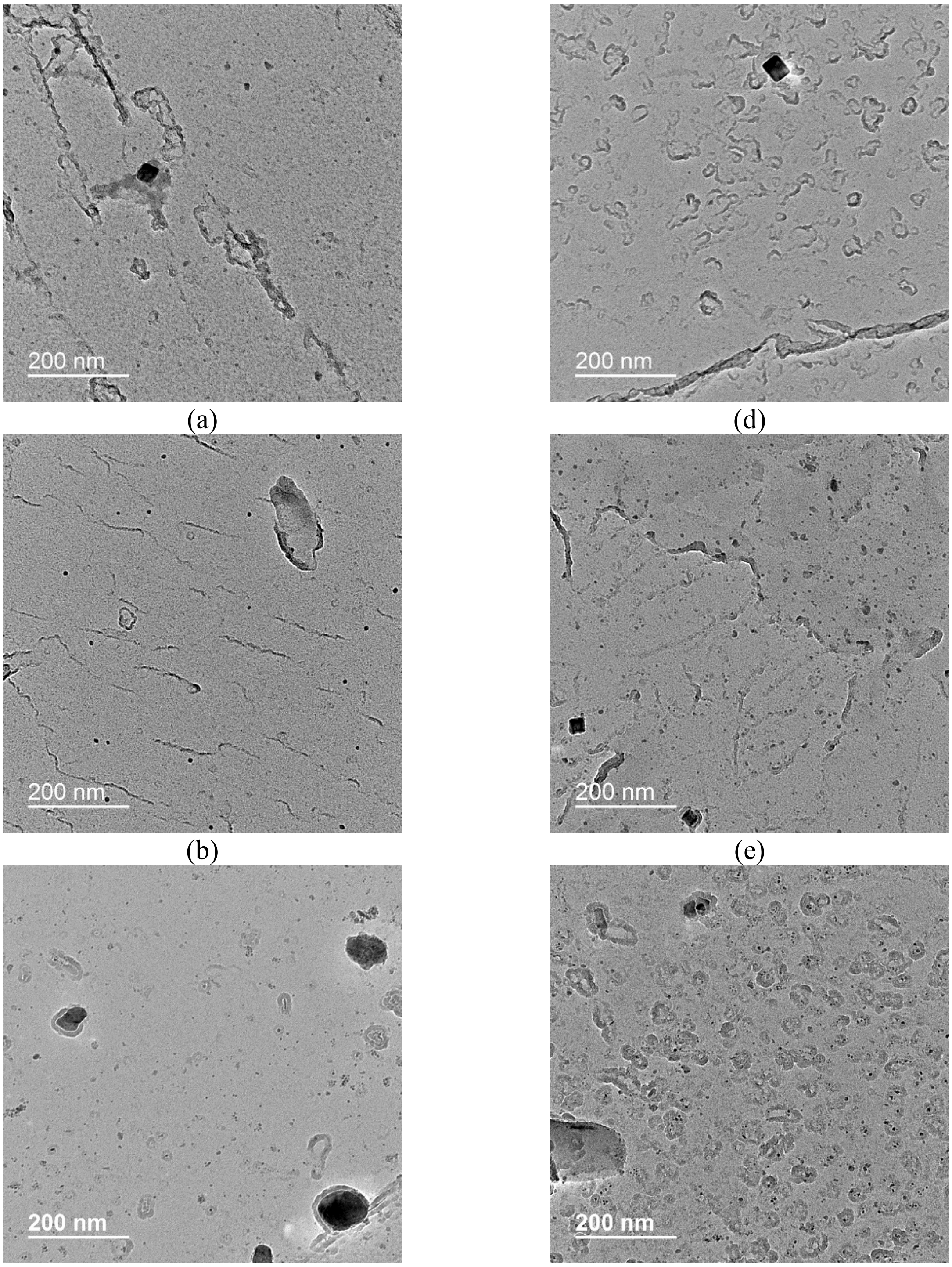

(a) (d)

(b) (e)

(c) (f)

Figure 6.45 Precipitation progress during hot processing: of CCR High-Nb (a) after reheating, (b) after roughing, (c) fully processed; and of IRCR Low-Nb (d) after reheating, (e) after roughing and (f) fully processed. 20 000X.

6.3.5 Texture Analysis Results

Few fiber components related to toughness were detected in the validation specimens. Texture was obtained from the EBSD OIM scans of the validation samples. Special attention was paid to those fiber components that may affect toughness negatively or positively, as discussed in section 2.2.4.

The most relevant texture fibers in steel can be observed by plotting the Orientation Distribution Function (ODF) at the Euler space, sectioned at $\varphi_2 = 45°$. In hot rolled products, the orientations along the RD and TD fibers shown in Figure 6.46 are common[47]. The critical components that have been negatively related to toughness in the literature are marked red, and the only component related to toughness improvements is marked green.

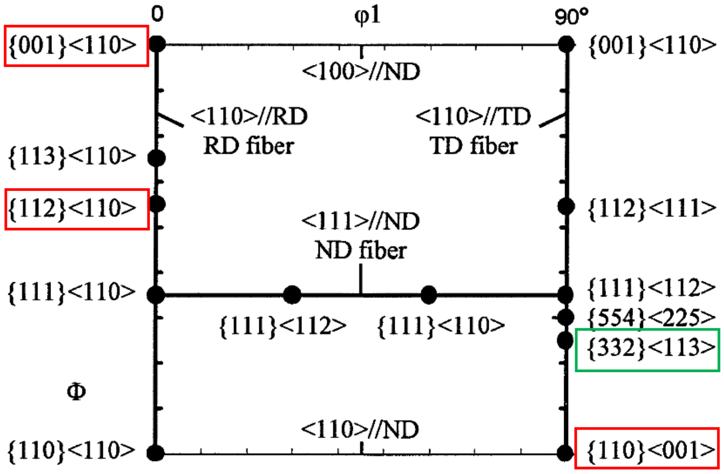

Figure 6.46 Cross-section of Euler space showing relevant fibers and orientations[47].

Only two components of α-fiber related to poor toughness were detected in the conventional process specimens. Component {100}<110> had a high value in the CCR High-Nb steel. Component {112}<110> in CCR Low-Nb steel had a slightly high value. In the IRCR High-Nb steel, one component of ε-fiber related to poor toughness was slightly high, component {110}<100>. Component {332}<113> of ε-fiber related to positive toughness is high in CCR High-Nb steel. See Figure 6.47. No texture fiber components that may affect toughness were detected in the proposed IRCR Low-Nb steel.

6.3.6 Mechanical Tests Results

IRCR processed steel with Low-Nb complied to API X70 mechanical requirements. This demonstrates the scalability of the IRCR process.

Hardness of the IRCR processed specimens was superior to that of CCR specimens. Microhardness Vickers was performed in an array through thickness, showing rather flat profiles for all four final conditions. Using 300g for 10s, the average HV300 hardness values are presented in Table 6.6. IRCR specimens are about 6% harder than CCR specimens. Hardness variability is, however, slightly higher for the IRCR processed specimens. Hardness values are consistent with the observed microstructure.

IRCR processed steels showed higher strength than CCR. Tensile test results are consistent with microhardness results. Ultimate Tensile Strength (UTS) followed the same pattern as hardness, it was higher for IRCR and for High-Nb, as compared to their counterparts. The 0.2% offset Yield Stress (σ_y) did not show a clear trend regarding Nb content, but it was higher for the CCR processed steels.

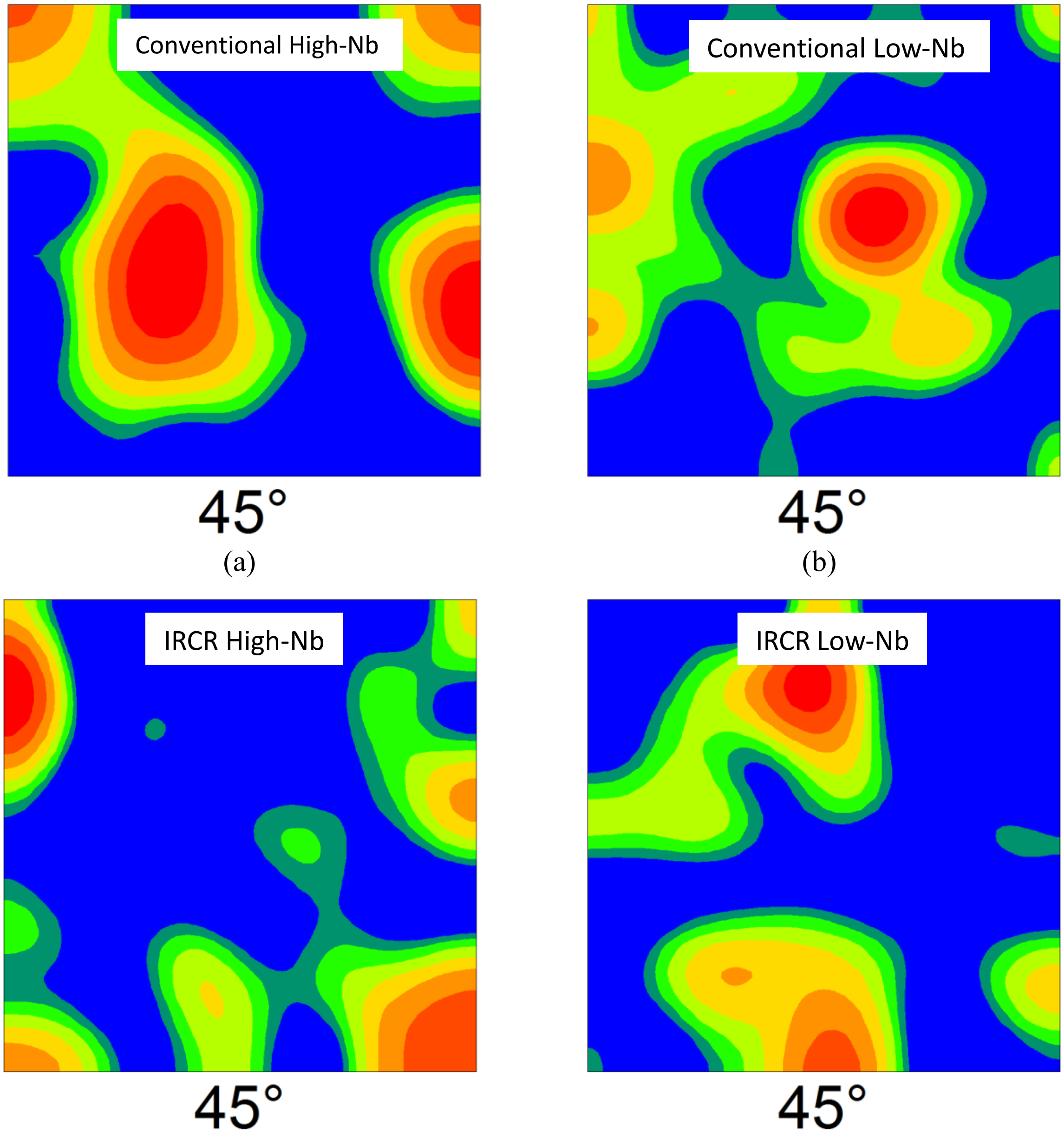

(a) (b)

(c) (d)

Figure 6.47 ODF section at φ_2=45°. Use previous Figure 6.46 as guide to navigate these maps.

Table 6.6 Microhardness and tensile test results from fully processed full thickness specimens.

	HV300	HV300 SD	σ_y (KSI)	UTS (KSI)	Elongation %
CCR High-Nb	224	6.2	78727.71	93344	37.2%
CCR Low-Nb	218	7.5	75250.64	89718	35.2%
IRCR High-Nb	239	7.8	70536.29	95675	31.5%
IRCR Low-Nb	231	11	75226.22	93336	31.4%

The occurrence of secondary cracks, also known as splitting, was observed along the tensile axis on CCR specimen. This can be attributed to the inhomogeneity of the CCR material microstructure observed by OM and SEM. This slipping mode of fracture was not observed on the IRCR specimens as can be verified on Figure 6.48.

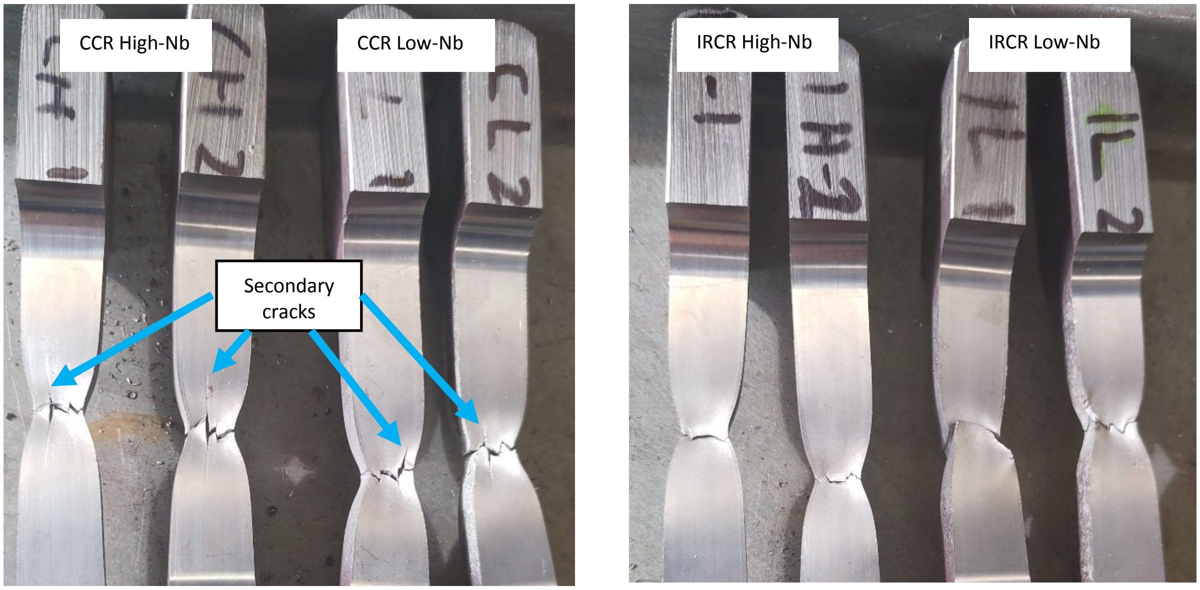

(a) (b)

Figure 6.48 Type of fracture observed during tensile tests.

Impact toughness performance was best in the Low-Nb steels. Impact toughness was assessed by Charpy V-notch test. The results present on Figure 6.49 show the improved toughness when compared to the commercial (High-Nb) HTP steel labeled “HH”. Steels HH, AR and AC were presented in section 4.3. Steels AR and AC Nb content is comparable to our Low-Nb steel.

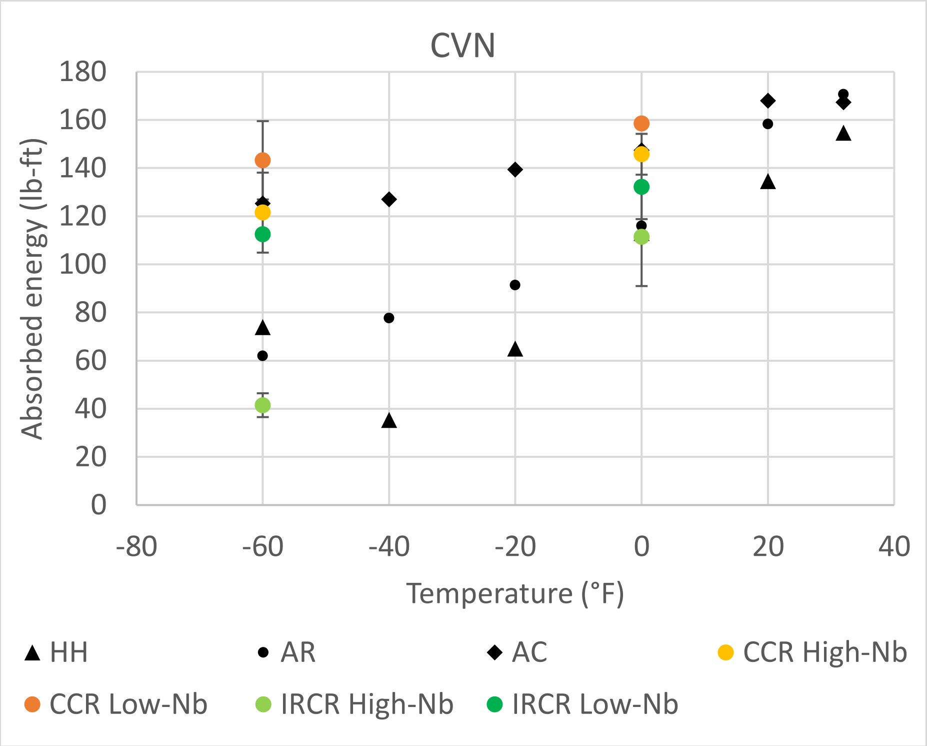

Figure 6.49 Charpy V-notch impact test results.

Low-Nb demonstrated better impact toughness than High-Nb steels. This is evident in absorbed energy, as well as % ductile area, as shown in Figure 6.50.

Fractography done on the Charpy specimens (Figure 6.51) revealed the fracture mechanisms at 0°F and -60°F. The ductile fracture from 0°F presented a mixed size of dimples ranging from 0.5µm to ~50µm.

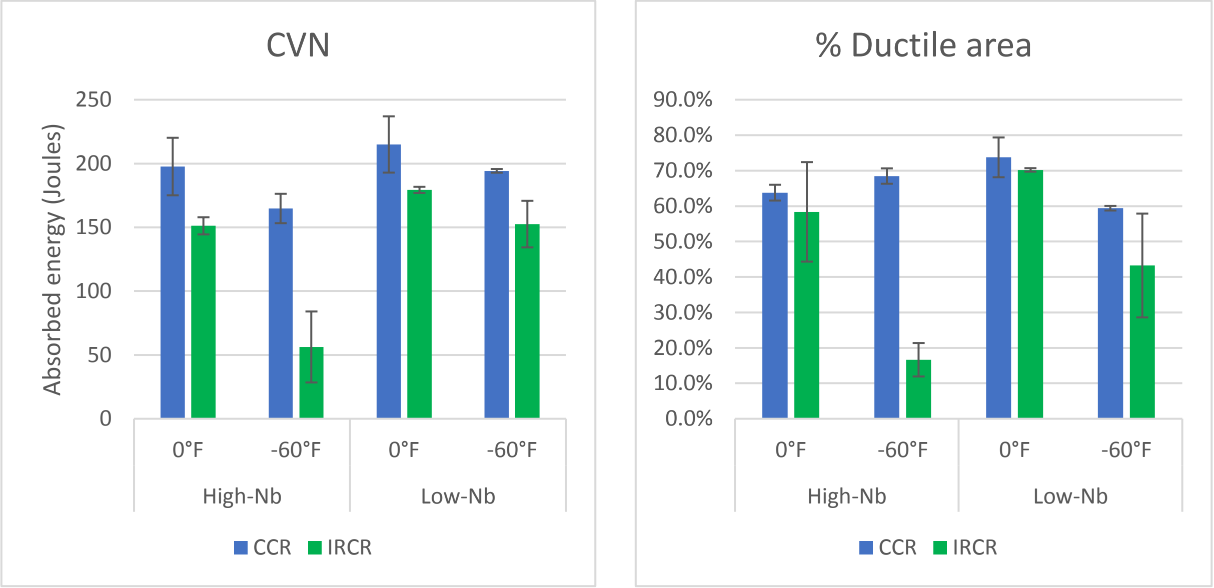

(a) (b)

Figure 6.50 Comparison of impact toughness of High vs Low-Nb.

A variety of initiating particle sizes might have caused the broad distribution of dimple size. Non-metallic inclusion particles were identified by EDS, inside the big dimples (Figure 6.52), such as: aluminum oxides, calcium oxides and manganese sulfides, ranging from 2-5µm in diameter. Meanwhile, inside the small dimples, silicon and chromium carbide particles were identified, ranging 150nm and below in size.

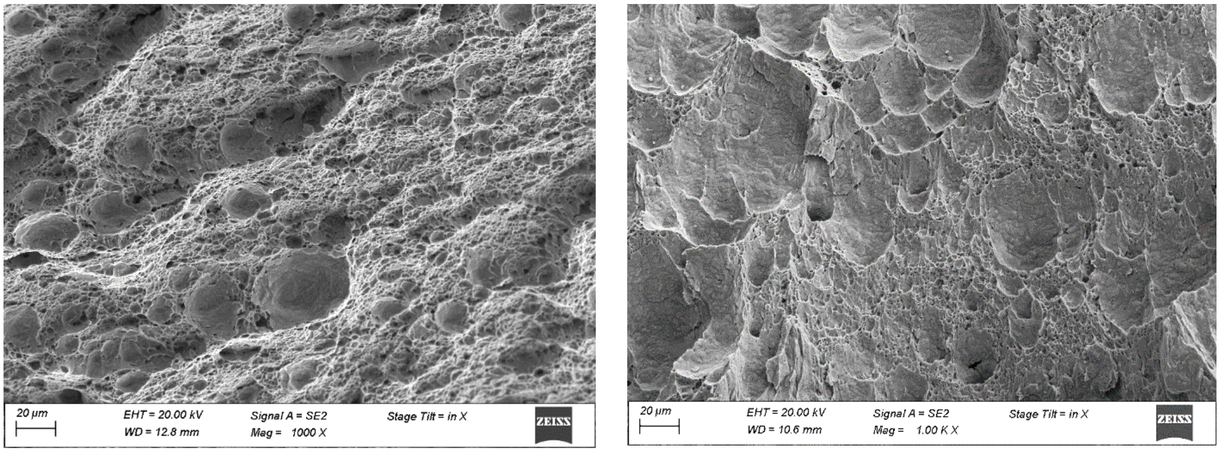

(a) **(b)**

Figure 6.51 Fractography of ductile area from IRCR Low-Nb tested at: (a) 0°F; and (b) -60°F.

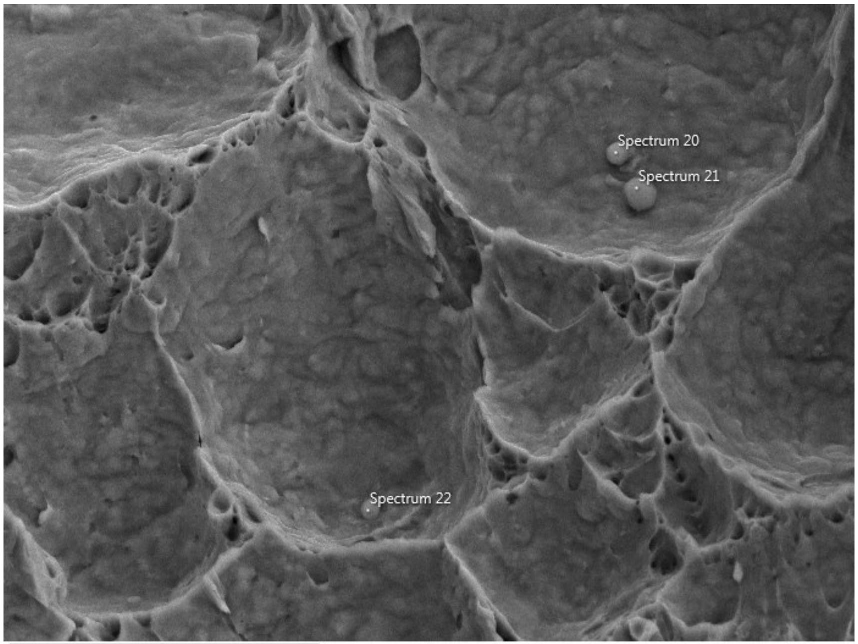

Spectrum Label	C	O	Al	Si	S	Ca	Ti	Mn	Fe
20	11.58	36.64	29.4		0.5	2.82	0.49	0.93	17.64
21	10.89	42.99	31.45	0.14	0.12	2.96	0.14	0.37	10.63
22	13.75	31.29	24.19		0.93	2.01	0.28	1.68	25.88

Figure 6.52 Non-metallic inclusions found in Low-Nb Steel dimples.

The brittle fracture occurred through cleavage. The characteristic feather-like facets can be observed in Figure 6.53.

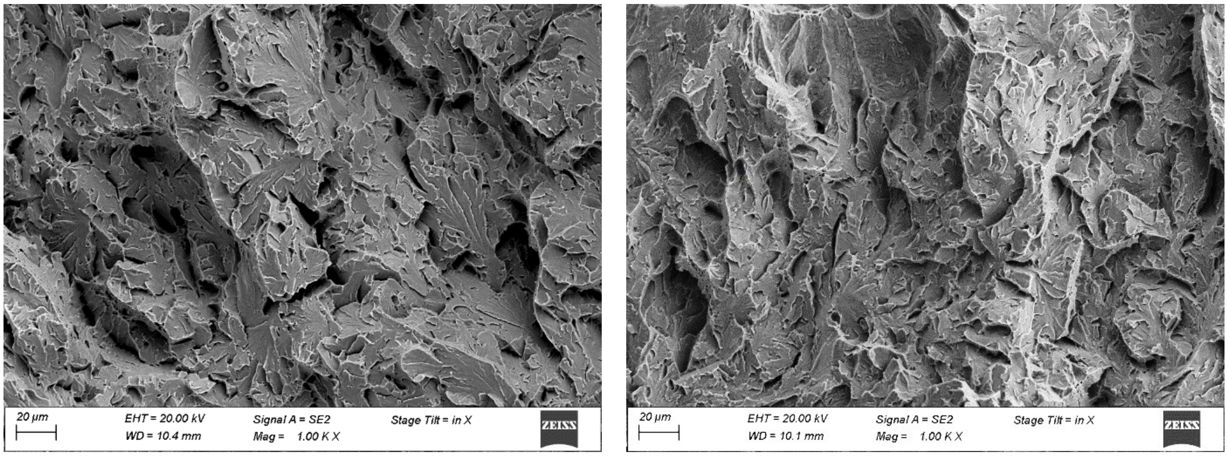

(a) **(b)**

Figure 6.53 Fractography of brittle area from IRCR Low-Nb, tested at: (a) 0°F; and (b) -60°F.

A small fraction of ductile fracture was observed among the brittle cleavage area. The facet size was measured for comparison to effective grain size measurements. No intragranular fracture was observed.

7.0 Conclusions and Future Work

7.1 Conclusions

Three studies were done on LP steel, that provided fundamental understanding of the evolution of the structural factors throughout the thermo-mechanical process, that control the final properties. Based on the results observed, the suggested novel approach IRCR to hot rolled HSLA linepipe steels provided several benefits. It allows the reduction of Nb content in the steel and has the potential to improve the productivity compared to the conventional CCR process. In addition, the following conclusions can be taken:

1. 0.051wt% Nb was enough to produce homogeneous grain size at 1200°C austenitization temperature when using a 1h soaking time.
2. The comparison of precipitates volume fraction calculated from empirical solubility products and based on measured precipitates did not match. These models do not consider the observed complexity of precipitate particles.
3. Complex precipitates resistance to dissolution allowed grain size control at high temperatures despite the low Nb content. Evidence of solute drag was not found. Hence, precipitation was regarded as the main mechanism for grain size control.
4. Reconstruction of austenite orientation maps based on martensite EBSD scans was effective for measuring PAGS and comparable to conventional methods. These reconstructions also helped show the conditioning of austenite, through KAM maps.
5. The use of Misaka and Siciliano models for predicting MFS is reliable for these steels. This holds, even though Misaka's model does not explicitly consider recrystallization effects. And despite the experimental data shows a more linear behavior with transitional slope at Tnr.

6. The temperature of no-recrystallization is sensitive to Nb content. In the present study, reducing Nb from 0.09wt% to 0.05wt% reduced Tnr by ~50°C from ~1025 to ~975°C. None of the models found in the literature could predict this temperature accurately.
7. Precipitation of standalone NbC particles and epitaxial NbC on pre-existing TiN is responsible for inhibition of recrystallization at the transfer bar. Evidence from EPMA showed minimum segregation at GBs, indicating that solute drag is not the controlling force of recrystallization. Precipitates' volume fraction, obtained experimentally, produced pinning forces one order of magnitude higher than recrystallization force.
8. Austenite conditioning was assessed through Effective Nucleation Area and Kernel Average Misorientation maps. After roughing deformation, the effective nucleation area was higher for the IRCR process than the CCR, but the KAM were quite similar. Austenite conditioning was regarded as very similar during roughing deformation. Finishing simulations, in torsion and in full scale experiments, provided KAM maps that agree on a higher accumulation of strain produced by IRCR as compared to CCR.
9. There is a big potential observed by the homogeneity obtained through IRCR processing. Other cooling rates must be tried, to reduce MA presence.
10. The proposed Low-Nb steel can achieve the strength and toughness required by API X70 specifications in 19mm thickness, if processed through IRCR. IRCR was successfully scaled-up to an industrial size experimental mill. Only half of the commercial Nb content was used and tensile properties exceeded specifications. Impact properties were superior than commercial HTP steel with twice as much Nb.

From the three objectives, two were completely achieved and one partially. Objective 1 was partially achieved, since the precipitation behavior of the IRCR process was optimized, however the microstructure has room for improvement. Especially the presence of MA constituent, which can be eliminated with a better cooling control. Objective 2 was achieved through IRCR process and the Low-Nb steel, which achieved homogeneity through thickness and competitive mechanical properties. Objective 3 was achieved, since the Low-Nb steel reduces alloy cost and showed improved impact toughness and competitive strength.

The experimental results from the proposed Low-Nb steel processed by IRCR, agree with the hypothesis statement. However, many opportunities of future work were identified, that can significantly improve the final transformation results.

7.2 Future Work

1. Further experiments may be done to determine the minimum soaking time for achieving equilibrium conditions of dissolution during reheating.
2. Models for the kinetics of dissolution, that account for precipitate's morphology effects, need to be developed for similar systems. The hypothesis of epitaxial precipitation followed by mutual interdiffusion should be tested.
3. Experiments can be done to determine the role of GBCD of austenite, to precipitate dissolution and grain coarsening phenomena in these steels. These can utilize the austenite EBSD map reconstruction tool.
4. Crystallographic changes such as formation of texture and changes in GBCD can be studied during deformation-recrystallization cycles.
5. A study for determining the reason for higher KAM in IRCR as compared to CCR is required. The study should answer why a smaller reduction of thickness, 46%, of IRCR produces higher KAM than the 66% reduction of CCR. A possibility to consider is differences in recovery behavior.
6. A study that combines IRCR with several cooling rates and finishing temperatures should be done to minimize MA content in IRCR processed steel. This study should look for a correlation between elimination of MA, precipitate enhancement and impact toughness improvement.

Appendix

A.1 Mechanical Properties Charts

A.1.1 Microhardness on validation specimens

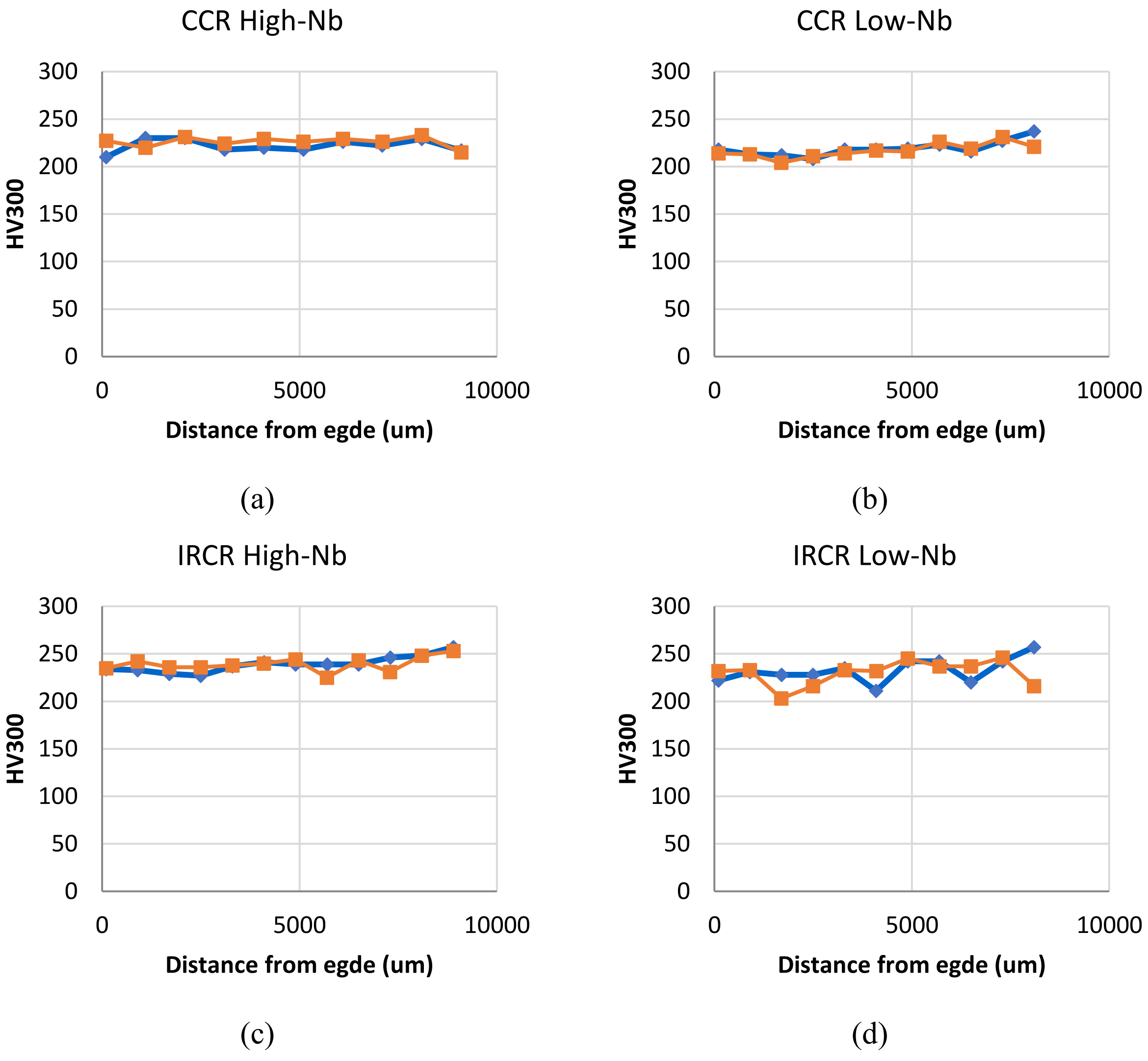

(a) (b) (c) (d)

Figure 7.1 Microhardness profile HV300 from edge to center.

A.1.2 Tensile test

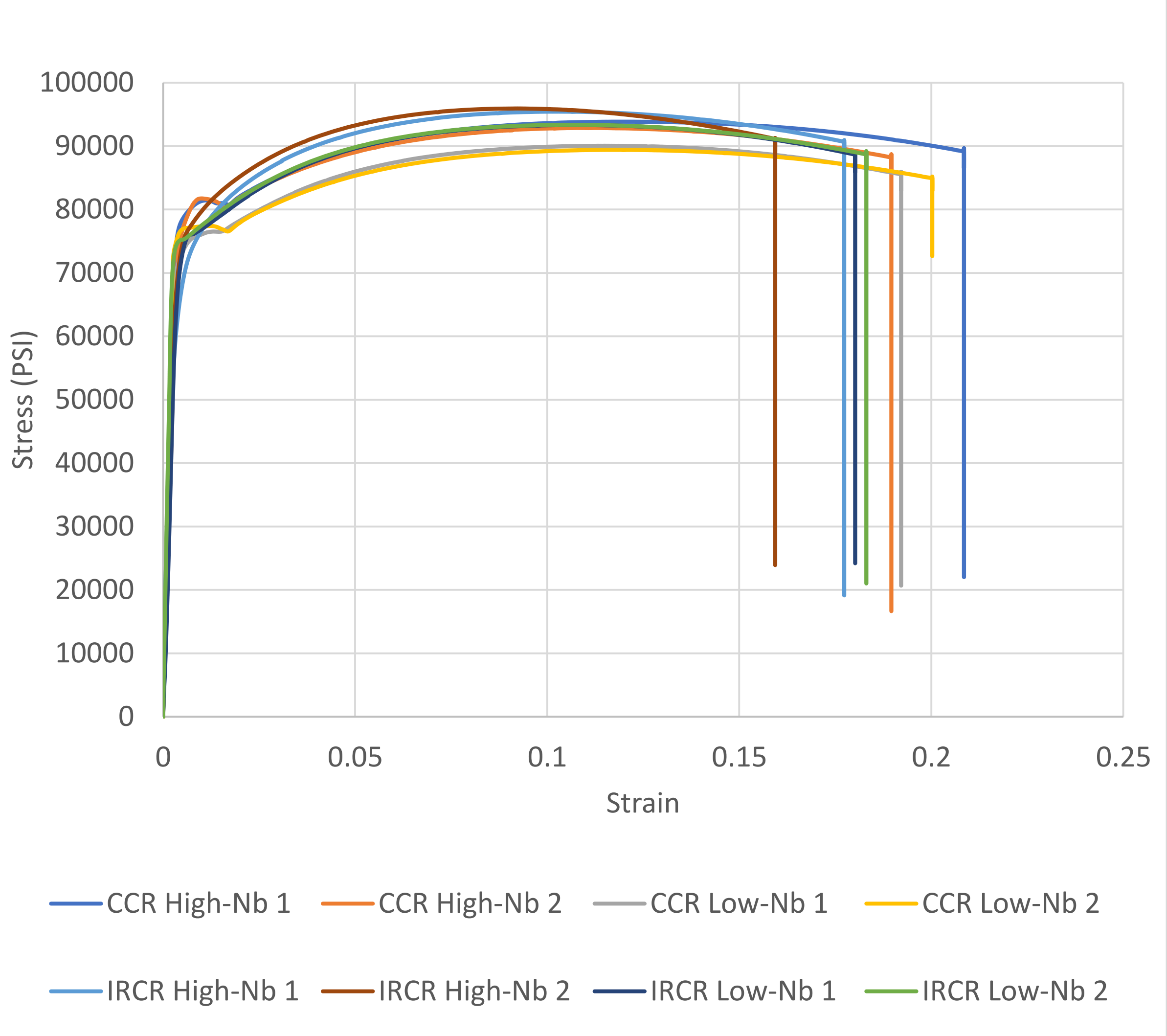

Figure 7.2. Stress-strain plot of tensile tests of final, full thickness, specimens.

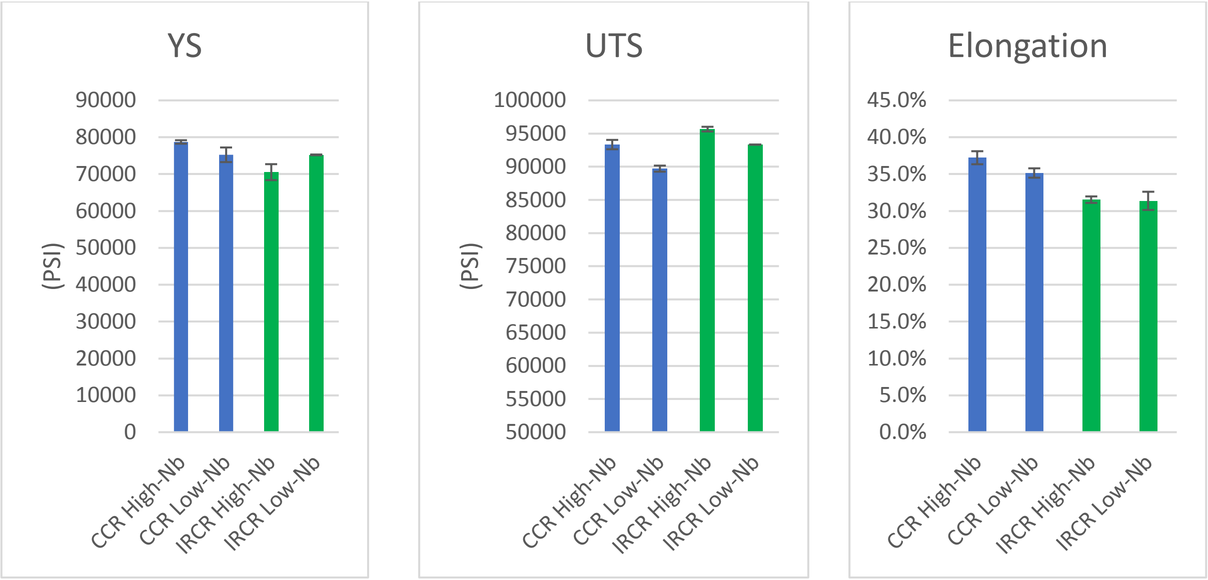

(a) (b) (c)

Figure 7.3. Tensile test results comparison.

A.2 Other EBSD relevant charts

A.2.1 Relevant observed Texture fiber components

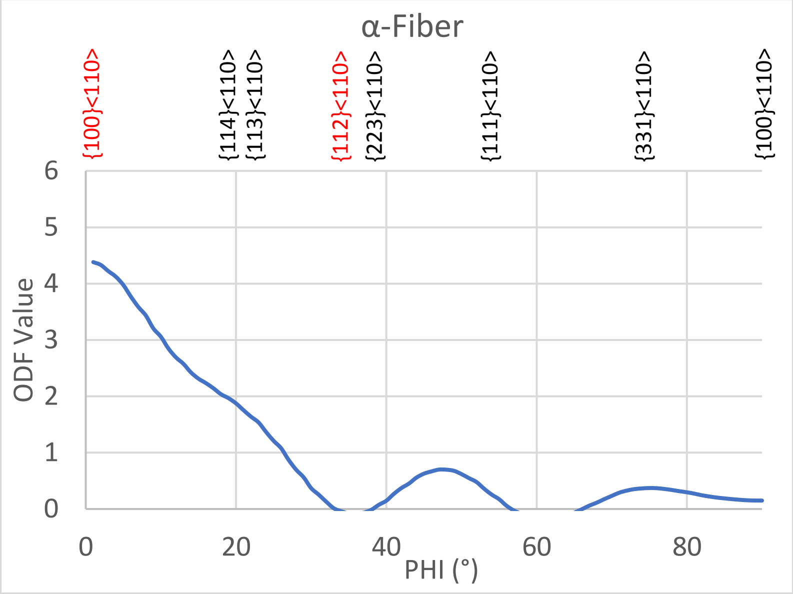

Figure 7.4 CCR High-Nb steel α-fiber

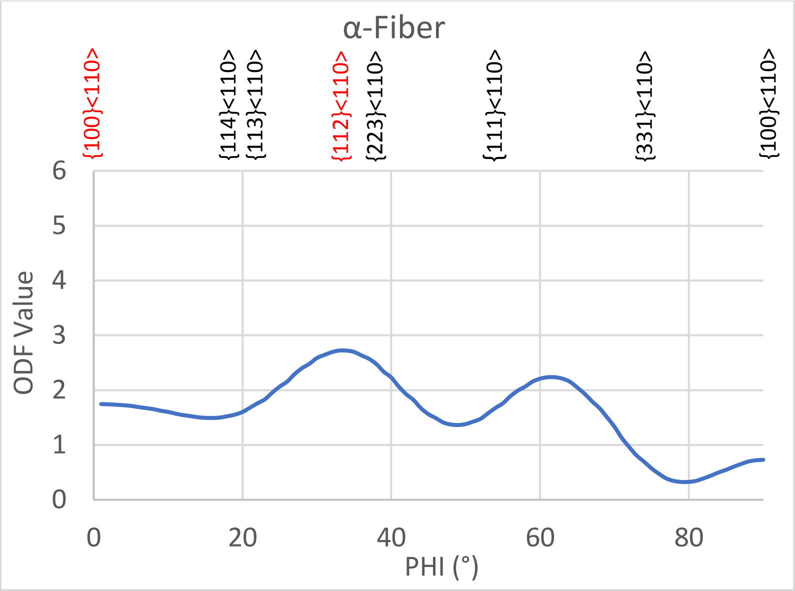

Figure 7.5 CCR Low-Nb α-fiber.

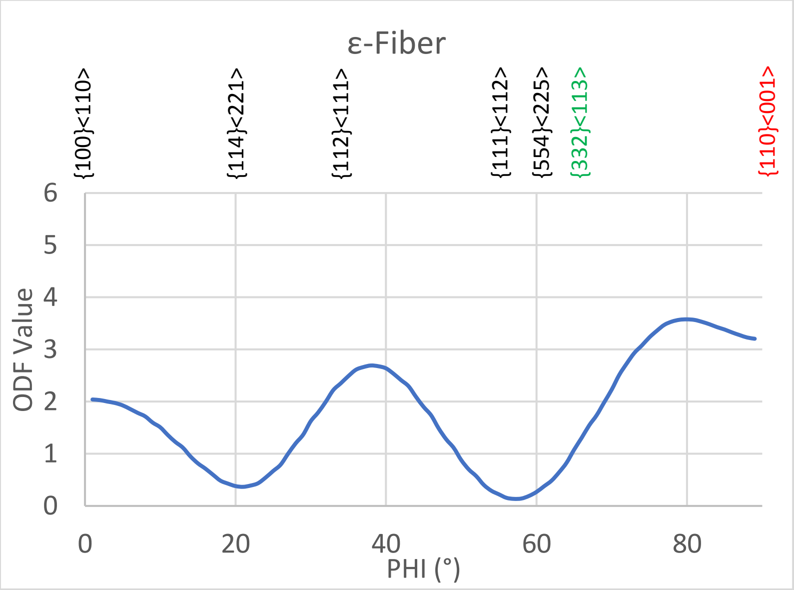

Figure 7.6 IRCR High-Nb ε-fiber.

A.3 Additional Micrographs

A.3.1 Relevant micrographs of precipitates

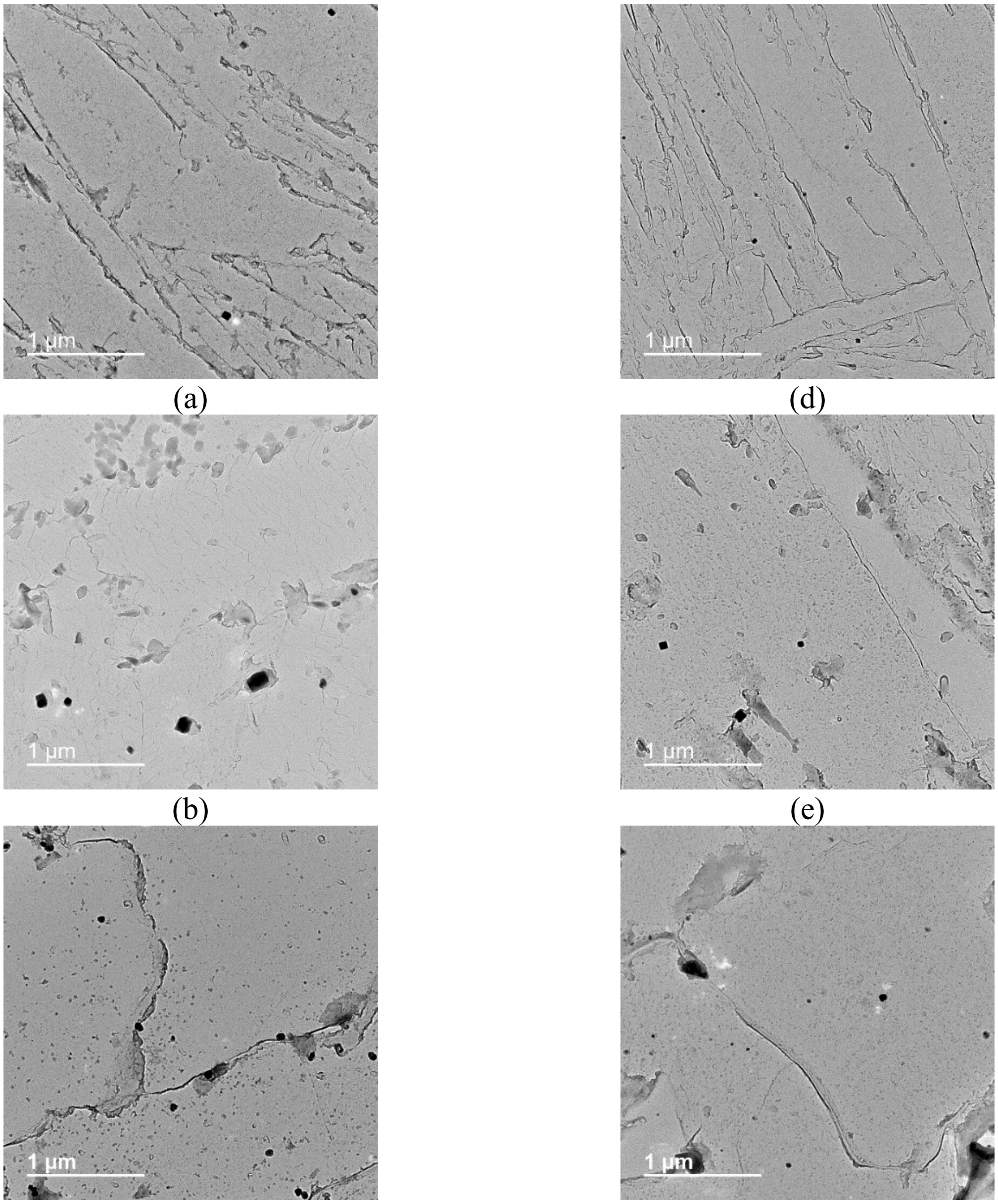

(a) (d)

(b) (e)

(c) (f)

Figure 7.7 Precipitation progress during hot processing: of CCR High-Nb (a) after reheating, (b) after roughing, (c) fully processed; and of IRCR Low-Nb (d) after reheating, (e) after roughing and (f) fully processed. 5000X.

Bibliography

[1] W.F. Hosford, Mechanical behavior of materials, Cambridge University Press, Cambridge, UK, 2010.

[2] E. Orowan, The crystal plasticity. III: about the mechanism of the sliding, Z Physik 89 (1934) 634-659.

[3] G.I. Taylor, The Mechanism of Plastic Deformation of Crystals. Part I. Theoretical, Proceedings of the Royal Society of London. Series A, Containing Papers of a Mathematical and Physical Character 145(855) (1934) 362-387.

[4] M. Polanyi, Über eine Art Gitterstörung, die einen Kristall plastisch machen könnte, Zeitschrift für Physik 89(9) (1934) 660-664.

[5] N.J. Petch, The ductile-brittle transition in the fracture of α-iron: I, The Philosophical Magazine: A Journal of Theoretical Experimental and Applied Physics 3(34) (1958) 1089-1097.

[6] F.R.N. Nabarro, Theoretical and experimental estimates of the Peierls stress, Philosophical Magazine A 75(3) (1997) 703-711.

[7] G.E. Dieter, D.J. Bacon, Mechanical metallurgy, SI Edition ed., McGraw-Hill, New York, NY, 1986.

[8] T. Gladman, The physical metallurgy of microalloyed steels, Maney Pub1997.

[9] A.H. Cottrell, B.A. Bilby, Dislocation Theory of Yielding and Strain Ageing of Iron, Proceedings of the Physical Society. Section A 62(1) (1949) 49-62.

[10] T. Gladman, Precipitation hardening in metals, Materials Science and Technology 15(1) (1999) 30-36.

[11] S.P. Ringer, W.B. Li, K.E. Easterling, On the interaction and pinning of grain boundaries by cubic shaped precipitate particles, Acta Metallurgica 37(3) (1989) 831-841.

[12] S. Iwamura, Y. Miura, Loss in coherency and coarsening behavior of Al3Sc precipitates, Acta Materialia 52(3) (2004) 591-600.

[13] S. Liu, F.-C. Liao, Precipitate stability in the heat affected zone of nitrogen-enhanced high strength low alloy steels, Materials Science and Engineering: A 244(2) (1998) 273-283.

[14] E.O. Hall, The Deformation and Ageing of Mild Steel: III Discussion of Results, Proceedings of the Physical Society. Section B 64(9) (1951) 747-753.

[15] N. Hansen, Hall–Petch relation and boundary strengthening, Scripta Materialia 51(8) (2004) 801-806.

[16] N.J. Petch, The cleavage strength of polycrystals, Journal of the Iron and Steel Institute 174 (1953) 25-28.

[17] H. Bhadeshia, R. Honeycombe, Steels: microstructure and properties, Butterworth-Heinemann2017.

[18] Z.W. Wang, Y.B. Wang, X.Z. Liao, Y.H. Zhao, E.J. Lavernia, Y.T. Zhu, Z. Horita, T.G. Langdon, Influence of stacking fault energy on deformation mechanism and dislocation storage capacity in ultrafine-grained materials, Scripta Materialia 60(1) (2009) 52-55.

[19] G.J. Tucker, D.L. McDowell, Non-equilibrium grain boundary structure and inelastic deformation using atomistic simulations, International Journal of Plasticity 27(6) (2011) 841-857.

[20] G.J. Tucker, M.A. Tschopp, D.L. McDowell, Evolution of structure and free volume in symmetric tilt grain boundaries during dislocation nucleation, Acta Materialia 58(19) (2010) 6464-6473.

[21] J.C. Li, Petch relation and grain boundary sources, Transactions of the Metallurgical Society of AIME 227(1) (1963) 239-&.

[22] J. Kacher, B.P. Eftink, B. Cui, I.M. Robertson, Dislocation interactions with grain boundaries, Current Opinion in Solid State and Materials Science 18(4) (2014) 227-243.

[23] I. Tamura, H. Sekine, T. Tanaka, Thermomechanical processing of high-strength low-alloy steels, Butterworth-Heinemann2013.

[24] J. Heslop, N.J. Petch, The ductile-brittle transition in the fracture of α-iron: II, The Philosophical Magazine: A Journal of Theoretical Experimental and Applied Physics 3(34) (1958) 1128-1136.

[25] J.J. Hauser, M.G.H. Wells, C. Colt Industries Inc Pittsburgh Pa Crucible Research, Inclusions in High-Strength and Bearing Steels. Their Dependence on Processing Variables and their Effect on Engineering Properties, Defense Technical Information Center, Ft. Belvoir, 1970.

[26] V. Gentilicore, A. Pense, R. Stout, FRACTURE TOUGHNESS OF PRESSURE-VESSEL STEEL WELDMENTS, WELD J--NEW YORK-- 49(8) (1970) 341.

[27] H. Sieurin, R. Sandström, Fracture toughness of a welded duplex stainless steel, Engineering Fracture Mechanics 73(4) (2006) 377-390.

[28] S. Arnold, Toughness of Steel Sheet: The Advantage of Laminating, Watertown Arsenal Labs., Mass., 1960.

[29] J.Y. Koo, M.J. Luton, N.V. Bangaru, R.A. Petkovic, D.P. Fairchild, C.W. Petersen, H. Asahi, T. Hara, Y. Terada, M. Sugiyama, H. Tamehiro, Y. Komizo, S. Okaguchi, M. Hamada, A.

Yamamoto, I. Takeuchi, Metallurgical Design of Ultra-High Strength Steels For Gas Pipelines, The Thirteenth International Offshore and Polar Engineering Conference, International Society of Offshore and Polar Engineers, Honolulu, HI, 2003.

[30] C.R. Brooks, Principles of the heat treatment of plain carbon and low alloy steels, ASM international, Knoxville, TN, 1996.

[31] S.K. Hwang, J.W. Morris, The use of a boron addition to prevent intergranular embrittlement in Fe-12Mn, Metallurgical Transactions A 11(7) (1980) 1197-1206.

[32] X. Liang, The Complex Phase Transformation of Austenite in High Strength Linepipe Steels and Its Influence on the Mechanical Properties, University of Pittsburgh, 2012, p. 1 online resource (237 pages).

[33] J.J.W. Morris, Z. Guo, C.R. Krenn, Y.H. Kim, The Limits of Strength and Toughness in Steel, ISIJ International 41(6) (2001) 599-611.

[34] S.Y. Shin, B. Hwang, S. Lee, N.J. Kim, S.S. Ahn, Correlation of microstructure and charpy impact properties in API X70 and X80 line-pipe steels, Materials Science and Engineering: A 458(1–2) (2007) 281-289.

[35] F.B. Pickering, Physical metallurgy and the design of steels, Applied Science Publishers1978.

[36] J. Gregg, H. Bhadeshia, Solid-state nucleation of acicular ferrite on minerals added to molten steel, Acta Materialia 45(2) (1997) 739-748.

[37] L. Shi, Z. Yan, Y. Liu, C. Zhang, Z. Qiao, B. Ning, H. Li, Improved toughness and ductility in ferrite/acicular ferrite dual-phase steel through intercritical heat treatment, Materials Science and Engineering: A 590 (2014) 7-15.

[38] M.-C. Zhao, K. Yang, Y.-Y. Shan, Comparison on strength and toughness behaviors of microalloyed pipeline steels with acicular ferrite and ultrafine ferrite, Materials Letters 57(9) (2003) 1496-1500.

[39] J.-S. Byun, J.-H. Shim, J.-Y. Suh, Y.-J. Oh, Y.W. Cho, J.-D. Shim, D.N. Lee, Inoculated acicular ferrite microstructure and mechanical properties, Materials Science and Engineering: A 319-321 (2001) 326-331.

[40] L. Lan, Z. Chang, X. Kong, C. Qiu, D. Zhao, Phase transformation, microstructure, and mechanical properties of X100 pipeline steels based on TMCP and HTP concepts, Journal of Materials Science 52(3) (2017) 1661-1678.

[41] H. Zhao, B.P. Wynne, E.J. Palmiere, Conditions for the occurrence of acicular ferrite transformation in HSLA steels, Journal of Materials Science 53(5) (2018) 3785-3804.

[42] B. Hwang, Y.G. Kim, S. Lee, Y.M. Kim, N.J. Kim, J.Y. Yoo, Effective grain size and charpy impact properties of high-toughness X70 pipeline steels, Metallurgical and Materials Transactions A 36(8) (2005) 2107-2114.

[43] M. Díaz-Fuentes, A. Iza-Mendia, I. Gutiérrez, Analysis of different acicular ferrite microstructures in low-carbon steels by electron backscattered diffraction. Study of their toughness behavior, Metallurgical and Materials Transactions A 34(11) (2003) 2505-2516.

[44] G. Krauss, Steels: processing, structure, and performance, ASM International2015.

[45] F. Matsuda, K. Ikeuchi, Y. Fukada, Y. Horii, H. Okada, T. Shiwaku, C. Shiga, Review of mechanical and metallurgical investigations of MA constituent in welded joint in Japan, Transactions of JWRI 24(1) (1995) 1-24.

[46] M.S. Joo, D.W. Suh, J.H. Bae, N. Sanchez Mouriño, R. Petrov, L.A.I. Kestens, H.K.D.H. Bhadeshia, Experiments to separate the effect of texture on anisotropy of pipeline steel, Materials Science and Engineering: A 556 (2012) 601-606.

[47] G.J. Baczynski, J.J. Jonas, L.E. Collins, The influence of rolling practice on notch toughness and texture development in high-strength linepipe, Metallurgical and Materials Transactions A 30(12) (1999) 3045-3054.

[48] J.-B. Ju, J.-S. Lee, J.-i. Jang, Fracture toughness anisotropy in a API steel line-pipe, Materials Letters 61(29) (2007) 5178-5180.

[49] H. Inagaki, K. Kurihara, I. Kozasu, Influence of Crystallographic Texture on the Strength and Toughness of the Controlled Rolled High Tensile Strength Steel, Tetsu-to-Hagane 61(7) (1975) 991-1011.

[50] ASM, High-Strength Low-Alloy Steels, in: ASM (Ed.) Alloying: Understanding the Basics, 2001.

[51] A.S.f. Materials, Volume 1, Properties and Selection: Irons, Steels, and High Performance Alloys, 2005.

[52] J.C. Villalobos, A. Del-Pozo, B. Campillo, J. Mayen, S. Serna, Microalloyed Steels through History until 2018: Review of Chemical Composition, Processing and Hydrogen Service, Metals 8(5) (2018) 351.

[53] P.A. Manohar, M. Ferry, T. Chandra, Ferrite and Austenite, Recrystallization of, in: K.H.J. Buschow, R.W. Cahn, M.C. Flemings, B. Ilschner, E.J. Kramer, S. Mahajan, P. Veyssière (Eds.), Encyclopedia of Materials: Science and Technology, Elsevier, Oxford, 2001, pp. 3019-3024.

[54] A.K. Das, The Present and the Future of Line Pipe Steels for Petroleum Industry, Materials and Manufacturing Processes 25(1-3) (2010) 14-19.

[55] P.R. Rios, Abnormal grain growth development from uniform grain size distributions, Acta Materialia 45(4) (1997) 1785-1789.

[56] T. Nishizawa, I. Ohnuma, K. Ishida, Examination of the Zener relationship between grain size and particle dispersion, Materials Transactions, JIM(Japan) 38(11) (1997) 950-956.

[57] T. Gladman, On the theory of the effect of precipitate particles on grain growth in metals, Proceedings of the Royal Society of London A: Mathematical, Physical and Engineering Sciences, The Royal Society, 1966, pp. 298-309.

[58] P.R. Rios, A theory for grain boundary pinning by particles, Acta Metallurgica 35(12) (1987) 2805-2814.

[59] P.R. Rios, On the relationship between pinning force and limiting grain radius, Scripta Materialia 34(8) (1996) 1185-1188.

[60] R.E. Reed-Hill, R. Abbaschian, Physical metallurgy principles, Brooks/Cole Engineering Division Monterey, Calif, USA1973.

[61] M.I. Vega, S.F. Medina, A. Quispe, Oacute, M. Mez, Oacute, P.P. Mez, Influence of TiN Particle Precipitation State on Static Recrystallisation in Structural Steels, ISIJ International 45(12) (2005) 1878-1886.

[62] E.J. Palmiere, C.I. Garcia, A.J. DeArdo, The influence of niobium supersaturation in austenite on the static recrystallization behavior of low carbon microalloyed steels, Metallurgical and Materials Transactions A 27(4) (1996) 951-960.

[63] M.I. Vega, S.F. Medina, A. Quispe, M. Gómez, P.P. Gómez, Recrystallisation driving forces against pinning forces in hot rolling of Ti-microalloyed steels, Materials Science and Engineering: A 423(1) (2006) 253-261.

[64] N. Gao, T.N. Baker, Austenite Grain Growth Behaviour of Microalloyed Al–V–N and Al–V–Ti–N Steels, ISIJ International 38(7) (1998) 744-751.

[65] J. Moon, J. Lee, C. Lee, Prediction for the austenite grain size in the presence of growing particles in the weld HAZ of Ti-microalloyed steel, Materials Science and Engineering: A 459(1–2) (2007) 40-46.

[66] S. Weinig, E.S. Machlin, Investigation of the effects of solutes on the grain boundary stress relaxation phenomenon, Trans. AIME 209 (1957) 32-41.

[67] W.F. Hosford, Physical Metallurgy, Taylor & Francis2005.

[68] J.F. Siciliano, K. Minami, T.M. Maccagno, J.J. Jonas, Mathematical Modeling of the Mean Flow Stress, Fractional Softening and Grain Size during the Hot Strip Rolling of C-Mn Steels, ISIJ International 36(12) (1996) 1500-1506.

[69] S.V. Subramanian, M. Xiaoping, K. Rehman, Austenite Grain Size Control in Upstream Processing of Niobium Microalloyed Steels by Nano-Scale Precipitate Engineering of TiN-NbC Composite, Springer International Publishing, Cham, 2016, pp. 639-650.

[70] C.-x. Yue, L.-w. Zhang, J.-h. Ruan, H.-j. Gao, Modelling of recrystallization behavior and austenite grain size evolution during the hot rolling of GCr15 rod, Applied Mathematical Modelling 34(9) (2010) 2644-2653.

[71] R. Lagneborgh, T. Siwecki, S. Zajac, B. Hutchinson, The Role of Vanadium in Microalloyed Steels, The Scandinavian Journal of Metallurgy (1999) 86.

[72] K. Al-Hajeri, The grain coarsening and subsequent transformation of austenite in the HSLA steel during high temperature thermomechanical processing, University of Pittsburgh, 2005, p. 1 online resource (1 volume).

[73] S.S. Hansen, J.B.V. Sande, M. Cohen, Niobium carbonitride precipitation and austenite recrystallization in hot-rolled microalloyed steels, Metallurgical Transactions A 11(3) (1980) 387-402.

[74] A. le Bon, J. Rofes-Vernis, C. Rossard, Recrystallization and Precipitation during Hot Working of a Nb-Bearing HSLA Steel, Metal Science 9(1) (1975) 36-40.

[75] L. Bäcke, Modeling the Microstructural Evolution during Hot Deformation of Microalloyed Steels, Materials Science and Engineering Division of Mechanical Metallurgy, Royal Institute of Technology, Stockholm, Sweeden, 2009.

[76] G.I. Rees, H.K.D.H. Bhadeshia, Thermodynamics of acicular ferrite nucleation, Materials Science and Technology 10(5) (1994) 353-358.

[77] H. Jun, J. Kang, D. H. Seo, K. B. Kang, C. G. Park, Effects of deformation and boron on microstructure and continuous cooling transformation in low carbon HSLA steels, Materials Science and Engineering A-structural Materials Properties Microstructure and Processing - MATER SCI ENG A-STRUCT MATER 422 (2006) 157-162.

[78] Y. Gu, G.-y. Qiao, D.-y. Wu, B. Liao, F.-r. Xiao, Precipitation kinetics of Nb carbonitride in austenite and acicular ferrite and its effect on hardness of high-Nb steel, Materials Chemistry and Physics 183 (2016) 506-515.

[79] P.J. Hurley, P.D. Hodgson, Formation of ultra-fine ferrite in hot rolled strip: potential mechanisms for grain refinement, Materials Science and Engineering: A 302(2) (2001) 206-214.

[80] P.R. Jepson, D. Bozkaya, Refractory metal plates with improved uniformity of texture, Google Patents, 2015.

[81] C.N. Homsher, Determination of the non-recrystallization temperature (Tnr) in multiple microalloyed steels, Department of Metallurgical and Materials Engineering, Colorado School of Mines, Denver, CL, USA, 2013.

[82] Y. Prawoto, N. Jasmawati, K. Sumeru, Effect of Prior Austenite Grain Size on the Morphology and Mechanical Properties of Martensite in Medium Carbon Steel, Journal of Materials Science & Technology 28(5) (2012) 461-466.

[83] H.-S. Yang, H.K.D.H. Bhadeshia, Austenite grain size and the martensite-start temperature, Scripta Materialia 60(7) (2009) 493-495.

[84] A. García-Junceda, C. Capdevila, F.G. Caballero, C.G. de Andrés, Dependence of martensite start temperature on fine austenite grain size, Scripta Materialia 58(2) (2008) 134-137.

[85] F.B. Pickering, B. Garbarz, The effect of transformation temperature and prior austenite grain size on the pearlite colony size in vanadium treated pearlitic steels, Scripta Metallurgica 21(3) (1987) 249-253.

[86] V. Blancas, A new view of the Grain-Coarsening Behavior of austenite in Ti-microalloyed Low-Carbon Steels, Department of Mechanical Engineering and Materials Science, University of Pittsburgh, Pittsburgh, PA, USA, 2016.

[87] L.J. Cuddy, J.C. Raley, Austenite grain coarsening in microalloyed steels, Metallurgical Transactions A 14(10) (1983) 1989-1995.

[88] Y.W. Kim, J.H. Kim, S.-G. Hong, C.S. Lee, Effects of rolling temperature on the microstructure and mechanical properties of Ti–Mo microalloyed hot-rolled high strength steel, Materials Science and Engineering: A 605 (2014) 244-252.

[89] P. Rodrigues, P. Andersan dos Santos, M.F. De Campos, Nb-Ti Microalloyed HSLA steel structural evolution during hot rolling in pilot scale, COBEF, ABCM, Caxias do Sul, RS, Brazil, 2011.

[90] X. Chen, Y. Huang, Hot deformation behavior of HSLA steel Q690 and phase transformation during compression, Journal of Alloys and Compounds 619 (2015) 564-571.

[91] D.Q. Bai, S. Yue, W.P. Sun, J.J. Jonas, Effect of deformation parameters on the, Metallurgical Transactions A 24(10) (1993) 2151-2159.

[92] C. Ouchi, T. Okita, Dynamic Recrystallization Behavior of Austenite in Nb-bearing High Strength Low Alloy Steels and Stainless Steel, Transactions of the Iron and Steel Institute of Japan 22(7) (1982) 543-551.

[93] J. Cahn, JW Cahn, Acta Metall. 10, 789 (1962), Acta Metall. 10 (1962) 789.

[94] X. Ma, C. Miao, B. Langelier, S. Subramanian, Suppression of strain-induced precipitation of NbC by epitaxial growth of NbC on pre-existing TiN in Nb-Ti microalloyed steel, Materials & Design 132 (2017) 244-249.

[95] B. Guo, L. Fan, Q. Wang, Z. Fu, Q. Wang, F. Zhang, Effect of Finish Rolling Temperature on the Microstructure and Tensile Properties of Nb–Ti Microalloyed X90 Pipeline Steel, Metals 6(12) (2016) 323.

[96] J. Zrník, T. Kvackaj, A. Pongpaybul, P. Sricharoenchai, J. Vilk, V. Vrchovinsky, Effect of thermomechanical processing on the microstructure and mechanical properties of Nb–Ti microalloyed steel, Materials Science and Engineering: A 319-321 (2001) 321-325.

[97] V. Carretero Olalla, V. Bliznuk, N. Sanchez, P. Thibaux, L.A.I. Kestens, R.H. Petrov, Analysis of the strengthening mechanisms in pipeline steels as a function of the hot rolling parameters, Materials Science and Engineering: A 604 (2014) 46-56.

[98] C. García de Andrés, F. Caballero, C. Capdevila, D. San Martín, Revealing austenite grain boundaries by thermal etching: Advantages and disadvantages, 2002.

[99] T. Nyyssönen, M. Isakov, P. Peura, V.-T. Kuokkala, Iterative Determination of the Orientation Relationship Between Austenite and Martensite from a Large Amount of Grain Pair Misorientations, Metallurgical and Materials Transactions A 47(6) (2016) 2587-2590.

[100] T. Nyyssönen, P. Peura, V.-T. Kuokkala, Crystallography, Morphology, and Martensite Transformation of Prior Austenite in Intercritically Annealed High-Aluminum Steel, Metallurgical and Materials Transactions A (2018).

[101] E. Gomes, L.A.I. Kestens, Fully automated orientation relationship calculation and prior austenite reconstruction by random walk clustering, IOP Conference Series: Materials Science and Engineering 82 (2015) 012059.

[102] S.M. Van Dongen, Graph clustering by flow simulation, 2000.

[103] M. Charleux, W.J. Poole, M. Militzer, A. Deschamps, Precipitation Behavior and its Effect on Strengthening of an HSLA-NbTi Steel, Metallurgical and Materials Transactions A 32A(July 2001) (2001) 1635-1648.

[104] C.B. Carter, D.B. Williams, Transmission electron microscopy, Springer-Verlag US2009.

[105] D.A. Porter, K.E. Easterling, M. Sherif, Phase Transformations in Metals and Alloys, (Revised Reprint), CRC press, New York, NY, 2009.

[106] E. Turkdogan, Causes and effects of nitride and carbonitride precipitation during continuous casting, Iron Steelmaker 16(5) (1989) 61.

[107] E.J. Pavlina, J.G. Speer, C.J. Van Tyne, Equilibrium solubility products of molybdenum carbide and tungsten carbide in iron, Scripta Materialia 66(5) (2012) 243-246.

[108] K. Xu, B.G. Thomas, R. O'malley, Equilibrium Model of Precipitation in Microalloyed Steels, Metallurgical and Materials Transactions A 42(2) (2011) 524-539.

[109] W. Wang, H.R. Wang, A simple method to determine the complex carbonitride composition in multicomponent microalloyed austenite, Materials Letters 61(11) (2007) 2227-2230.

[110] L. Xiaodong, J.K. Solberg, R. Gjengedal, A.O. Kluken, An expression for solubility product of complex carbonitrides in multicomponent microalloyed austenite, Scripta metallurgica et materialia 31(12) (1994) 1607-1612.

[111] M.F. Ashby, K.E. Easterling, A first report on diagrams for grain growth in welds, Acta Metallurgica 30(11) (1982) 1969-1978.

[112] C.J. Tweed, N. Hansen, B. RALPH, Grain growth in samples of aluminum containing alumina particles, Metallurgical Transactions A 14(11) (1983) 2235-2243.

[113] Y. Hayakawa, M. Muraki, J. Szpunar, The changes of grain boundary character distribution during the secondary recrystallization of electrical steel, Acta materialia 46(3) (1998) 1063-1073.

[114] Y. Hayakawa, J.A. Szpunar, The role of grain boundary character distribution in secondary recrystallization of electrical steels, Acta Materialia 45(3) (1997) 1285-1295.

[115] X. Tao, J. Gu, L. Han, Carbonitride Dissolution and Austenite Grain Growth in a High Cr Ferritic Heat-resistant Steel, ISIJ International 54(7) (2014) 1705-1714.

[116] H.O.K. Kirchner, Coarsening of grain-boundary precipitates, Metallurgical Transactions 2(10) (1971) 2861-2864.

[117] H.U. Hong, B.S. Rho, S.W. Nam, Correlation of the M23C6 precipitation morphology with grain boundary characteristics in austenitic stainless steel, Materials Science and Engineering: A 318(1–2) (2001) 285-292.

[118] C.J. Tweed, B. Ralph, N. Hansen, The pinning by particles of low and high angle grain boundaries during grain growth, Acta Metallurgica 32(9) (1984) 1407-1414.

[119] C. Zener, Private communication to CS Smith, Trans. AIME 175(15) (1949) ll.

[120] A. Grajcar, Thermodynamic analysis of precipitation processes in Nb–Ti-microalloyed Si–Al TRIP steel, Journal of Thermal Analysis and Calorimetry 118(2) (2014) 1011-1020.

[121] S.H. Mousavi Anijdan, S. Yue, The necessity of dynamic precipitation for the occurrence of no-recrystallization temperature in Nb-microalloyed steel, Materials Science and Engineering: A 528(3) (2011) 803-807.

[122] A. Nowotnik, T. Siwecki, The effect of TMCP parameters on the microstructure and mechanical properties of Ti–Nb microalloyed steel, Journal of Microscopy 237(3) (2010) 258-262.

[123] J. Lu, J.B. Wiskel, O. Omotoso, H. Henein, D.G. Ivey, Matrix Dissolution Techniques Applied to Extract and Quantify Precipitates from a Microalloyed Steel, Metallurgical and Materials Transactions A 42(7) (2011) 1767-1784.

[124] R. Wang, C.I. Garcia, M. Hua, K. Cho, H. Zhang, A.J. DeArdo, Microstructure and Precipitation Behavior of Nb, Ti Complex Microalloyed Steel Produced by Compact Strip Processing, ISIJ International 46(9) (2006) 1345-1353.

[125] S.G. Hong, H.J. Jun, K. K.B., C.G. Park, Evolution of precipitates in the Nb-Ti-V microalloyed HSLA steels during reheating, Scripta Materialia 48 (2003) 1201-1206.

[126] A.J. Craven, K. He, L.A.J. Garvie, T.N. Baker, Complex heterogeneous precipitation in titanium–niobium microalloyed Al-killed HSLA steels—I. (Ti,Nb)(C,N) particles, Acta Materialia 48(15) (2000) 3857-3868.

[127] F. Fletcher, Meta-analysis of Tnr measurements: Determining new empirical models based on composition and strain, Austenite Processing Symposium (Internal company presentation), 2008, pp. 1-14.

[128] Y. Misaka, T. Yoshimoto, Formularization of mean resistance to deformation of plain carbon steels at elevated temperature, Journal of The Japan Soc. Tec. Plasticity 8(79) (1967) 414-422.

[129] T. Kvackaj, I. Mamuzic, A Quantitative Characterization of Austenite Microstructure after Deformation in Nonrecrystallization Region and Its Influence on Ferrite Microstructure after Transformation, ISIJ International 38(11) (1998) 1270-1276.

[130] C. Moussa, M. Bernacki, R. Besnard, N. Bozzolo, About quantitative EBSD analysis of deformation and recovery substructures in pure Tantalum, IOP Conference Series: Materials Science and Engineering 89 (2015) 012038.

[131] J. Wu, Development of a new technique to identify and quantify complex austenite decomposition products, University of Pittsburgh, 2005.